Novel Embedded Metrology Instruments for the Light Controlled Factory

Azini, Maria

Award date:
2021

Awarding institution:
University of Bath

Novel Embedded Metrology Instruments for the Light Controlled Factory

Maria Azini
University of Bath

Submitted for the degree of Doctor of Philosophy
February 2021

Supervised by
Prof. William J. Wadsworth

Centre for Photonics and Photonic Materials
Department of Physics
University of Bath
United Kingdom

Abstract

This thesis aims to document the work done over the previous thirty-six months as part of the Light Controlled Factory (LCF) research project. The first part of the thesis aims to familiarise the reader with a) the "problem" that we are trying to solve, b) some standard metrology terms and c) state-of-the-art coordinate measuring machines and techniques such as laser tracker and photogrammetry. The environment is the main limiting factor when trying to provide accurate measurements in large scale manufacturing, such as aircraft production. In the following chapters the "solution" is referred to as AMS, Absolute Multilateration Between Spheres. The idea involves interferometry in order to measure the distance between the centres of two spheres whilst the optical path is shielded from environmental disturbances.

Two computational AMS models, the ray tracing and Gaussian beam models, were developed in order to test and confirm the validity of the solution. Their capabilities were investigated and compared. The data gathered suggest that using feedback inherent to the system it is possible to achieve sub-micron accuracy when aligning the interferometer. The experimental work involved the development of a Mach Zhender and the AMS interferometers. The interference patterns were analysed and the data gathered from the quadrature detection were interpreted. It was therefore possible to define the direction of the movement of the interferometric pattern and whether or not it had moved to the next fringe (or by a whole fringe).

Even though the diode laser used was surprisingly stable (∼30MHz) without any external systems involved, a feedback loop was developed in order to stabilise its frequency. For this a series of equipment was required i.e. frequency generator, lock-in amplifier, PID controller etc. A number of recordings of the interferometric signals, $I\&Q$, for short (a few seconds) and long (∼12-hours) term time scales was taken when the laser was unlocked, frequency stabilised whilst using only the P term of the PID controller and frequency stabilised whilst using the PI terms. At the same time the beat frequency and Allan deviation of the laser was calculated. A combination of the results led to the conclusion that when using the feedback controller loop, the laser was locked to better than 0.4 MHz at 10^4 seconds.

At the same time, a hollow core optical fibre was designed and fabricated in order to develop an all-fibre acetylene gas cell for a collaboration project with the National Physical Laboratory. Their system already contains an acetylene reference cell (50 Torr) for monitoring frequency and frequency stability of the laser in a Frequency Scanning Interferometry (FSI) system. However, using an optical fibre gas cell implies that the absorption peaks can have a much smaller pressure shift as the pressure inside the fibre can be reduced whilst increasing the fibre's length. A comparison of pressure shifts for the acetylene spectrum of the three different cells along with the Gaussian lineshape fits confirm that the centers of the acetylene peaks can be determined with higher accuracy when using the fibre gas cell and the device can be implemented in an FSI system. Converting this device into an all-fibre design created issues regarding back-reflections. To minimise back-reflections a series of experiments was performed that involved tapering a single mode fibre and inserting it into the hollow core fibre, and coupling light in and out of a hollow core fibre using angled polished patch cables. The back-reflections were

minimised to -42dB and less than -66.3 dB respectively. The second option was therefore more promising and a technique was developed for implementing angle polished fibres in an all-fibre gas cell device. This involved coupling light in and out of a hollow core fibre using angle cleaved pigtails whilst relying on a tight fit inside a capillary. The preliminary results were positive though the technique requires further improvement.

Acknowledgements

There are quite a few people I would like to thank for their support throughout this journey.

William, I am so worried that words are not good enough to express my gratitude and respect to you. You have always been there when I needed your help. You have always been so enthusiastic about research and you are such an inspiration for all your students. I feel so lucky that I was given the chance to work with you.

Kristina, it was a pleasure working with you. From the spinning preforms to the embarrassing attempts to couple light into an SMF-28, I have made so many memories in the lab with you. Also thank you for the numerous times you solved my MATLAB issues.

To Stefanos and Tim, thank you both for showing interest in our research and using your amazing tapers to improve our experiment.

To my PhD friends, Kerri Harrington, Harry Wood, James Arter, Marie Anderson, Tom McManus, Mengrong Xu, Anastasia Efthymiadou, Tom Wright and Adam Earthey. Thank you for all the amazing memories over the past few years.

To my family, especially my amazing granddad and grandma, thank you for supporting me all these years.

Last but not least... Thank you for being in my life Jon. I cannot wait to see what the future holds for us.

Contents

Chapter 1

Introduction

In this section the LCF's project description and goals are described as well as the need and motivation behind the development of a new length metrology system.

1.1 Light Controlled Factory (LCF)

The LCF project was born due to the urgent need to provide high accuracy measurements for large scale manufacturing within a factory environment with particular emphasis on aircraft structure manufacturing. To accomplish this, the Engineering and Physical Sciences Research Council (EPSRC) has funded the team which consists of three academic institutions (University of Bath, University College London and Loughborough University) and nine industry partners including Hexagon, National Physical Laboratory,

Rolls-Royce Plc and Airbus Group Limited. The research consortium is led by the University of Bath.

The project seeks to define and re-develop the key technologies in order to provide a "new template for a new type of factory" which will include novel measurement-based techniques for machine control and parts verification. To assemble aircraft structures, tooling (e.g. jigs) is currently being used to control their key dimensions. For stability the tooling is secured to the reinforced-concrete floor and these capital intensive structures are very inflexible. This method's accuracy (positional, dimensional and geometric) as well as the jig location, datum and pin diameter are all implied from the tooling. In other words, provided that the tooling is correct, in combination with accurate positioning of the components within the tooling, the assembly will be successful. This rather slow (and costly) process requires improvement. Furthermore, better performance and high efficiency, for the aerospace structure, can be achieved through weight reduction and tightening of aerodynamic profile tolerances[1].

The project has been broken down into four themes:

Research Theme 1: Measurement assisted assembly technology with integrated processing machines.

Research Theme 2: Measurement methods for establishing the uncertainty due to gravitational effects and thermal gradients.

Research Theme 3: An ubiquitous 7D (x, y and z translation, pitch, roll and yaw rotation and time) measurement environment for the factory environment.

Research Theme 4: Build a Demonstrator and integrated experimental validation [2,3].

This research was part of the third theme and took place in the Physics Department (in collaboration with the Department of Mechanical Engineering). It involved the design of a new interferometric system and the design and fabrication of an optical fibre, which took place in the fibre tower of the Centre for Photonics and Photonic Materials (CPPM).

1.2 Motivation

Currently the accuracy provided during the process of aircraft production in a factory environment is limited by many factors, including environmental effects [1]. A major technical challenge is to overcome effects such as temperature variation and line-of-sight obstruction. An interesting example can be seen from the data that Airbus has provided to the LCF group. An Airbus A350 wing which is 25 m long, can have positioning errors of 1.6 mm

caused by the thermal expansion of tooling of 6°C (over a day-to-night thermal cycle). This suggests that the structure needs to be constantly monitored and measured. Optical methods (i.e. use of optical lasers) seem to be the most accurate methods for measuring large scale manufacturing. However, a line-of-sight is required and temperature variations can affect the outcome of the measurement.

The main drawback of employing such a method is that a change in temperature can affect the refractive index (n) of air. The dependence of n on temperature, as well as changes in pressure, humidity and CO_2 are extremely important when a system that uses an optical method is required to provide precision measurements for a given structure. The system will measure nL (L being the size of the object), therefore a temperature variation will have a significant impact on the precision of the technique. Work that has been done from former members of the LCF group (P. Maropoulos *et al*), produced a model that can simulate component and assembly level variation due to designed tolerances[4]. The results gathered during a case study suggest that the model can be implemented in the assembly of large scale manufacturing as it can provide insight into accurate compensation for thermal expansion at the part[4]. More data that support the need of a new system which will not be subject to environmental

conditions are the following facts: laser straightness (caused by vertical thermal gradients of $1°\mathrm{Cm}^{-1}$) and optical triangulation measurement can be distorted by 0.3 mm over the 25m scale[5]. To achieve laminar flow and interchangeability, the next generation of aerospace structures has to provide surface profile and position tolerances of 0.5 mm and 40 µm respectively. These features correspond to required measurement uncertainties of the order of 50 µm and 4 µm respectively[6].

The idea presented in this thesis is to create a new interferometric design that involves absolute distance measurement in order to calculate the distance between the centre of two spheres. When measuring the distance between spheres it is possible to mechanically shield the laser path from environmental disturbances while exposing most of the spheres' surfaces as external datum points and form a triangulated network of arbitrary shape in order to cover a jig. By discretizing the space, the measured path can be locally enclosed and the temperature $T(x, y, z, t)$ will collapse to a number of measured temperatures T_i (with some small variation over time), for each scale bar. Therefore, by utilizing the fact that the spheres can be part of more than one interferometer simultaneously, the line-of-sight issue can be overcome and uncertainties in the measurements caused by thermal fluctuations can be minimised. The model (simulations and experimental

design) is called Absolute Multilateration between Spheres (or AMS model).

A similar technique was recently employed for the development of Lasertracer-MT from Etalon. It provides a measurement for the displacement of a sphere and a retroreflector (moving relative to one another) using differential interferometry [7]. It was found that the technique used i.e. fringe counting, provides a 500 nm uncertainty over 1 m whereas the technique employed for the ATLAS project (frequency scanning interferometry FSI), can measure an absolute distance (explained in Section 2.3) of 1 m with an uncertainty of 250 nm (with temperature control) [8,9].

The results that have been generated from the computational model prove that it is possible to obtain interferometric fringes from the system and that we can achieve sub-micron accuracy using feedback inherent to the system. More details about the model can be found in Section 4.

1.3 LCF's Project Goals

As mentioned earlier, LCF's aim is to provide high accuracy measurements for large scale manufacturing within a factory environment. It aspires to address this need by producing and designing three classes of novel technologies; measurement-assisted assembly, computational and

experimental methods for providing uncertainty of assembly machines and parts, a 7D (6DOF and time) measurement environment to provide positional accuracy from 10 µm to 500 µm as well as aspects of temporal and spatial self-awareness[10]. Self-awareness for a machine can be achieved when a feedback signal is sent to the system so it will always be aware of its position in space and time. This requires fast data acquisition and processing systems i.e. for the robot (shown if figure 1.1), the data acquisition has to be faster than its movement.

Once all these individual tasks are completed and each academic institute finalise their models, everything will be brought together in order to create a demonstrator. By the end of this project the three academic institutions have to provide to the industrial partners a multi-instrument measurement assisted assembly and control system. The initial design of the demonstrator is depicted in Figure 1.1. The Demonstrator cell will integrate a number of measurement systems to enable a process that is not possible with any single system. The sequential flow of measurement data between these systems is detailed below: Each instrument plays a distinct role in the process:

Fringe Projection: Enables direct measurement of features on the part such as holes, edges, pins etc. This will eliminate the uncertainties inherent in facility tooling while also removing the requirement for placement of

targets on the part and therefore enabling a fully automated process. The structures e.g. barrel sections (as shown in Figure 1.1) will be placed on a rotary table so they can be turned around and measured.

AMS Scale Bar: The completion of the scale bar is the main objective of this PhD project. It will provide a directly traceable dynamic length scale which will be able to provide quasi-real-time uncertainty information. This is in contrast to traditional scale bars which, although calibrated in a traceable process, if damaged in a production environment can introduce errors into measurements based on that scale.

Photogrammetry: Provides large scale measurement of many targets simultaneously and links all the other systems together. When referencing a traceable scale bar it provides self-calibration with full uncertainty evaluation.

Laser Tracker: Provides highly accurate high frequency measurement for dynamic measurement of the robot enabling high accuracy machining.

Accelerometers: Provide very high frequency measurement of vibration for active vibration damping of the robot end effector while machining.

Work to be carried out at the University of Bath is broadly divided into three themes; the Absolute Multilateration between Spheres (AMS) scale bar; thermal compensation; and robotic machining.

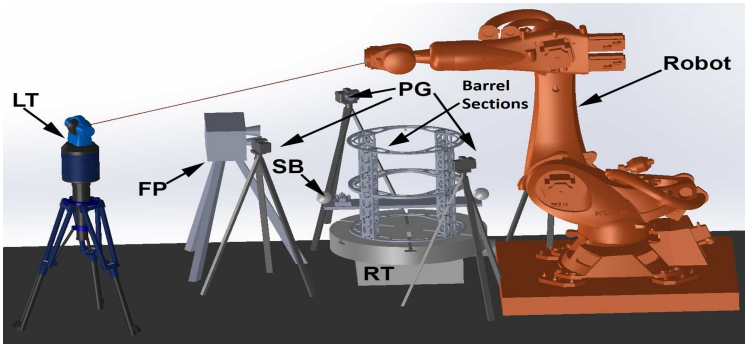

Figure 1.1 Demonstrator Cell Layout showing Laser Tracker (LT), Fringe Projections (FP), Photogrammetry (PG), Rotary Table (RT) with part mounted coaxially on its surface and Robot. The image is owned by the LCF group.

Initial system design and specification for the AMS interferometer has been completed during work for this PhD project, as well as experimentation on an optical bench. A working scale bar was then planned to be setup on a portable bench and moved into the demonstrator cell to provide a directly traceable length reference for large volume coordinate measurement systems. This final task is a work in progress.

A thermal compensation methodology has been developed by other members of the LCF group in collaboration with Airbus UK[11]. Uncertainty evaluation for the compensation is now required as well as integration with other measurement systems. Development of robotic machining is in the experimental phase using feedback from the laser tracker to correct path following errors. Subsequent work will involve integrating other feedback

from accelerometers and robot encoders where this will provide a benefit and carrying out uncertainty evaluation for the complete robotic machining process[12,13].

1.4 National Physical Laboratory (NPL) collaboration

This side project was not initially part of this PhD's research description and is not one of the LCF's research goals. Close collaboration with NPL on other research themes, resulted in a project that was born due to the need of a system that works alongside their frequency scanning interferometer and provides a reduced uncertainty in frequency measurements than their current system.

This part of the research involved the design and fabrication of optical fibres as well a series of experiments for filling these optical fibres with acetylene gas. The project was initiated by Ben Hughes and Michael Campbell, members of the Dimensional Metrology Group at NPL. Their main research interest is the development of novel techniques and instruments for providing measurements with minimum uncertainties in 1D, 2D and 3D over a range of scales i.e. from hundreds of metres down to picometres.

Their current system requires a way of monitoring frequency and frequency

stability of the operating laser. A hollow core fibre filled with a gas with absorption lines in the required range of the spectrum was the way to solve the problem. A reference cell (filled with gas) was already part of the setup[14]. However, using a fibre gas cell can provide these absorption lines with significantly less pressure (as the cell can be much longer). Therefore the pressure shift of the absorption peaks will be much smaller and the broadening will be less, compared to a standard reference cell. This means that the frequency of the laser can be determined with a smaller uncertainty.

Chapter 2

Distance & Position Metrology Techniques

2.1 Metrology

"When you can measure what you are speaking about, and express it in numbers, you know something about it; but when you cannot measure it, when you cannot express it in numbers, your knowledge is of a meagre and unsatisfactory kind" Sir William Thomson, 1883[15].

Metrology is the science of measurement (covering both theoretical and experimental aspects), which is also associated with the evaluation of the uncertainty of those two aspects. The theoretical part focuses on the fundamental concepts and principles of the study. Therefore it is a

requirement that the theoretical aspect will be functional and reasonable. As for the experimental part, it provides information about the variables of the study and tests the hypothesis[16]. Due to different levels of complexity and accuracy the field is divided in three sub-sections: Legal metrology with its main concern being the accuracy of measurements for the protection of life, health and public safety. Scientific metrology deals with organisation and development of standard measurements i.e. establishment of units of measurement. Finally, applied metrology, deals with measurement systems used in industry. Its main focus is to ensure the adequate functioning and production of the measured parts[17].

2.2 Interferometry

In this section the principles of interferometry are explained along with some specific features that are necessary to understand how the AMS interferometer works.

2.2.1 Basic Principles

The interferometer is a well known optical instrument which has multiple applications not only in the field of length metrology but also in fields such as physics, astronomy, engineering, sensing and medicine. It uses the phenomenon of interference of light waves to explore changes in

displacement. In the field of length metrology it is mostly used for calibration and motion control in order to achieve high precision in machining[18]. There are many interferometric designs with one of the most famous being the Michelson interferometer named after Albert Michelson, who was one of the first to demonstrate a measurement tool using interference of light, in 1880. The technique has undergone a lot of development over the years, especially after the invention of lasers[19].

An interference pattern can be produced by superposing two coherent beams of light, which are usually generated from the same light source. Noticeable changes in that pattern can be produced by changing the distance that one of the two beams has travelled (usually the measured arm of the interferometer, while the other arm stays the same - the reference arm). The two beams will recombine and therefore interfere before reaching the detector either constructively or destructively. Destructive interference indicates that the two beams are out of phase and therefore their amplitudes are cancelled out, resulting in a dark fringe in the pattern. If the interference is constructive, there will be a bright fringe in the pattern which means that the two beams are in phase[20].

The relative phase between the two arms of the interferometer will change

when there is a further displacement of the measurement arm. This will create a cyclic variation between constructive and destructive interference. Every time the path difference moves by a whole wavelength (increase or decrease) there will be a variation in intensity altering a bright to dark and back to bright fringe. Therefore, the movement of the measured arm can be determined by

$$d = \frac{\lambda N}{2n}, \tag{2.1}$$

where n is the refractive index, λ and d are the lasing wavelength in vacuum and displacement in micrometers, respectively and N is the number of half-wavelengths that can fit between the mirrors[21]. The AMS scale bar that was briefly mentioned in Chapter 1.3 (and will be explained in detail in Chapter 4) is an interferometer that measures the distance between two spheres, or for simplicity in this case the distance between two mirrors. A visualisation of this can be seen in figure 4.1. Therefore the optical path difference is 2 times the fit between the two mirrors which is equal to $2d$. A stable and well defined laser source is therefore crucial for the application of fringe counting. As mentioned earlier when an optical method is involved in distance measurements, the temperature and the refractive index can affect the stability of the system. In the same way, any frequency fluctuations caused by the laser can be interpreted as a change of the interferometric length (Equation 2.1). More information about the need of stabilizing an

optical laser can be found in Chapter 5.

The contrast of the fringe pattern is defined by the visibility (or interferometric visibility) V, and is given by

$$V = \frac{I_{\max} - I_{\min}}{I_{\max} + I_{\min}}, \tag{2.2}$$

where $I_{\max}$ and $I_{\min}$ are the maximum and the minimum intensity[21]. The fringe pattern produced by a monochromatic source should ideally have very high visibility.

In the next section a new type of fringe pattern is introduced which is what the AMS interferometer is generating due to the reflections off spherical surfaces.

2.2.2 Fringes and Newton's Rings

For two flat wavefronts (i.e. when the beams reflect off plane flat mirrors), an interferogram of straight, parallel, bright and dark bands will be formed (1D case with changes only in the z-axis). However, if the interference is being generated by reflections off a flat and a spherical surface, the fringes will be circular (3D case with changes in x- & y- axis). This phenomenon is called Newton's rings[22]. The AMS interferometer contains two spherical

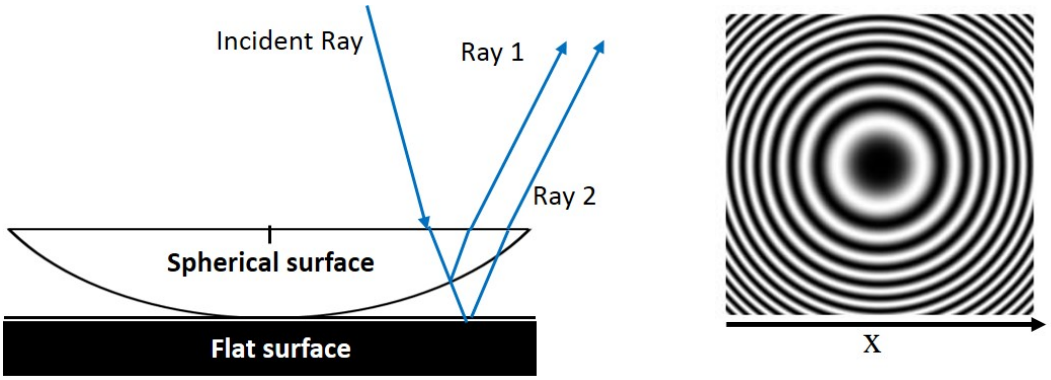

Figure 2.1 a) Schematic diagram of how Newton's rings are generated. b) Interferometric pattern of Newton's rings [23]

surfaces therefore it is important to consider this effect. At this point is worth mentioning that the interference fringes obtained by a Michelson interferometer are also circular. This phenomenon is completely different as these circular fringes are obtained due to angular changes (not positional - Newton's rings). As mentioned earlier, the AMS interferometer will be required to measure the distance between the centre of two spheres, therefore the interferometric pattern will be the Newton's rings. Figure 2.1a shows a flat surface placed very close to a lens. A thin air film is formed between the two surfaces, whose thickness increases as you move away from the centre. A ray of light hits the bottom curved surface of the lens where it gets partially reflected (follows path of Ray 1) and partially transmitted. The second beam gets reflected when it hits the second interface i.e. the flat surface (follows path of Ray 2). Interference pattern is generated with dark and bright rings (as the lens is

circularly symmetric) - see Figure 2.1b [23,24]. The central ring is a dark ring as destructive interference takes place. Refractive index plays the key role here. The air gap between the flat surface and the lens has to be tiny or infinitesimal at the centre. Assuming that the material of the lens and the flat surface is exactly the same e.g. n_{glass}, then n_{glass} is always bigger than the refractive index of the air, n_{air}. When a ray travels through a region of high refractive index and reflects off the interface with a region with smaller refractive index then there won't be any phase change at the boundary. However, the transmitted beam, which is now traveling in air, will impinge on an interface with the flat surface of higher refractive index. This will cause a 180° phase change. Considering that the path length difference of Ray 1 and Ray 2 at the centre is zero (or almost zero), this results in a dark fringe/spot [21]. Constructive and destructive interference will occur at:

$$2d_m = (2m + 1)\frac{\lambda}{2} \tag{2.3}$$

and

$$2d_m = m\lambda \tag{2.4}$$

respectively, where d is the thickness of the film and m is the order of interference [21].

The radii of the m^{th} bright and dark fringe are given by:

$$r_{m+\frac{1}{2}} = \sqrt{(2m+1)R\frac{\lambda}{2}} \tag{2.5}$$

and

$$r_m = \sqrt{m\lambda R} \tag{2.6}$$

respectively, where R is the radius of curvature of the lens. As the interference order increases, the fringes get closer together. This is because the diameter does not increase in the same proportion (see Equations 2.5 & 2.6). Dark and bright fringes will appear when a monochromatic source is used. Under white light the result is coloured fringes[22].

Understanding how Newton's ring behave is essential for the development of the AMS scale bar. Using equations 2.5 & 2.6 the distance between the fringes can be determined which is also what dictates the finite size of the detectors used in the AMS interferometer (more information about AMS can be found in Chapter 4).

The final part of this section focuses on the basic principles of the detection system of the AMS interferometer. The type of the interferometric fringe pattern does not affect the detection system. The way to create the quadrature detection for the AMS interferometer will be explained in

Chapter 4.

2.2.3 Quadrature Detection

Quadrature signals or $I.Q$ signals can be generated from an interferometric design. The purpose of creating a quadrature signal in length metrology measurements is to have an indication of the direction of the movement [25]. A pair of sinusoidal signals are 90° out of phase (as shown in Figure 2.2) and when plotted in an x-y mode a circle is formed. If the phase is not 90°, then the x-y mode forms an ellipse. Ways of generating this quadrature signal will be described later on (for a Mach Zehnder interferometer in Section 4.4 and for the AMS in Section 4.5). The $I.Q$ signal can also be used for length measurements, typically if fringe counting is the technique used [26].

For example, assuming that initial position of the blue signal is at point A (peak). If the interferometer moves left or right the power will drop with the same amount either way, meaning that it won't be possible to define the direction of the movement with just one signal. However, if another signal exists that is 90^0 out of phase, its intensity will either increase or decrease relative to the direction of the movement. This technique is very useful during fringe counting as the direction of the movement is required.

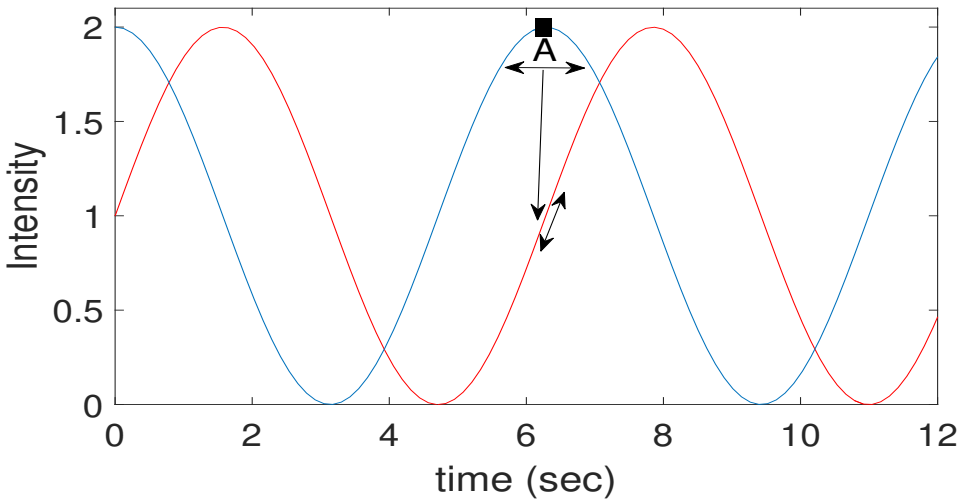

Figure 2.2 Quadrature detection of interferometric signals. When the blue signal is at point A, a second signal (red), that is 90° out of phase, can be used to determine the direction of the movement of the interference pattern.

In Section 1.3 the laser tracker and photogrammetry were briefly mentioned. Currently they are the state of the art systems for length metrology measurements, each of which has its own advantages and disadvantages (can be found in Sections 2.3.1& 2.3.3). As one of the main PhD project goals (AMS scale bar with an absolute distance measurement) is to surpass the accuracy of the laser tracker and photogrammetry, in a controlled environment, understanding their capabilities and limitations is necessary.

2.3 Absolute Distance Measurement (ADM)

Absolute distance measurements refer to the methods that can be used to determine a distance precisely usually through geometrical means or timing,

providing a value, along with its standard units[27]. As mentioned briefly in Section 1.2, the AMS interferometer will measure the distance between two spheres using an absolute distance measurement. The advantage of using an absolute distance measurement is that at any time during the measurement, if one of two spheres is removed, one can use the feedback to place the sphere back exactly where it was. Furthermore, the absolute distance is not retained, but can be re-acquired when the readout's power is switched back on again or when the line of sight is disturbed[28].

ADM is one of the main features of the laser tracker which was first implemented in the system in the mid 90's. During that time the state of the art of an ADM system was not fast enough to allow scanning over a surface. Therefore, the laser trackers used to include only an interferometer. However, within the last decade, the system has undergone intense development that increased its performance, allowing it to scan with high-speed (1000 points per second) and negligible loss in accuracy (0.025 mm)[29]. Nowadays the companies that make the laser trackers include only an absolute distance measurement system e.g. Faro Laser Tracker Vantage. Though the interferometers provide a better accuracy, they can only measure relative distance i.e. some calibration is needed and they cannot retain the measurements if the line of sight is disturbed. This is a major disadvantage

compared to the absolute distance measurement method, as the line of sight in a factory environment is easily disturbed [30].

2.3.1 Laser Tracker

The laser tracker was first introduced in 1987 and is a portable 3D measuring system that can provide effective and highly precise measurements of large objects. The system measures 3D coordinates with a spherically mounted retro-reflector (SMR), which seats on a 3-point conical land and is held in place by a magnet. The spherically mounted retro-reflector reflects the incoming beam back to its source along a vector that is parallel (and opposite in direction) to the incoming beam. The measurements are stored and shown on real time basis [31].

A starting point for the spherically mounted retro-reflector (home position) initiates the measuring process. The reflector is led to the measuring object and is moved around the area to be measured while the laser follows the movement of the spherically mounted retro-reflector (see Figure 2.3). Two highly precise angle encoders measure the elevation and rotational angles. The light reflects off the spherically mounted retro-reflector and enters the tracker where an absolute distance measurement or interferometer (or both) calculates the distance travelled. This procedure works well provided that there won't be any obstruction of the beam path between the laser tracker

and the spherically mounted retro-reflector (when the interferometer is used). In this case, the spherically mounted retro-reflector must be returned manually back to a home position (or any reference point) and start over. The tracker calculates the 3D space coordinate and up to 1000 points can be determined per second, therefore the movement of the reflector is fully tracked [29].

The distance measurement is a crucial process. This can either be achieved with the use of an interferometer, provided that the laser being used has a narrow spectral bandwidth (usually a stabilised HeNe 632.8 nm). The beam is split into two, one travelling inside the interferometer (reference arm) and the other travelling in free space. It will eventually reflect off the spherically mounted retro-reflector and return back to the interferometer. Light will then interfere and the signal will be analysed using electronic circuitry. As the SMR moves, the signal changes and the technique called "fringe counting" is used to determine the distance travelled [32].

The distance can also be determined using an absolute distance measurement. In this case, a modulated usually infrared laser (780 nm) is being used which will also reflect off the spherically mounted retro-reflector and return back to the tracker. The signal is then analysed in order to

determine the time of flight which is determined by the phase modulation of the beam. Finally, the position of the spherically mounted retro-reflector (and therefore the distance between the tracker and the spherically mounted retro-reflector) is given by multiplying the time of travel by the speed of light in air[33].

Many systems that were commonly used in the industry have been replaced by the tracker as it allows quick and easy measurement - it can measure a whole system with one laser position and there is no need to change the settings or set new references. Its efficiency can also be increased when using the absolute distance measurement method as it can measure multiple targets sequentially. The model that LCF uses (FARO ION) has 110 m (361 ft.) spherical working volume and can provide accuracy up to 20 µm plus 5 µm per meter[34]. This means that at any distance, however small, there is an uncertainty of 20 µm. Then there is an additional 5 µm for each meter. So 1 metre has 25 µm uncertainty. This a very good length metrology system that can provide readings with very high accuracy and potentially be better than the AMS system i.e. in a controlled environment. It does, however, require line-of-sight at all times which is a problem in a large scale manufacturing factory.

Figure 2.3 The FARO laser tracker following the SMR[34].

2.3.2 Frequency Scanning Interferometry (FSI)

In Chapter 1.4 a measurement system called FSI was briefly mentioned. FSI is a type of absolute distance interferometry, which is the most accurate and developed technique that can be used for an absolute distance measurement. It involves the use of an interferometer, with the optical components to be placed at each end of a line-of-sight of the distance to be measured and the laser source has to be a tunable laser (rather than a laser with a fixed wavelength)[35]. FSI systems are well known for their capability to provide high precision distance measurements even though there are several potential sources of uncertainties[36].

Figure 2.4 shows a simplified version of an FSI system - light from the tunable laser is sent simultaneously to the reference arm and measured arm of the interferometer. Usually a high-quality detection system is used to

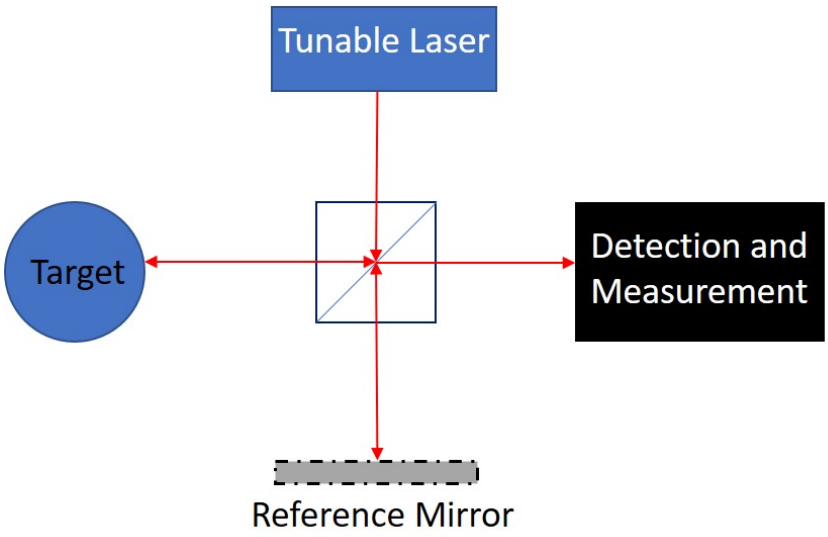

Figure 2.4 A simplified schematic diagram of an FSI system.

capture the signal from the two arms[37,38]. The data are collected and further analysis is required. Figure 2.5(a) shows the expected optical frequency signal reflected from the target and the mirror of the simplified FSI system.

The time difference between the blue and the red signal of figure 2.5a) is directly related to the distance to the target[36]. When light from a single target interferes with the reference signal, the intensity I of the signal is given by:

$$I(i,\tau) = A\cos[2\pi(\alpha\tau i + v_0\tau)]. \tag{2.7}$$

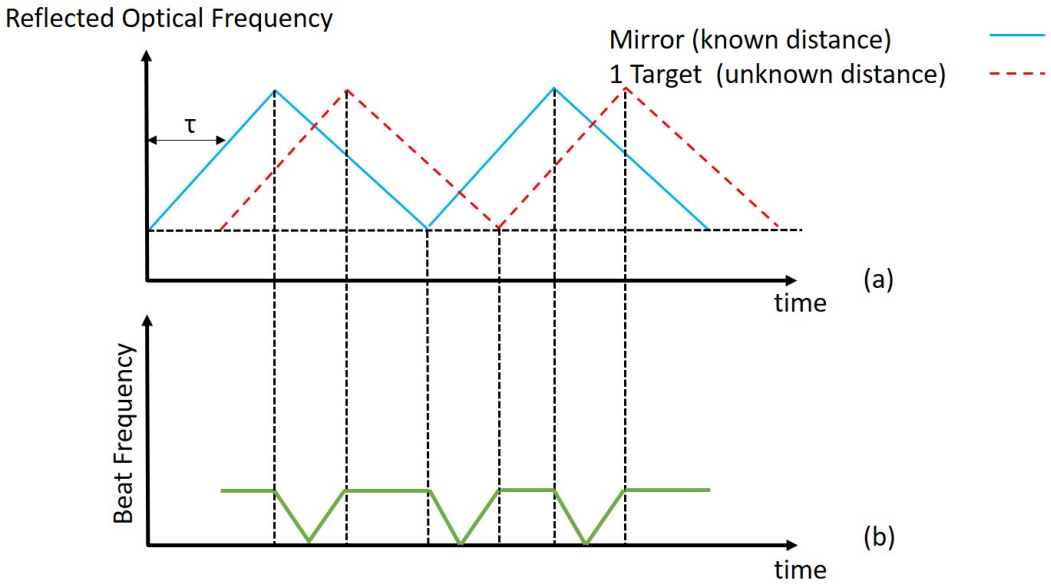

Figure 2.5 a)Expected signals reflected off of the mirror (blue) and target (red) in a simplified FSI system. The time difference τ is shown in the time axis b) Beat frequency of the two signals [36,39].

The frequency of the signal is defined by the sample index (i), the time of flight between the detection system and the target (τ) and α, the tuning rate of the laser frequency ($= dv/di$) [36,40]. A is the amplitude of the signal and v_0 is the frequency of the laser when i is zero. From equation 2.7, $\alpha\tau$ (the first term in the cosine) can be defined as f_{beat} and therefore the target distance (d) can be expressed as:

$$d = c\frac{f_{beat}}{2\alpha}, \tag{2.8}$$

where c is the speed of light in the medium (in this case air) [14,41]. Thus, the distance to the target can be determined from the frequency of the interference signal, provided that the laser tuning rate is known [14]. Figure

2.5(b) shows the beat frequency signal of the two signals shown in figure 2.5(a). This is the case when light from only one target is detected. When light from multiple targets interferes simultaneously with the reference signal, there will be a superposition of multiple f_{beat}(s) (each f_{beat} will be related to the distance between the sensor and each target). Therefore by taking the Fourier Transform (FT) of the interference signal, $\mathcal{F}(I)$, each peak can be traced back to each target as $\mathcal{F}(I)$ produces a signal in the frequency domain whereas the original signal is expressed in the time-domain (t). Then, a simple multiplication of $c \times \tau$ for each peak/target can determine the distance to each target.

In order to determine distance d accurately from equation 2.8 it is also necessary to know α, the tuning rate. The most common method and reliable technique for determining the tuning rate is by implementing a gas cell in the system[42,43]. A gas absorption cell has very well-defined absorption peaks and it only requires a very small amount of light to be guided through the cell whilst the laser is scanning. The absorption peaks at different pressures for different gasses, such as hydrogen cyanide and acetylene, have been characterised before by the National Institute of Standards and Technology (NIST)[44,45]. By fitting profiles to the absorption peaks, the peak line centres can be extracted which can be used to determine the tuning rate.

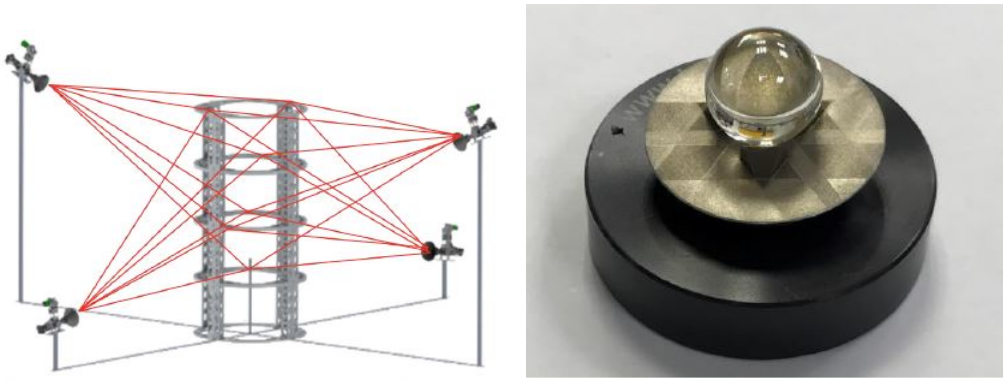

(a) (b)

Figure 2.6 (a) Four sensors placed around the object to be measured with the red lines indicating the distance between the multiple targets and the sensors (b) Spherical retro-reflector mounted in an adaptor used by NPL as target [40].

Figure 2.6(a) shows NPL's FSI system where 4 sensors are placed around the object to be measured. Retro-reflectors (in this case glass spheres) are used as targets and are placed around the object. The targets have fixed positions on the object and they can move with the object whilst being tracked. The retro-reflectors are mounted in an adaptor as shown in figure 2.6b. The sensors shine light on all targets simultaneously using an infrared laser. The distance between all sensors and targets is simultaneously monitored with the use of an infrared FSI system [14]. Each sensor is connected to a central control unit which monitors the 2 lasers and data acquisition system.

NPL uses an infrared tunable laser (New Focus TLM 8700) with 110 nm

mode-hop free tuning range and up to 2000nm/s tuning rate. Light from the laser is sent to the sensors using a single mode fibre (SMF-28), where ∼4% reflects back and is used as a reference signal for the interferometer[40]. The remaining light is guided from the sensors to the targets, where it reflects back into the sensor (and therefore the fibre) and interferes with the reference signal (given by equation 2.7). Their system can simultaneously measure multiple targets and therefore equation 2.8 can be used. The data can be further analysed using a computational model in order to locate the multiple targets in a unified coordinate frame. This process is called multilateration[40].

The method that NPL is using for determining the tuning rate is by implementing a gas cell in their system. Based on the operating wavelengths (1530-1565 nm), a hydrogen cyanide (HCN) gas cell is used and the intensity of the absorption peaks can be recorded whilst the laser is scanning (see figure 2.7)[44]. The absorption peaks are very stable and well known within this range, therefore by fitting peaks to the correct sample number (x-axis of figure 2.7) the tuning rate can be determined.

The main sources of uncertainty for this FSI measurement arise from the tuning rate and beat frequency (see equation 2.8). How well a beat signal

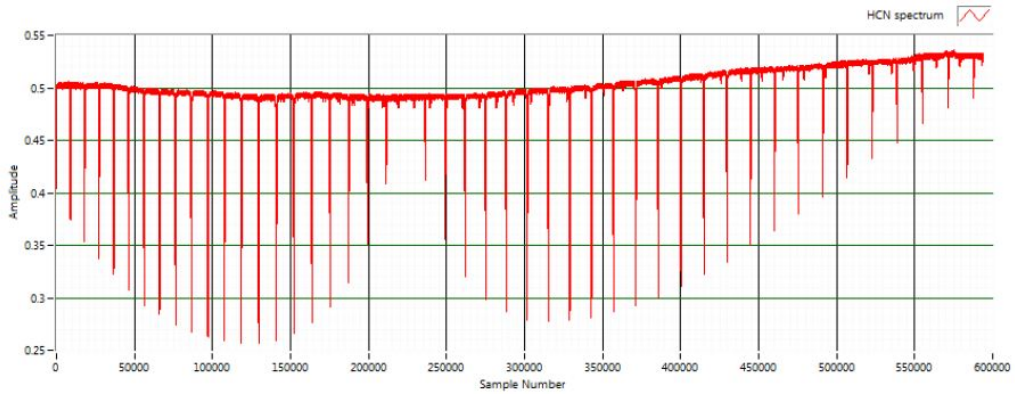

Figure 2.7 Absorption peaks of HCN recorded during the frequency scan [40].

can be extracted is dependent on the signal-to-noise ratio (SNR) of the signal [46]. For the beat frequency uncertainty it is important to maximise the signal strength and minimise the noise. Careful setup of the apparatus can help achieve this e.g balanced photodetectors can be used to remove common mode laser noise whilst the laser power is set to maximum. The setup is optimised for measurement target SNR [46]. It is worth noting that any other potential source of noise during the measurement will contribute to the final measurement uncertainty.

The other main source of uncertainty for this FSI measurement is the tuning rate which depends on the gas cell setup. Hughes *et al* estimated the uncertainty in the scale factor derived from the gas cell to be less than 1ppm (see figure 2.8) [40]. In this case the scale factor is the tuning rate of the laser. It is calculated by knowing the gas cell absorption peak frequencies and

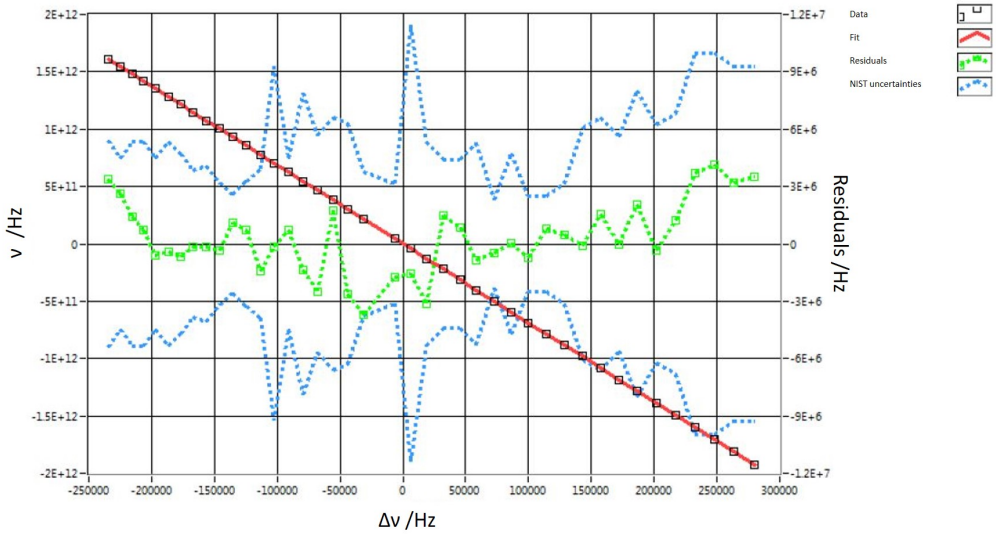

Figure 2.8 Experimental data for HCN gas cell. Red line: NIST calibrated frequency against fitted peak frequencies. Green line: residuals of red plot. Blue: uncertainties extracted from NIST calibrated frequencies [40,44].

where the centre of these absorption peaks are sampled during the laser sweep. Unfortunately there is an uncertainty in the peak frequency values and the fit to the absorption lines is not perfect. These errors combine so that when fitting the line of laser frequency with sample number, there is an uncertainty associated with the gradient of that line (the gradient is the change of frequency with sample). This is the scale factor uncertainty and if there is an error in the tuning rate of 1 ppm, it will contribute this 1 ppm to the distance measurement (see equation 2.8). This means that when measuring a distance as 1 m $\pm$ 1 ppm, there is an error of 1 micrometre.

This is NPL's system that will be discussed again in Chapter 6 where an acetylene fibre gas cell can be used to improve the uncertainty in the measurement of the system. There are multiple FSI techniques that are being used by different research groups to measure absolute distance. For example, the research group at CERN used their own technique to measure a 1195 mm interferometer to better than 250 nm [47].

FSI is one of the most accurate techniques for length measurements and can potentially be implemented in the AMS system. The main disadvantage of this method is that it can be slow and it is not a cost effective solution.

2.3.3 Photogrammetry

Photogrammetry or photographic metrology is another technique that can be used for determining the position between two objects. This technique requires multiple images (2D) of the same point of interest in order to reconstruct the 3D shape by intersecting the light rays in XYZ coordinates (triangulation). It involves the use of a camera which is not required to be at a fixed position, and usually hundreds of coded targets, for higher accuracy, on a large scale structure. The internal setting of the camera e.g. zoom and focus, are required to be fixed during a set of measurements. Its main applications are to measure deformation of objects (caused by thermal effects for example) and to monitor how the shape of an object (usually a solid

object) behaves in an unstable environment [48].

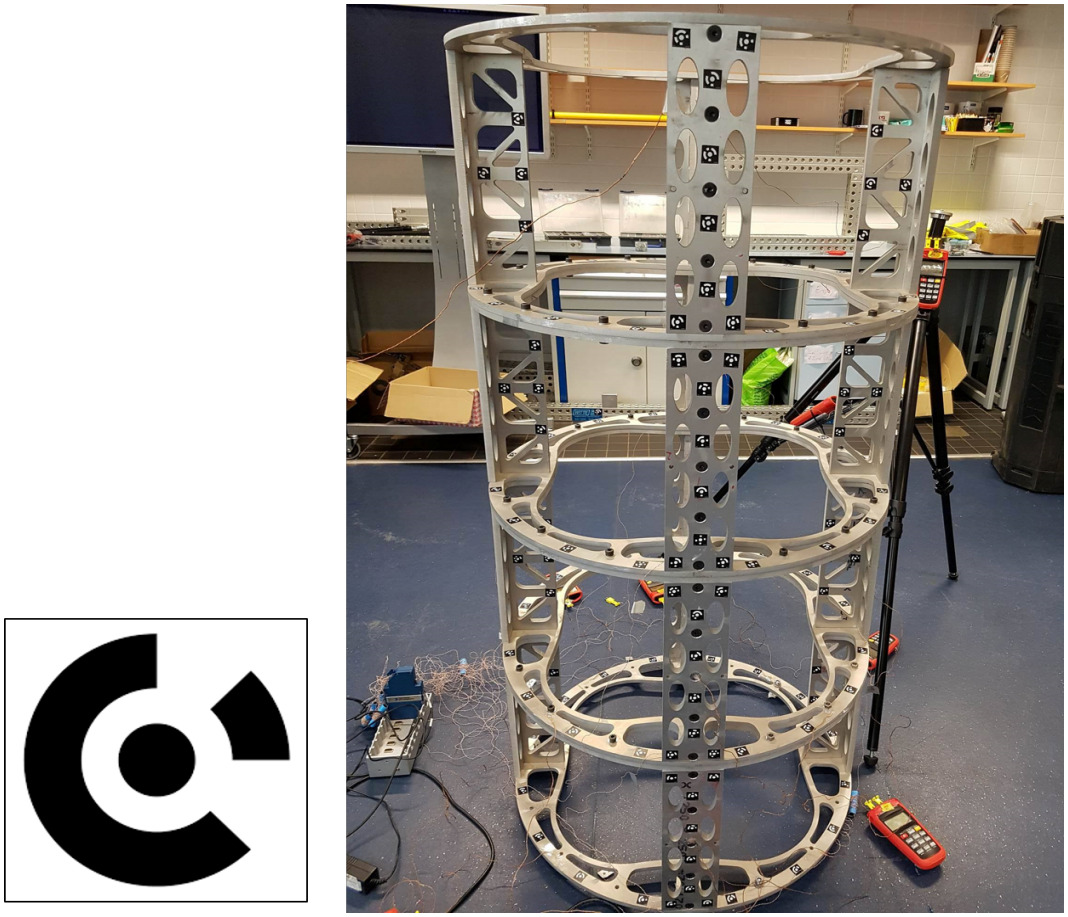

Figure 2.9 Left: Encoded target [49]. Right: Photogrammetry encoded targets stuck on the barrel sections.

A major advantage of photogrammetry over the laser tracker is the fact that it can record the entire point field in an instant (depending on the complexity of the object), provided that enough targets are being used - see Figure 2.9. In other words, the shape and any possible change in the shape of an object can be determined much faster compared to a laser tracker. For

large scale structures two scale bars and a cross (with five coded targets on each one) are used in order to set the coordinate system[50]. The technique called Bundle Adjustment (see Figure 2.10) is used to process the images and generate the coordinates (XYZ) of the measured points. The term refers to the bundle of light rays leaving a 3-dimensional object and converging at the centre of the cameras used.

The program will simultaneously self-calibrate the camera, triangulate all the points and resect the pictures. The resection is the procedure that determines the position of the cameras and their orientation as they can be placed in the same position but aimed in different directions. Self-calibration implies that the cameras will be calibrated during the measurements[51].

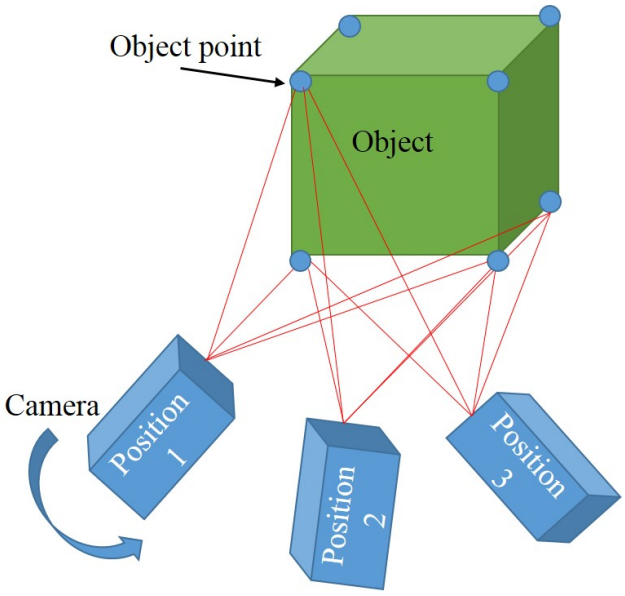

Figure 2.10 Example of bundle adjustment with 3 camera positions.

Another advantage of photogrammetry is the fact that it is a contact-free sensing technique. This can be extremely handy in cases where a hot or toxic material/object has to be monitored. The main disadvantages of this technique is that it requires a light source when used (therefore it cannot operate in a dark room) and the fact that there are occlusions and visibility constraints in a factory environment that can affect its performance. Furthermore, the laser tracker can provide a more accurate set of measurements for large scale structure as it only measures a single point. The uncertainty of the photogrammetry measurements is 10 µm plus 10 µm per meter[52]. As the camera does not require to be at a fixed position it is easy to overcome the line-of-sight issue with this technique. However, this technique, especially for a large scale structure, is limited by the properties of the camera i.e. pixels and resolution and it is also subject to environmental disturbances.

Chapter 3

Introduction to hollow core optical fibres

3.1 Optical Fibres

3.1.1 History

It is indeed remarkable how much progress has been achieved over the years in many scientific fields due to the use of optical fibre, a piece of glass with thickness almost similar to a human hair. Many scientists over the years attempted to control and confine light with Daniel Collodon and Jacques Babinet to be some of the first who proved that they can confine light with their water jets or the so called luminous fountains in the 1840's[53]. Later on, John Tyndall, demonstrated that light can be guided through a curved

water stream. William Walter, in the 1880's showed that you can use a series of pipes to guide light through a house. He placed an electric arc lamp at the basement of the house and used a series of pipes with a highly reflective coating. In 1888, Dr. Roth and Prof. Reuss from Vienna used bent glass rods to illuminate body cavities for medical applications. This was mainly used in dentistry and surgery as it allowed doctors to illuminate inside the patient's bodies. The idea inspired David Smith, who attempted to develop a dental illuminator based on bend glass rods. Arrays of transparent rods was the main mechanism behind Baird's patent for transmiting images for television, as well as for Clarence W . Hansell, who created facsimiles[53]. In 1930, Heinrich Lamm applied for a patent as he has proved that a bundle of thin transparent strand of glass can be used to transmit an image. He was aiming to use his invention in the medical field i.e. use these fibres to look inside the patient's body but World War II forced him to abandon his research. It is interesting to note that even today scientists are still working to optimise optical fibres for medical imaging i.e. for Lamm's original application[54]. Elias Snitzer in 1961 suggested that if the core of the fibre i.e. the central part of the glass is significantly small, only one mode can be guide down the length of the fibre, the fundamental mode. He was able to prove that this fibre can be used in medicine, however, its loss was too high and can not be used in telecommunications. A few years later, Charles Kao

and George Hockham, suggested that the loss of these fibres can be reduced by removing impurities from the glass[53]. It was not long until scientists at Corning Glass Works managed to resolve this issue by introducing titanium as a dopant in the glass. Therefore, in 1970 this group fabricated a fibre, which was ideal for applications in telecommunications as it was single moded and had less than a 20dB/km attenuation. Further work at Corning Glass Works resulted into further reduction of the attenuation loss by replacing titanium dopants with germanium[53].

3.1.2 Basic Principles

Conventional optical fibres are composed of glass, most often silica glass. The most common form of optical fibre is the step-index fibre. In a step-index fibre the core is surrounded by the cladding, as shown in Figure 3.1 and they have different refractive indices from each other due to the intentional addition of dopants in the glass. This difference of refractive index between the core and the cladding is the reason why light is trapped in the core. In other words, total internal reflection occurs at the boundary between the core and cladding and therefore the light is forced to travel down the length of the fibre. One can increase the refractive index of the glass by doping it with germanium or phosphorous or decrease it by adding dopants such as fluorine and boron.

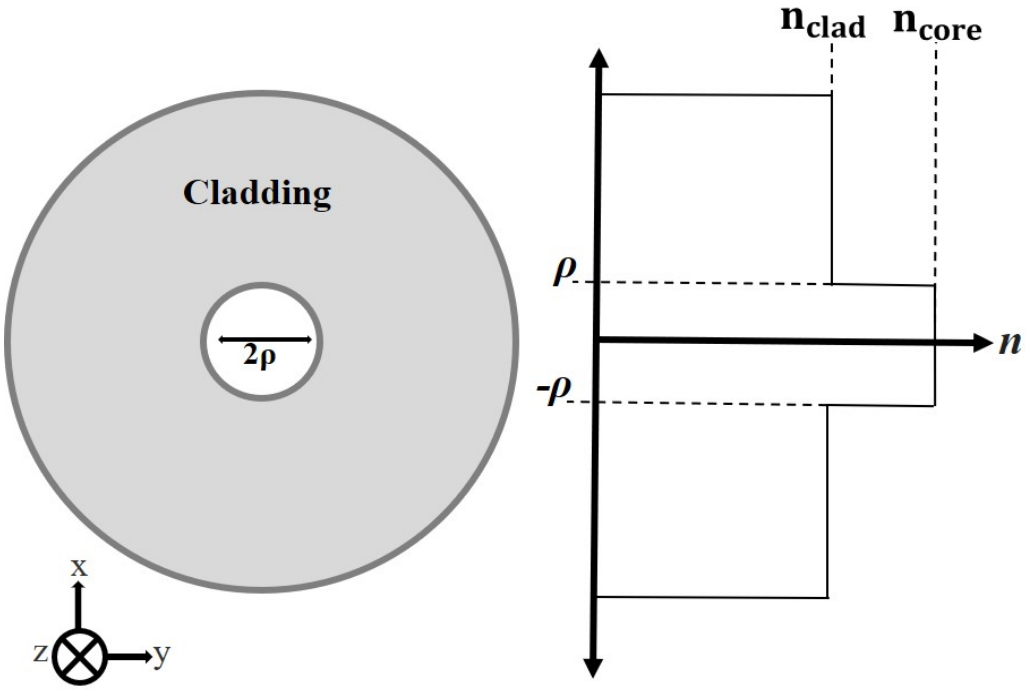

Figure 3.1 Transverse section of a fibre where ρ is the core radius.

However, the explanation above, has its own limitations. Light bouncing off the boundary and therefore being forced to travel down the length of the fibre is only valid when the core size is much larger than the wavelength of the propagating beam. In order to understand what happens when this is not the case, an explanation of the waveguide modes is required.

A mode is an electromagnetic field that can propagate through a waveguide with no change apart from its phase, and it is defined by:

$$\mathbf{E}(x, y, z, t) = \mathbf{E}(x, y)e^{\mathrm{i}(\beta z - \omega t)}, \tag{3.1}$$

where z is the direction of propagation, (x, y) is a plane parallel to the fibre's cross sectional area and β is the propagation constant. Using our knowledge from quantum physics and more specifically a finite potential well, one can relate the probability density to the intensity and the size of the potential well to the refractive index step change[55]. Within the potential well there is a finite number of bound states. These states have wave functions which do not change over time apart from their phase. It can be shown that the confinement of light in an optical fibre is directly analogous to a 1-D quantum well, as shown in Figure 3.2.

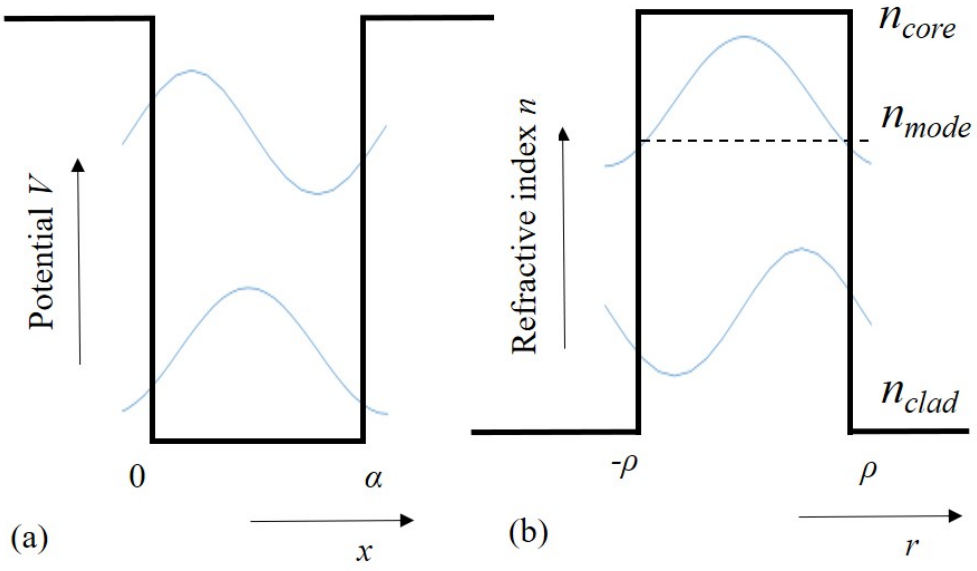

Figure 3.2 Schematic of (a) finite quantum well and (b) a mode field distribution inside a step-index fibre.

Propagating modes inside the fibre have an associated propagation constant,

β, and their mode index is given by:

$$n_{\text{eff}} = \beta/k, \tag{3.2}$$

where k is the free space wavevector. A step index fibre can support a finite number of bound modes and their propagation constants values are given by:

$$kn_{\text{clad}} < \beta \leq n_{\text{core}}k. \tag{3.3}$$

The mode with the highest β is called the fundamental mode. If only one mode is supported by the fibre (the fundamental mode), then the fibre is called a Single Mode Fibre (SMF). If more than one mode can be guided down the length of the fibre, then the fibre is known as a Multi-Mode Fibre (MMF).

3.1.3 Hollow Core Fibres

Hollow core fibres have been recently developed and have provided solutions to lots of different scientific fields such as medicine, defence, metrology and atmosphere monitoring. One of their main advantages over all the other types of optical fibres is that they can be filled with a controlled pressure of gas either for developing a gas laser or, for the purpose of this research, for extracting information regarding the stability and accuracy of the laser[56].

Figure 3.3 shows multiple designs of hollow core fibres[57]. As the core is

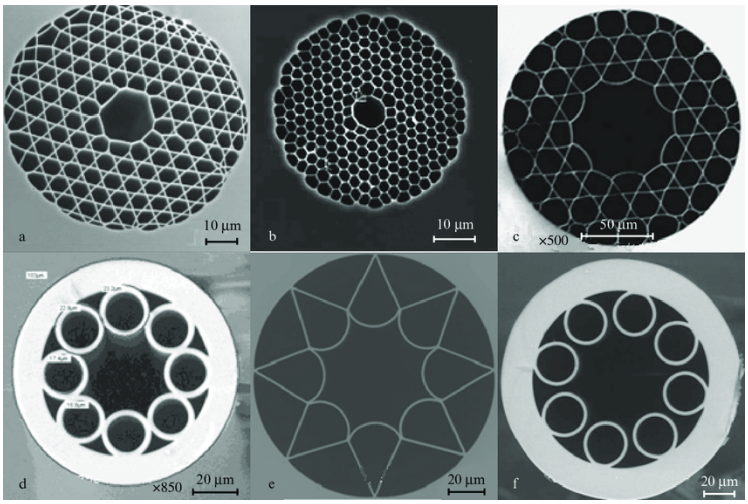

Figure 3.3 Cross section electron-microscopic images of hollow core fibre designs. a) Kagome lattice PCF, b) PCF with a hexagonal cladding structure, c) Kagome lattice PCF with a hypocycloid-shaped core–cladding interface, d) negative curvature anti-resonant guiding fibre, e) early tube lattice negative curvature fibre and f) eight-resonator free boundary fibre [57].

literally hollow, the guiding mechanism explained in Section 3.3.2 (total internal reflection) does not apply here as there is an increase in the refractive index from core (air) to cladding (glass). The guiding mechanisms that can explain the propagation of light inside most common hollow core fibres is anti-resonant reflection.

Anti-resonance (and resonance) refer to the phenomenon that occurs when a beam of light meets a dielectric material, in this case an etalon (two parallel highly reflective surfaces, as shown in Figure 3.4) [58]. At each interface, a fraction of the beam will reflect (r) and another fraction will be transmitted (t). The beams leaving the etalon will therefore have a fraction

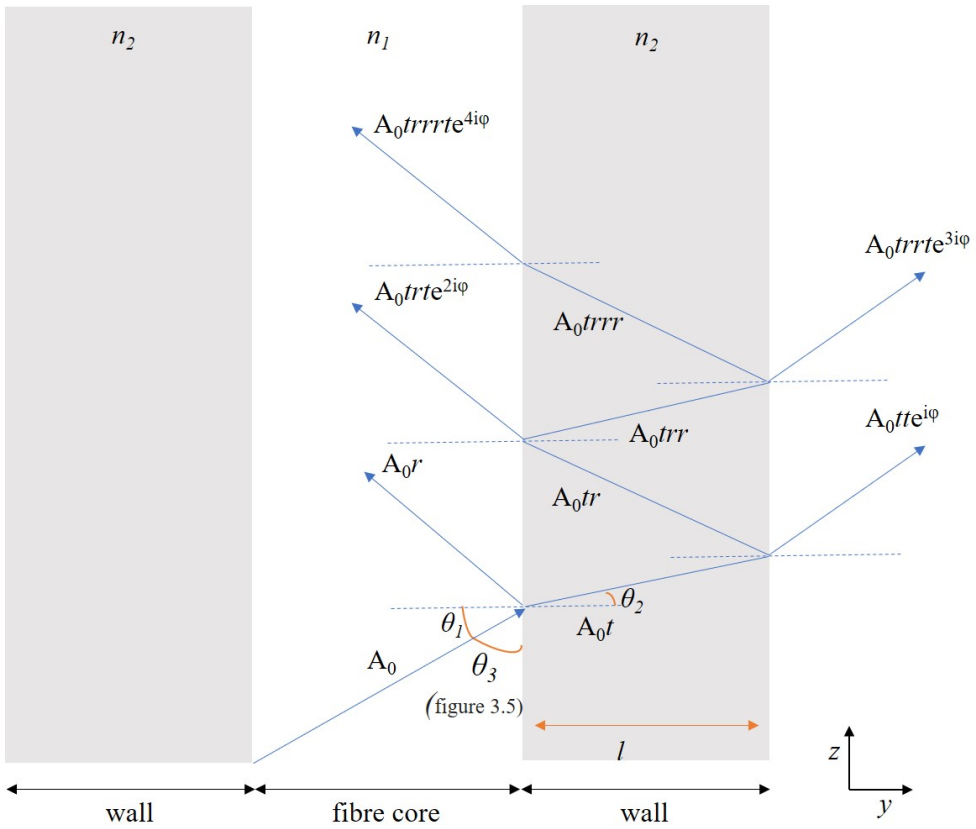

Figure 3.4 Reflection from two surfaces of a thin glass wall. A_0 is the amplitude of the incoming beam, ϕ is the phase and t and r are the transmission and reflection coefficient respectively.

of the amplitude of the incoming beam A_0, depending on how many times they travelled through the medium. They will also accumulate a phase ϕ each time they pass through the medium. The phase can take the form of:

$$\phi(\theta_1, l, n_2, \lambda) \tag{3.4}$$

where θ_1 is the angle of incidence of the incoming beam, l is the distance between the two reflective surfaces, n is the refractive index and λ is the

wavelength of the propagating beam.

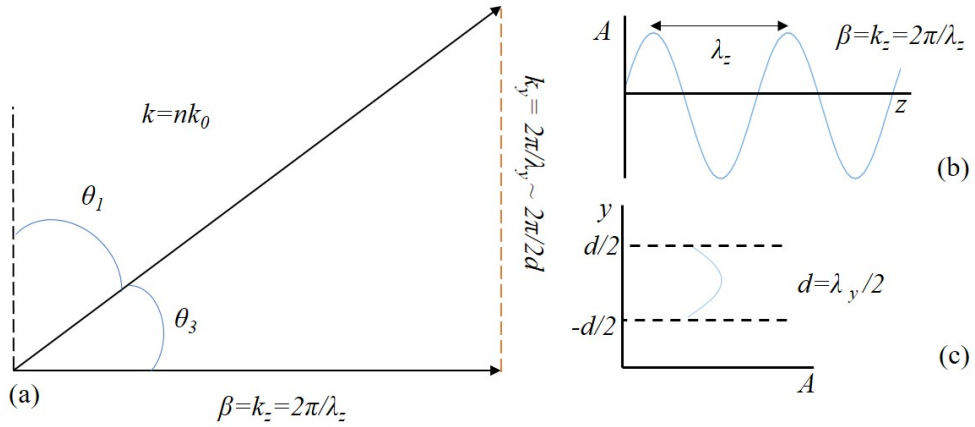

Figure 3.5 (a) Wave vectors in optical fibres. (b) Amplitude of propagating wave in the longitudinal axis. (c) Amplitude of the propagating wave in the transverse axis.

Marcatili and Schmeltzer, in 1964, published their findings regarding attenuation and bend properties of a hollow core waveguide[59]. Their model assumes that the core is surrounded by a uniform cladding of higher refractive index. One of their main conclusions was that attenuation α is directly proportional to λ^2/a^3 and this implies that attenuation can be highly suppressed by designing a hollow core fibre with core diameter that is much bigger that the desired wavelength ($d \gg \lambda$). However, they mentioned that a cannot take an arbitrary size and needs to be decided carefully as it causes higher bend loss which can limit the applications of the hollow core fibre[59].

Figure 3.5a shows the wave vector k inside an optical fibre. By following

Marcatili's and Schmeltzer's idea i.e. the core diameter $d \gg \lambda$, it suggests that $k_{\mathrm{y}} \ll k_0$. This can be explained by figure 3.5 b)&c) where the amplitude of a wave is shown in the longitudinal axis in b) and its wavelength is λ_{z}. However in the transverse axis (shown in figure 3.5c) only half a wavelength ($\lambda_{\mathrm{y}}/2$) can be fit between the core of the fibre (d) which means that $d = \lambda_{\mathrm{y}}/2$ and $k_{\mathrm{y}} = 2\pi/\lambda_{\mathrm{y}} \sim 2\pi/2d$.

In this case the angle θ_3 of the fibre is $\approx 0^\circ$ and the angle θ_1 in the Fabry Perot (Figure 3.4) has to be 90° (grazing incidence). When the phase $\phi = \pi$ the transmission (T) is maximum (in principle T=1) and this is essentially the condition for a resonance (all reflected waves interfere destructively).

The positions of the resonances are given by[60]:

$$2n_2 l\cos(\theta_2) = m\lambda, \tag{3.5}$$

where m is an integer and θ_2 is the angle of the propagating beam inside the etalon (figure 3.4).

For θ_1=90°, in a large core fibre

$$\frac{\sin(90)}{\sin(\theta_2)} = \frac{n_2}{n_1}. \tag{3.6}$$

Thus

$$\cos(\theta_2) = \sqrt{1 - \left(\frac{n_1}{n_2}\right)^2}. \tag{3.7}$$

Substituting this into equation 3.5 gives

$$\lambda_{\text{res}} = \frac{2n_1 d}{m}\left[\left(\frac{n_2}{n_1}\right)^2 - 1\right]^{1/2}, \tag{3.8}$$

where m is an integer, d is the layer thickness and n_1 and n_2 are the refractive indices of the waveguide core and anti-resonant layer respectively, it is possible to determine the position (and the edges) of the low loss anti-resonant bands of a hollow core fibre.

Figure 3.4 shows a single unsupported hollow core tube with no confinement that in theory should guide light at wavelengths defined by its wall thickness d. However, unless the core is perfectly suspended, the guidance properties will be negatively affected. This causes a manufacturability issue. Alternative designs are therefore required to overcome the need for structural support without affecting the guidance properties. Such examples are shown in figure 3.3. This thesis utilised designs containing resonators (the ring-like structures in figure 3.3 d, e and f) and for these designs the positions of the resonances are dictated by the thickness of the resonator rings.

Therefore when designing a new hollow core fibre that is required to guide light at very specific wavelengths, the use of equation 3.8 is essential. By plugging in the wall thickness (d) and changing m (integer number that defines the bands) the resonance wavelengths can be determined. Between these resonance wavelengths, a transmission band is formed. The same can be done in reverse i.e. when the edges of the transmission band (λ_{res1} and λ_{res2}) have been defined by the application, equation 3.8 can be used to determine the wall thickness in order to satisfy the application requirements.

Anti-resonant fibres have their drawbacks. There is a fundamental property in the nature of these anti-resonant reflections that affect the guiding properties of the fibres[61]. More specifically the modes are described as "leaky" and essentially Equation 3.1 is not appropriate. Instead, these leaky modes are described by the following equation:

$$\mathbf{E}(x, y, z, t) = \mathbf{E}(x, y)e^{\mathrm{i}(\beta \mathrm{z} - \omega \mathrm{t})}e^{-qz} \tag{3.9}$$

where q is the loss constant. Their leaky nature can be explained by referring back to figure 3.4 and the basic principles of the etalon. The transmittance function (T_{e}) of the etalon is given by:

$$T_{\mathrm{e}} = \frac{(1 - R_{\mathrm{e}})^2}{1 - 2R_{\mathrm{e}}\cos(\phi) + {R_{\mathrm{e}}}^2}, \tag{3.10}$$

where R_e is the reflectivity of the two surfaces (also changes based on the incoming angle) and ϕ is the phase difference between each successive transmitted pair given by:

$$\phi = \frac{2\pi}{\lambda} 2nl\cos(\theta_2), \tag{3.11}$$

where θ_2 and l are defined in figure 3.4[60]. Using equation 3.10, figure 3.6 was plotted for different values of R_e. From the figure it can be seen that the transmittance T_e (no matter what the value of R_e is) never goes to 0. As T_e=1-R_e, R_e can never be 1 for the etalon. This suggests that the transmittance of the fibre T_{fibre} will never be 1 (as R_e=T_{fibre}) and thus not a perfect waveguide (i.e. a leaky waveguide).

Furthuremore, an overlap of the leaky modes with the cladding structure can cause further leakage due to coupling with cladding modes. It was found that the mode overlap for the anti-resonant fibre can be reduced by changing the shape of the core boundary[63]. A hollow core fibre can have a positive curvature (figure 3.7a), a negative curvature (see figure 3.7c) or no curvature at all (see figure 3.7b). If the vector **R** (radius of the core) has the same direction as the vector **r** (radius of the curved surface) then the curvature is positive. If the directions of the two vectors have opposite signs then the curvature is negative and if there is no curved surface then the fibre has no

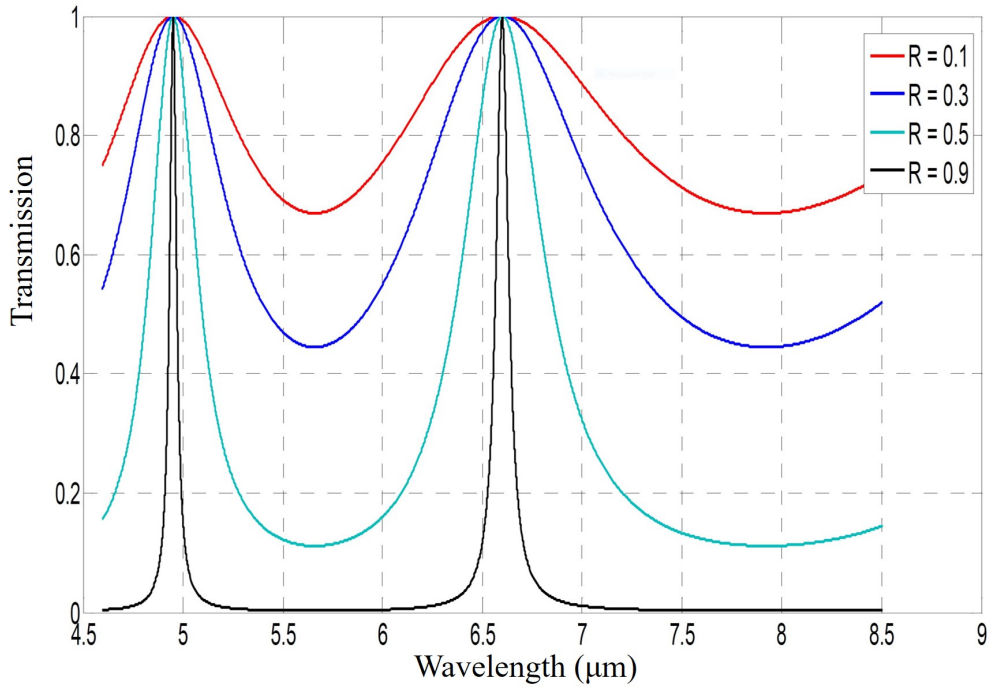

Figure 3.6 Transmission of the etalon for R=0.1,0.3,0.5 and 0.9. It can be seen that T reaches 1 but never 0 [62].

curvature. More examples can be seen in figure 3.3 where (a) has no curvature, (b) has a positive curvature and (c)(d)(e) and (f) have a negative curvature. If the design involves a negative curvature (similar to the design shown in Figure 3.3e), with the optimal core dimensions, the overlap can be reduced to less than 0.01%, whereas other anti-resonant designs can reach values that are as high as 0.5% [63].

In 2012 Yu *et al*, at the University of Bath developed a negative curvature fibre with one of the lowest transmission losses ever recorded at 3.04 µm ($34\,\mathrm{dB\,km^{-1}}$) [64]. However, the fibre was very sensitive to bend loss, 5.5 dB

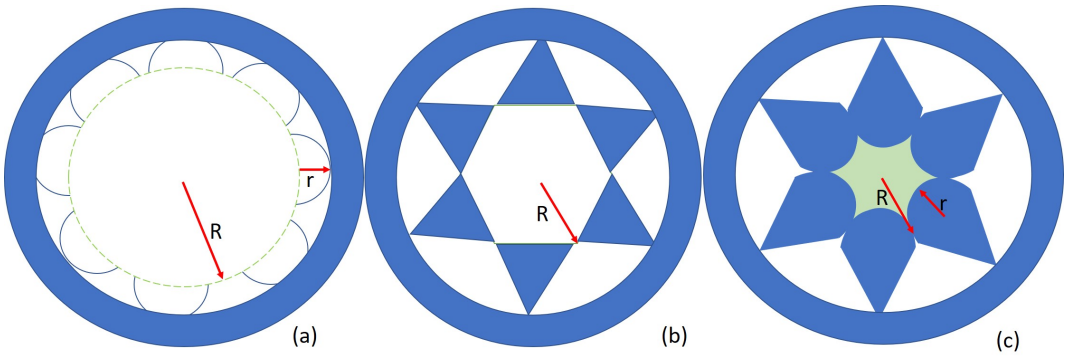

Figure 3.7 Definition of curvature in an optical fibre: a) positive curvature, b) no curvature and c) negative curvature.

per turn loss with a bend radius of 8 cm. It was then found that this leakage effect can be minimised by completely disconnecting the core structure, as in figure 3.8, where the resonators do not touch each other[64]. This new design is called "free boundary". An example of the capabilities of this design was demonstrated by Belardi *et al*, at the University of Bath as they presented a free boundary anti-resonant reflection fibre with 150 dB km^{-1} loss and 0.2 dB per turn bend loss at 3.35 µm (with an 8 cm bend radius)[65].

When fabricating a new hollow core fibre the design parameters that need to be considered are the thickness (d) and radius of resonators (r), number of resonator rigs (N) and core radius (R). These parameters can determine the application of the hollow core fibre. As shown with equation 3.8, the operating wavelengths are defined by the thickness (d) of the resonator rings. If the application requires a single mode hollow core fibre, literature shows

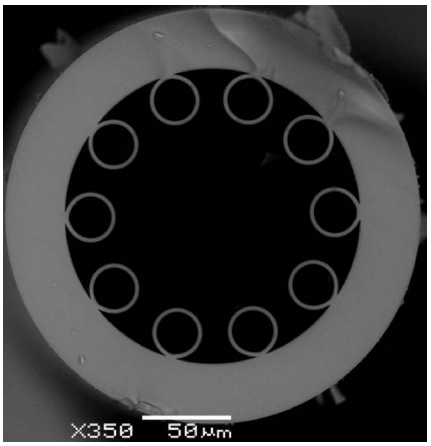

Figure 3.8 SEM image of a free boundary optical fibre [65].

that the ratio between the radius of the resonators (r) and the radius of the core (R) must be $\sim$0.66 [66]. To satisfy this condition it was found that the design must contain 6 or 7 resonators (N) [66]. It is also worth mentioning that this type of optical fibre does not have a cut-off wavelength. Furthuremore to achieve low attenuation, the diameter of the core has to be $\sim 30\lambda$, where λ is the operating wavelength [61]. It is also important to minimise the spacing between the resonators as the light confined in the core can escape through the gaps. A bigger gap between the resonators also has a negative effect on bend loss as well as a bigger core size.

3.2 Optical Fibre Fabrication

The CPPM group is housing a pair of state of the art optical fibre drawing towers that are constantly being used for the fabrication of microstructured

fibres e.g. hollow core fibres, PCFs etc. Microstructured is a term that refers to any fibre that involves a more complicated cross-sectional design than a step-index fibre. The process starts by taking a large glass structure called the preform, usually 1 meter long and 2 to 3 centimetres in diameter. The preform is then carefully placed vertically on top of the cane tower or fibre tower (Figure 3.9), by using the clamp. It is then slowly fed into the furnace which is usually heated up to 2000°C. At such high temperatures, the glass becomes very soft and eventually starts falling towards the bottom of the furnace. The laws of mass conservation suggest that if the soft preform is pulled out of the furnace at a higher rate that it is fed into the furnace it will reduce the diameter whilst maintaining the cross sectional refractive index profile. This process that involves the decrease of the preform size is called drawing and a typical desired diameter size (of the final product) for telecommunications is 125 µm. Once the preform is out of the furnace, it goes through a laser diameter monitor. Therefore the draw and feed speed can be adjusted in order to achieve the desired diameter. The system is not completely automated, therefore the presence of at least one person is essential. Dust and water are probably the biggest enemies during a fibre fabrication. For these reasons the process is taking place in a cleanroom and the preforms and each piece of equipment to be used are cleaned carefully with IPA. The fabrication towers of the CPPM group do not include a

humidity control system.

The most common technique for creating a hollow core fibre is the stack and draw method. For this technique, a macrostructure (or preform) needs to be build first and then draw it down to size. A macrostructure consists of a stacking tube, the resonators, the support rods and sometimes a jacket tube. Using the cane tower, the resonators and support rods can be drawn to desired size (2 mm-5 mm), using a tube which is 20 mm-30 mm in diameter (Figure3.10a). For a hollow core the structure is not self-supporting, therefore the support tubes are required. If the design involves, for example, 6 resonators, this means that a total of 13 tubes will be placed inside the stacking tube: 6 resonators, 6 support tubes (marked with blue Figure 3.11) and a core support. These two types of supports are extremely undesirable and usually their lengths are kept to the absolute minimum (10 cm-15 cm). They do however need to be placed at both ends of the stacking tube which is usually about a meter long, therefore about a third of the stack is scrap. Figure 3.10b shows how the stack looks, away from the support tubes. The stack is then loaded in the cane tower again and it is drawn to even smaller sizes. Once the supports have gone through the furnace, it is time to collect the interesting part of the remaining glass. These pieces can be manually cut after they pass through the puller belts. They usually are about a meter long

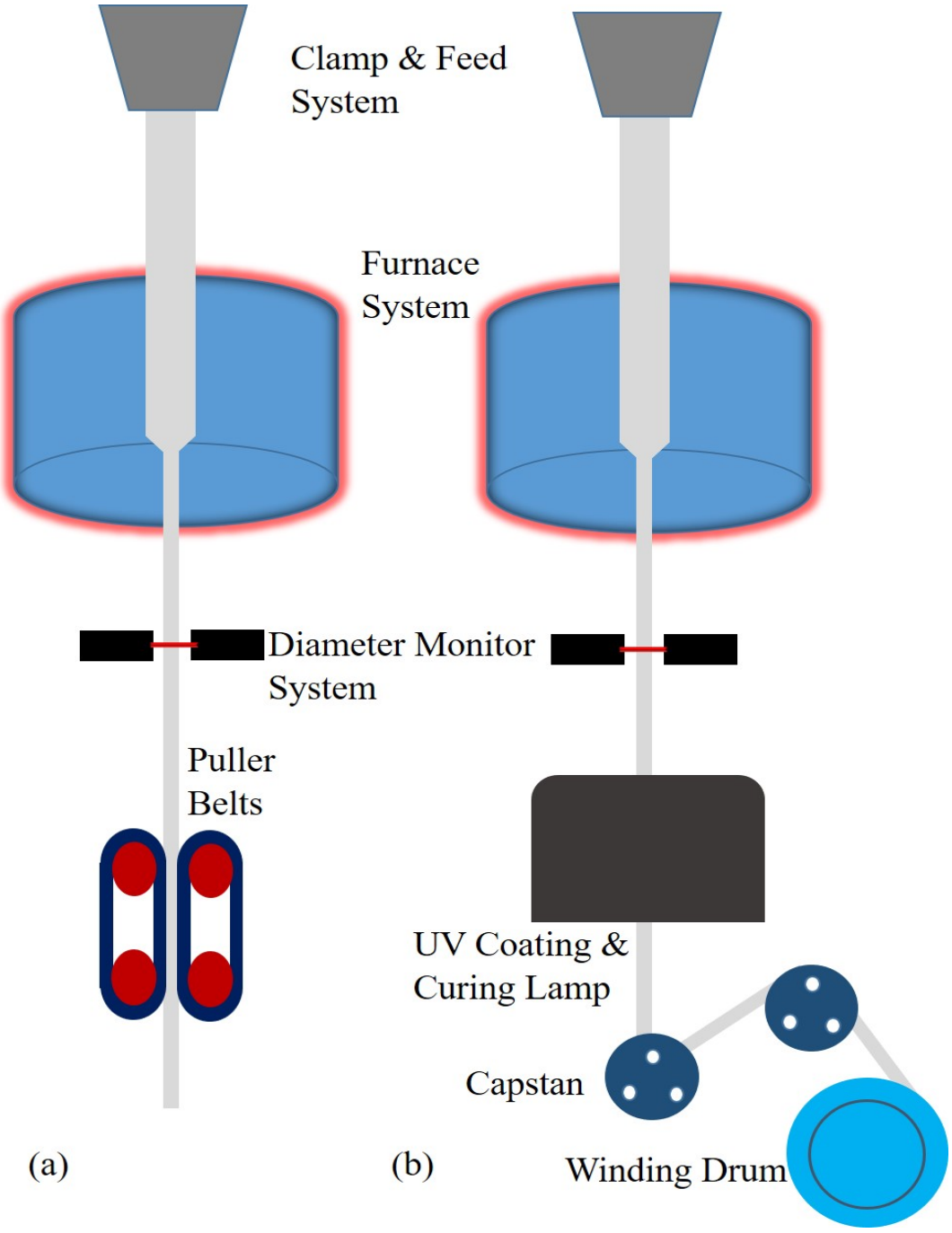

Figure 3.9 Schematic diagram of: a) the cane tower and b) the fibre tower.

and are called canes. The next step, though optional, is highly recommended as the addition of a silica jacket tube around the cane before drawing it down to fibre will provide extra support and prevent the fibre from snapping easily (see Figure 3.10c). For the next part, the fibre tower is used. The cane surrounded by the jacket is loaded and as the fibre comes out of the furnace (see Figure 3.10d), a UV curable polymer is applied on it for extra protection. As a single cane can provide a few hundred meters of fibre the capstans help to wind the fibre onto the collection drum. During the last fibre draw, pressure may be applied on the resonators in order to inflate them as well as a vacuum (away from the resonators) to remove any gaps between the cane and the jacket. Using this method a hollow core fibre was designed and fabricated, which will be discussed in Chapter 6, in order to develop a fibre gas cell for the NPL collaboration project.

3.3 Tapers

The term fibre tapering refers to the technique that can be used on any type of optical fibre in order to change their scale along the direction of propagation. Figure 3.12 shows a schematic of a simple taper structure with the transitions marked as b and d that connect the original uniform fibre size a and e to the waist of different diameter c. Depending on the application

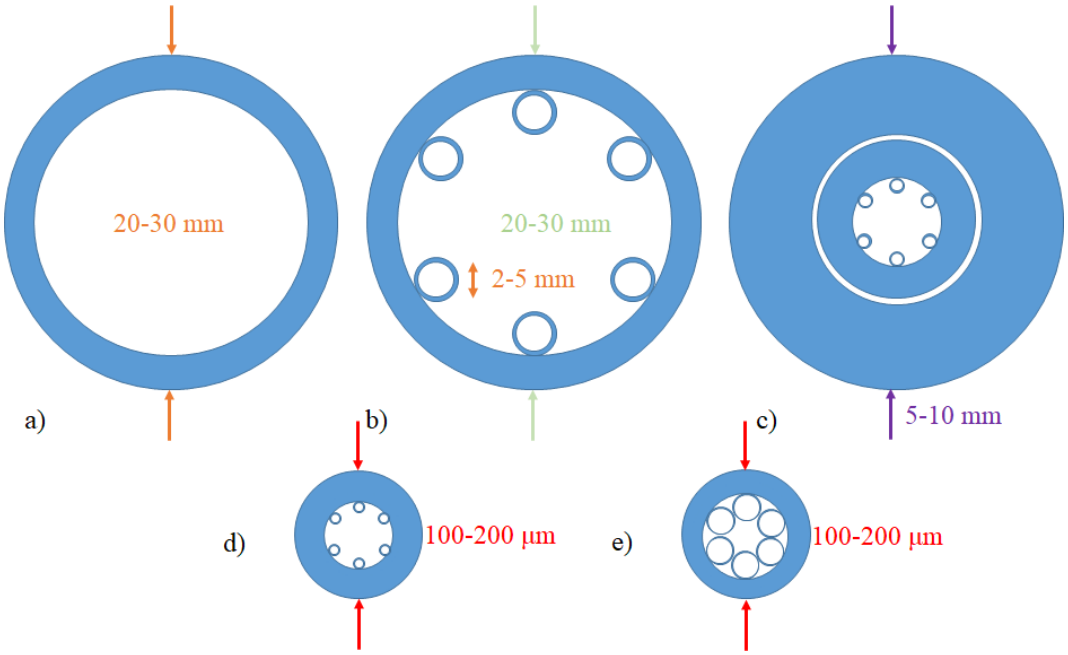

Figure 3.10 a) Tube used to draw the resonators and the supports, b) stack away from support tubes, c) cane with jacket tube around, d) fibre without any pressurisation and e) final fibre with pressurised resonators.

the structure shown in Figure 3.12 can be kept intact i.e. when the input and output coupling of the fibre needs to be kept the same but alter the dispersion or for optical couplers[67]. Other applications such as photonic lanterns require the taper to be cleaved at the waist (section *c* of Figure 3.12)[68].

The equipment involved in this process is shown in Figure 3.13 and it is broadly known as the taper rig. The basic principle involved in this technique is heating up part of the fibre whilst pulling along the ends. Thus the heated region will stretch to smaller sizes in diameter. The technique

Figure 3.11 Image taken at the end of a stack session of a 6 ring hollow core fibre. The tubes marked with blue are the support tubes, and in between them there are 6 resonator tubes. In the middle there is a core support tube.

that was used is called flame brush. The fibre is clamped onto the elongation stages as shown in Figure 3.13. A butane-oxygen flame is created on top of the burning stage and is manually pushed towards the fibre. The transverse movement of the flame as well as the movement of the other two stages is controlled by a computer. Controlling the speed of movement of the three stages allow the creation of even more complicated designs (i.e. multiple-waist taper). The burner is usually set to travel with a constant speed as this gives a uniform waist diameter[69]. Once the process is complete the burner stage is pushed back and the fibre can be unclamped. Tapers can be strong depending on their size, but most of the times they need to be

handled with great care in order to achieve the maximum durability.

In order to avoid creating lossy tapers it is essential to ensure gradual transition regions. In these regions the transverse geometry of a waveguide mode is not maintained. If the rate of change is slow enough the tapered fibre will be able to propagate the mode(s) without any loss. In such cases the taper transitions are known to be adiabatic.

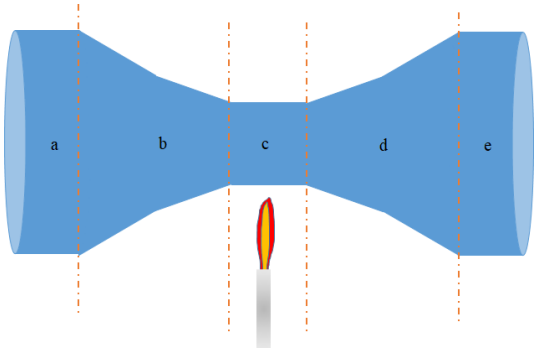

Figure 3.12 Schematic of a taper structure.

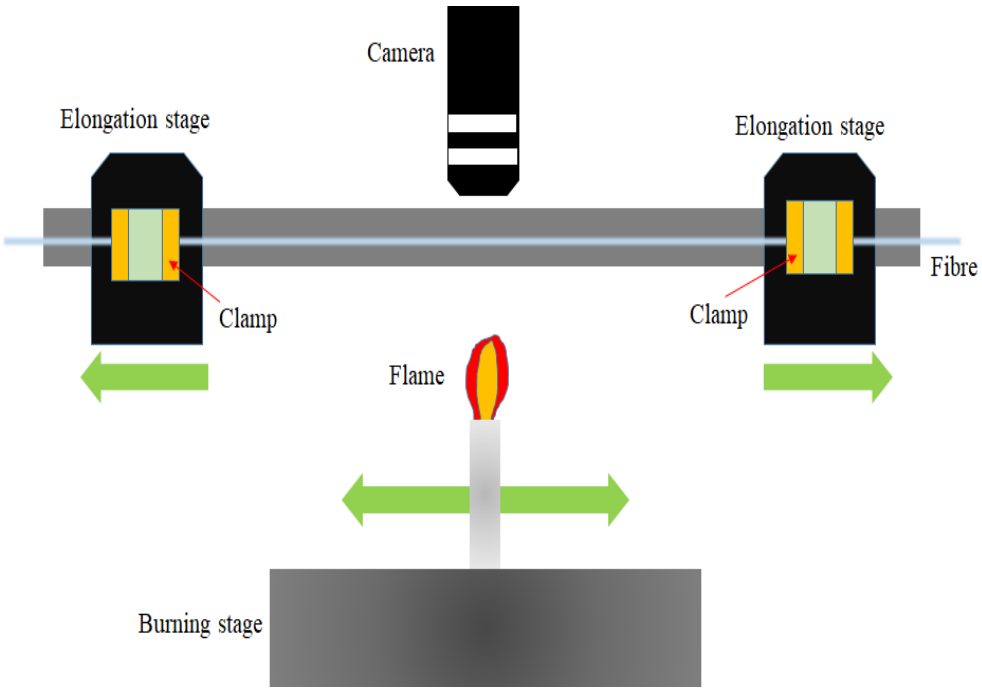

Figure 3.13 Schematic diagram of the taper rig. The fibre can be stretched between the two elongation stages whist the flame is heating a section.

Chapter 4

Developing the Interferometric models

The aim of this chapter is to explain the concept of the AMS model and the preliminary tasks (and their results) before building the final interferometer. The following analysis led to the publication of "Absolute multilateration between spheres" in Measurement Science and Technology journal [70].

4.1 The design

Environment is typically the limiting factor when thinking about accuracy of large scale coordinate measurements. A particular example is the Airbus aircraft production and assembly process, where different parts of the aircraft are being produced in different factories across Europe. The wing factory is

located in Broughton (UK), whereas the final assembly takes place in Toulouse (France). A system that will not be subject to environmental disturbances is required, which will also work reasonably fast. Currently, the laser tracker and photogrammetry are the most reliable systems for high accuracy measurements but they are still affected by temperature change[71,72].

The idea, which was first introduced and developed by Jody Muelaner (member of the LCF group) involves the integration of an absolute distance interferometer (as shown in Figure 4.1a) to measure the distance between two spheres.

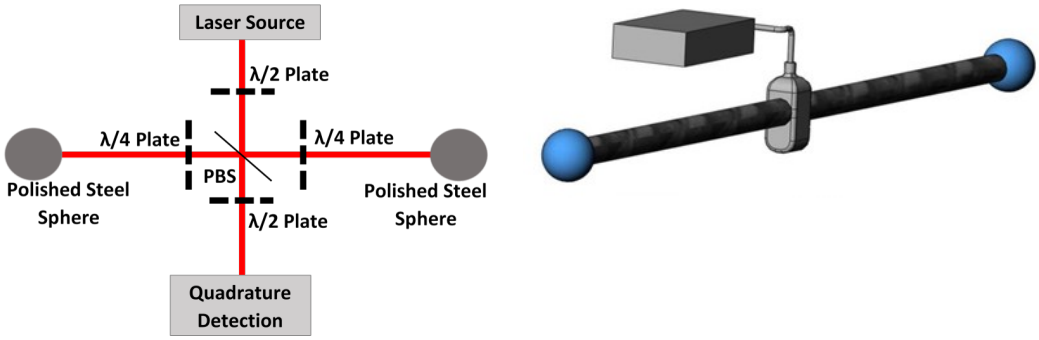

Figure 4.1 (a) AMS interferometric arrangement. The quarter ($\lambda/4$) and half ($\lambda/2$) waveplates, as well as the polarising beam splitter (PBS) were used to alter the polarisation in order to allow both beams to reach the detector. (b) Final Scale Bar. The path will be mechanically shielded[70].

The reference beam will travel in a straight line, from the source (which is fibre coupled) to the detector, whereas the beam that gets reflected off the

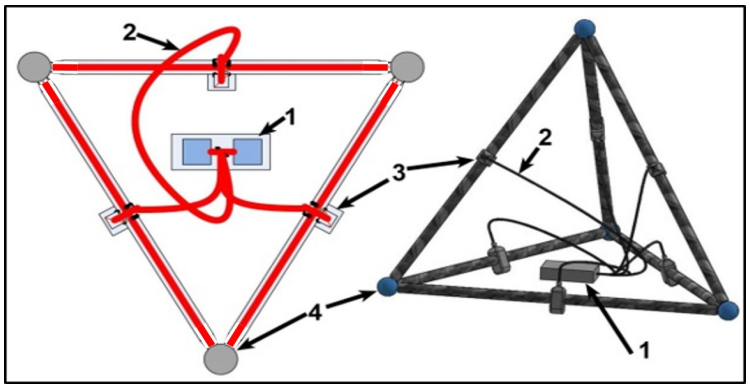

Figure 4.2 Network of interferometers measuring distance between spheres to give coordinate measurements; 1: source & splitter, 2: optical fibre, 3: interferometer optics of Figure 4.1a and 4: reference spheres [70].

polarising beam splitter (PBS) will travel between the two spheres before reaching the detector. When measuring the distance between two spheres their surfaces can be used as external datum while covering the laser path to avoid environmental disturbances (see Figure 4.1b). They can also serve as highly repeatable references and they can provide coordinate measurements through a trilateration network (and therefore multilateration - see Figure 4.2). Polished steel spheres are mass-produced with sub-micron accuracy for bearings, which means that in the case of a large scale structure, where cost and production are important designing factors, they are perfect to use. A network of spheres can then be built that provides information about the positioning of the structure at multiple points without requiring any temperature control and maintaining the line of sight during measurements. However, there is no record of research for ADM between two spheres. The

reason that they are not so commonly used in this field is due to the fact that they can cause significant divergence to a beam that reflects off their surface. The amount of power that reaches the detector when a beam reflects off a spherical surface is much smaller compared to a similar interferometric design that uses plane mirrors (or retro-reflectors) instead of spheres. Etalon has a system of one sphere and one retro-reflector.

A computational model is therefore needed to simulate various scenarios and find the actual power throughput and which feedback signals can be used to identify the optimal position on the surface of the spheres that the beam must reflect off, in order to achieve perfect alignment of the system. The distance between the centre of the spheres was initially modelled to be 1 m. This number does not have any particular physical meaning. It was chosen mainly because of its final application (see Chapter 7). Multiple scale bars will be used to cover a 25 m jig and therefore a smaller number will dramatically increase the cost which is an important designing factor, whereas a bigger number will increase the associated error of each scale bar.

4.2 The ray tracing model

The model, which was developed on MATLAB 2015b by J. Muelaner, uses vector geometry to simulate the divergence of the beam that travels through

the interferometer as well as the throughput power. The model initially simulates the position and direction of a single ray inside the AMS interferometer which can then be used with a numerical integration algorithm to analyse the behaviour of an entire beam inside the interferometer. The model assumes a standard telecoms laser (λ=1550 nm), a total path length of 2 m and an initially collimated beam.

Figure 4.3 shows the path of a ray as it travels within the AMS interferometer. If the interferometer is perfectly aligned a ray will travel from the source (A) to the beam splitter (B) then to a point on the surface of the first sphere (C - that point is also on a line that connects the centres of the two spheres). It will then reach the second sphere (D - at a point which is also on the line that connects the centres of the two spheres), reflect off the beam splitter (E) and finally it will reach the detector (F). To determine the ray path, the reflecting surfaces of the system were initially defined (plane of beam splitter & detector and surfaces of the spheres) in a vector form. The position of the laser A can then be chosen (with or without radial errors in the $y-$ and $z-$ direction) and the intercept between the plane of the beam splitter and the vector from point A to the beam splitter can determine point B. Similar analysis was done to determine the remaining ray path ($CDEF$).

In Figure 4.3 the system is not aligned and therefore the path is represented as $A'B'C'D'E'F'$. It is worth noting that the line $B'C'$ from figure 4.3 does not lie on top of the $C'D'$ line. This is to show that even a slight misalignment in the system can cause significant errors in the direction and orientation of the ray due to the highly divergent nature of the polished steel spheres. These significant errors can be seen on the plane of the detector as point F' can be found around the edge of the detector compared to point F (centre of the detector's plane). In an aligned system points B and E overlap.

The nominal distances AB (distance from the source to the beam splitter), CD (distance between the surfaces of the two spheres), EF (distance from the beam splitter to the detector) and the radius of the spheres (r) are used in order to describe the dimensional configuration and there are eleven parameters for describing alignment errors; position and orientations of laser and beam splitter and the position of the spheres. The outputs of the model are the coordinates of point F' and the path length error dL which is given by:

$$dL = (\mathbf{A'B'C'D'E'F'} - \mathbf{A''F'}) - (\mathbf{ABCDEF} - \mathbf{AF})\,. \tag{4.1}$$

The ray model can also prevent the generation of wrong data if the path BC and CD do not intersect with the first and second sphere respectively or if

path DE intercepts with the plane of the detector before the plane of the beam splitter or if the errors are so high that can cause reversal of the reflection direction of the ray when it hits the spheres.

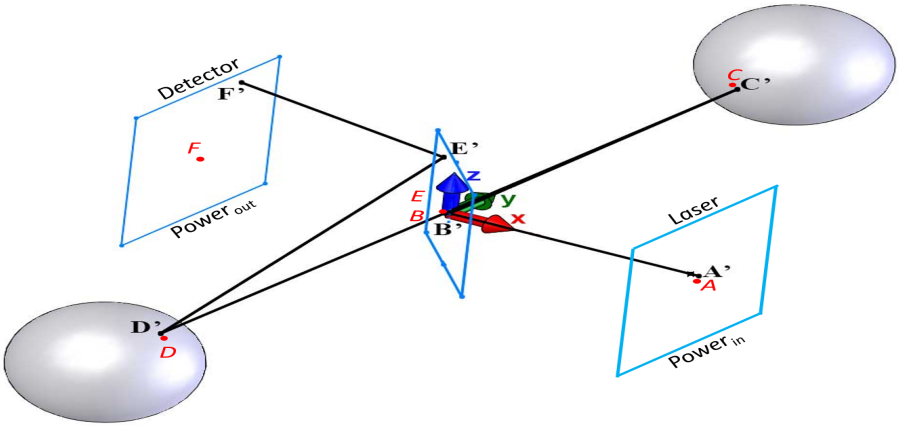

Figure 4.3 Representation of a ray path within the AMS interferometer model. The ray path for a perfectly aligned system is defined as $ABCDEF$ and for a misaligned AMS is defined as $A'B'C'D'E'F'$ [70].

The position on the detector and path length of a ray within a larger beam can also be determined using the ray tracing model. The beam was split into small areas of $dydz$. Numerical integration was used over the area of the beam that reaches the detector as the input beam was modelled with a Gaussian intensity profile. Therefore the power of each ray P_{ray} was given by:

$$P_{ray} = dy\ dz\ P_d\, e^{\frac{-{r_b}^2}{2 \cdot c^2}}, \tag{4.2}$$

where P_d is the peak power density of the input beam, $dydz$ are the step sizes between the integrated rays, r_b is the radial position of the ray within the beam and c is the Gaussian RMS width of the beam. The model first searches for the corners of the rectangle containing the detector and then integration is carried out within these bounds to determine the range in optical path errors across the detector, the mean path errors for all the rays and the throughput (fraction of laser power received at the detector). The range in path errors is an indication of whether or not we will be able to determine the fringes on the detector. The mean path errors (measured path errors) is an indication of how far away you are from measuring the correct distance (correct distance is the shortest distance). In order to be able to detect fringes, the range in path errors has to be less than the wavelength (see Equation 2.5&2.6 - the equations also determine the finite size of the detector). It was also assumed that the laser source, beam splitter and detector will be fabricated as a miniaturised photonic component with negligible internal alignment errors and it will be controlled with 4 degrees of freedom (DOF) in order to achieve a perfect alignment between the two spheres. The alignment of this assembly was therefore modelled with translation and rotation in/about the $x-$ and $z-$ axis of Figure 4.3.

Many simulations were then carried out in order to investigate the accuracy

of the model and whether it can be possible to use its feedback to align an interferometer. For the analysis in Section 4.2.1, the AMS interferometer was modelled with: AB=10 mm, CD=1 m and EF=10 mm.

A final point of discussion for this section is the effect of the dispersive elements of the interferometer (polarising beam splitters and wave plates) on the optical path difference of the interferometer, the interferometric signals and therefore the uncertainty in the measurement. Table 1 in Muelaner *et al* shows an uncertainty budget for independent uncertainties for an AMS scale bar[70]. Factors such as glass coefficient of thermal expansion (CTE), temperature expansion and index change have a minimal effect on the uncertainty measurement (0.02 µm). From Table 1 it can be seen that the source of the biggest uncertainty arises from the CTE of the Sphere (value of 1.00 µm/m/°C gives a standard uncertainty of 0.30 µm).

4.2.1 Optimising the model

The first step was to determine whether the size of the sphere and detector play a crucial role in the interferometric arrangement. It was found that the size of the spheres has a negligible effect on the range in path errors, whereas the detector size is crucial. Figure 4.4 shows a graph of range in path errors against detector radius. It can be seen that for a perfect alignment, a detector of approximately 1.2 mm radius will produce a clear signal (range in

path errors must be less than the wavelength). This is a reasonably large detector. However, the larger the alignment errors that the interferometer must cope with, the smaller the detector must be to produce a clear signal for fringe counting. When initial alignment errors are present e.g. 1 mm in translation and 0.1 degree in rotation, the detector radius must be reduced to no larger than 0.1 mm to achieve a clear signal (path difference $< \lambda$). The radius of the spheres was 50 mm for this simulation. Detector size is a compromise with smaller sizes receiving less laser power. This is a concern since the highly divergent nature of the spherical reflector surfaces means that very significant power loss takes place over the AMS interferometer. The radius of the spheres can also affect the amount of power that is reaching the detector (see Figure 4.5). The detector radius was 0.05 mm for this simulation.

A possible way of increasing the power i.e. by changing the position of interferometric assembly between the spheres was investigated. The position I_p was defined as the distance between the beam splitter (BS) and the surface of the first sphere as a proportion of the total distance CD (distance between the two spheres). This can be seen in Figure 4.6. For both cases (aligned and misaligned), the fraction of laser power that is reaching the detector can be increased by placing the structure closer to the second sphere

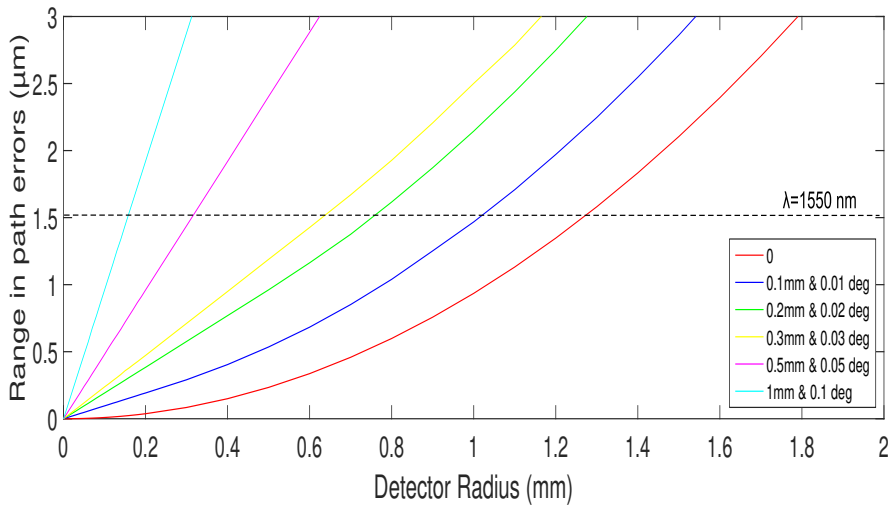

Figure 4.4 Effect of detector radius on the range in optical path for the rays received by the detector with sphere radius r=50 mm.

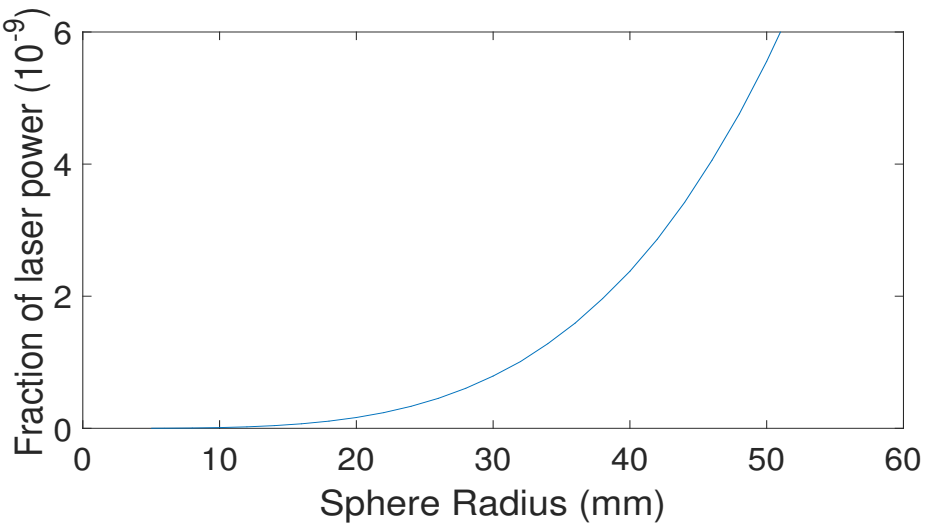

Figure 4.5 Effect of sphere radius (r) on power loss, with a detector radius of 0.05 mm and alignment errors of the interferometer optical components relative to the spheres of 1 mm in translation and 0.1 degree in rotation.

(95%). Comparing the 50% case (structure in the centre) with the 95% for the aligned system, it can be seen that the power increases by almost three orders of magnitude.

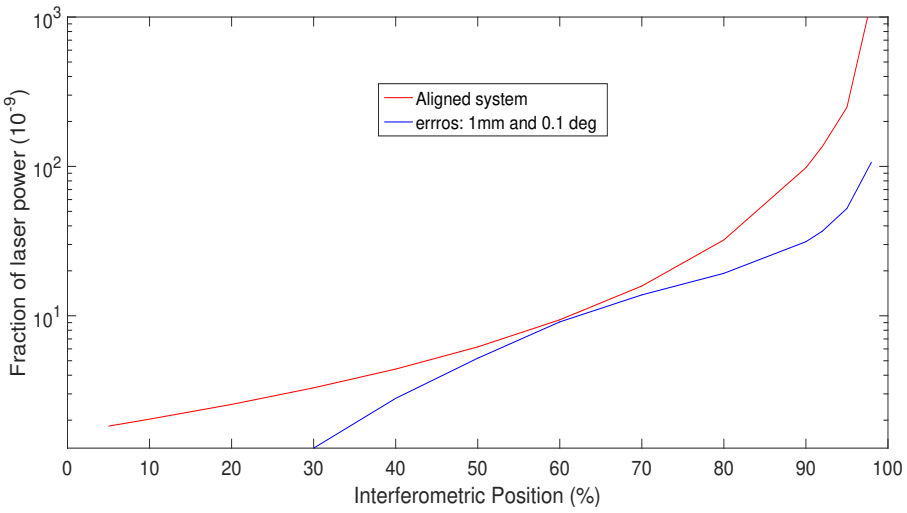

Figure 4.6 Effect of interferometer position on power loss, with a detector radius of 0.05 mm and 50 mm spheres.

From the investigations that were described above, it was decided that for the initial interferometer the radius of the spheres and detector will be 50 mm and 0.05 mm respectively, and the 95% interferometric arrangement will be used. Larger spheres involve significant thermal expansion and weight, both of which are problematic. Placing the interferometer closer than 50 mm from the surface of a sphere will present problems for the packaging of components. As mentioned earlier the path will be mechanically shielded to avoid environmental disturbances.

The next investigation was to determine whether or not this model is suitable for using feedback to align the system. Perfect alignment might be expected to result in maximum power at the detector. Figure 4.7 shows the three outputs of the model for a misaligned scenario with translational errors of 1.2 mm in x and z and 0.1 degrees in $x-$ rotation while $z-$ rotation is changed. The power graph (red plot shown in figure 4.7) is the fraction of power at points F' and A' of figure 4.3. This plot can be used to decide in which direction the system must be rotated in order to provide maximum power at the detector. In this case, it suggests that it should be rotated in the $z-$ direction to a value of 0.125 degrees. However, by checking the mean path errors graph (blue plot of figure 4.7), it shows that moving towards the peak of the power graph will actually induce a bigger error to the system. The peak of the power graph (z=0.125 degrees) does not occur at the same place as the minimum of the mean path errors graph (z= -0.04 degrees). Therefore it can be seen that local maxima occur with opposing translational and rotational errors. In other words, it is possible to find a local maximum power while there are significant errors in the measured path. Thus the path length must be used as feedback for alignment (by locating the smallest value) while keeping an eye on potential reductions in power that can cause detection issues. Minimum path length is the distance from the closest point

on the spheres, which gives the line between sphere centres that is needed for AMS.

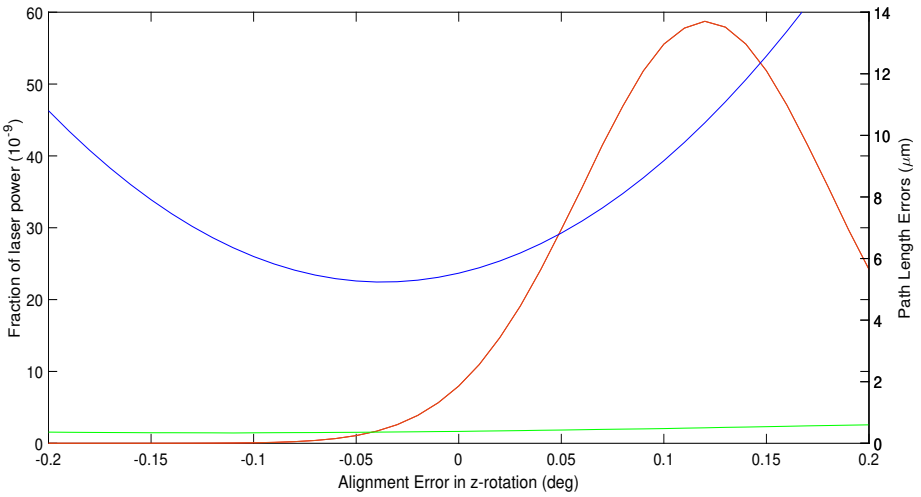

Figure 4.7 Results of interferometric alignment. Fraction of laser power (red), Mean path errors (blue), Range in path errors (green).

Table 4.1 Simulated alignment with 95% Interferometric Position. dIx = transalation in x-axis, dIz = translation in z-axis, dIrx = rotation about x-axis, dIrz = rotation about z-axis, meanE = mean path errors, RangeE= range in paht errors and TotalP = power throughput.

	dIx	dIz	dIrx	dIrz	meanE (μm)	RangeE (μm)	TotalP (10^{-9})
Initial	1	1	0.1	0.1	15.9	1.73	52.3
1^{st}	0.037	-0.001	0.019	-0.037	24.2	2.36	4.02
2^{nd}	-0.001	-0.001	-0.001	-0.001	0.008	0.02	248

Table 4.2 Simulated alignment with 90% Interferometric Position. dIx = transalation in x-axis, dIz = translation in z-axis, dIrx = rotation about x-axis, dIrz = rotation about z-axis, meanE = mean path errors, RangeE= range in paht errors and TotalP = power throughput.

	dIx	dIz	dIrx	dIrz	meanE (μm)	RangeE (μm)	TotalP (10^{-9})
Initial	1	1	0.1	0.1	12.5	1.17	31.3
1^{st}	-0.151	0.469	0.075	-0.065	2.85	0.45	9.20
2^{nd}	-0.047	0.271	-0.120	0.010	2.17	0.09	3.01
3^{rd}	-0.017	0.085	-0.020	0.003	1.05	0.38	23.0
4^{th}	-0.004	0.021	-0.005	0.001	0.107	0.12	86.3
5^{th}	0.000	0.003	-0.001	0.000	0.011	0.03	97.4

A simulation of an alignment process was then performed with a misaligned system of 1 mm in translation (x and z) and 0.1 degrees in rotation ($x-$ and $z-$). The alignment process was simulated by taking a sequential and iterative approach. Each DOF was moved through a series of discrete steps either side of its current position, for example the rotation about z was simulated from -0.2 to +0.2 degrees with a step size of 0.05. A quadratic was then fitted to the three sets of output data and the optimal position was located at the point where there was a clear signal (fraction of power must be greater than 10^{-9}, range in path errors must be less than 1.5 µm and mean path errors must be as small as possible). This process was then repeated sequentially for each DOF in alignment. The iterations were repeated until the system converged towards a perfect alignment. Muelaner *et al* have defined perfect alignment

as system with less than 0.5 µm uncertainty for a scale bar (i.e. mean path errors ∼0.5 µm)[70]. Table 4.1 & 4.2 give the results of this process with the interferometer positioned at Ip=95% and 90% respectively. It can be seen that after only a few iterations the mean path errors drop below the required number. Furthermore, the power throughput of the system can potentially be a problem (i.e. photon shot noise was considered as potential limiting factor), but provided that the input power is high enough this should not be a concern. For the simulation the input power was set to 1 W. We have therefore shown that it is feasible to align the system using the mean path errors as feedback, whilst maintaining sufficient power for detection.

4.3 Gaussian Beam model

A way of confirming the validity of the ray tracing model was by creating another model using basic Gaussian beam equations (this includes diffraction which is the main difference from the previous AMS model). Ray transfer matrix analysis (ABCD matrices) were used to simulate how the optical components of the interferometer and the spheres will affect the incoming beam. The procedure requires the user to give the input beam size (w_0) and its radius of curvature (R_{in}). The ray tracing model uses an initially collimated beam i.e. $R_{in} = \infty$, which was represented with $R_{in} = 10^6$ in this model. Different scenarios were simulated by varying the value of R_{in} while

the model calculates the fraction of output power, the Rayleigh length of the input beam (z_{Rin}) and the focal position relative to the input (z). The model can also simulate the range in path errors (defined in Section 4.2 and shown in Figure 4.8) but is not able to simulate the total beam path length (mean path errors).

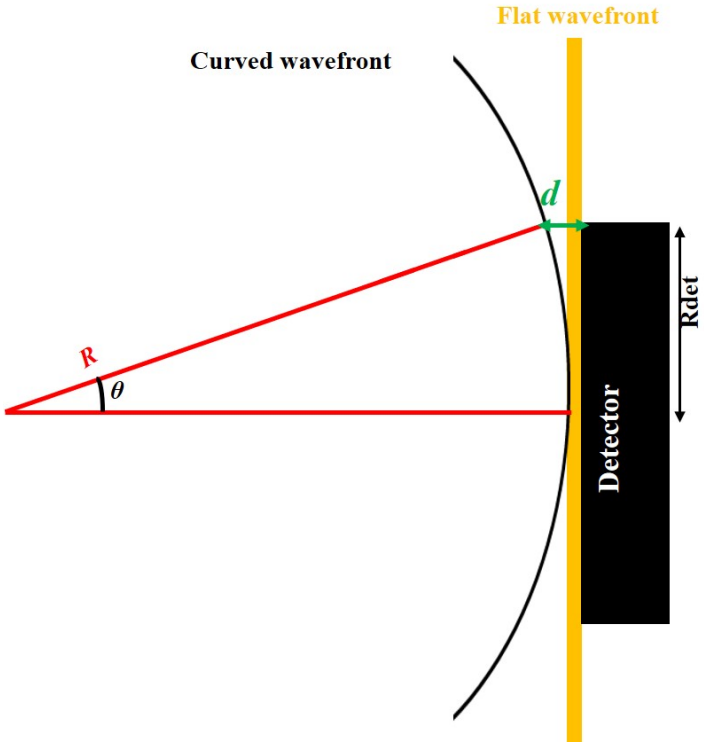

Figure 4.8 Representation of range in path errors d. R is the radius of curvature and R_{det} is the radius of the detector.

Figure 4.9a)&b) shows the fraction of output power as a function of z for w_0 =1 mm and 2 mm respectively. The graphs suggest that if the beam is focused at the right position it will result in maximum throughput. An

interesting observation here is that the graph is doubled-valued. This is because there will be another beam with different R_{in} that can be focused at the same point - one beam is large and does not diverge by a large amount and the other one is small and diverges a lot and at that point they have the same waist. Further analysis involved the comparison between the two models. A simple comparison was made by plotting the range in path errors as a function of detector radius for an aligned system. It was found that the results agree within 3 d.p (see Figure 4.10).

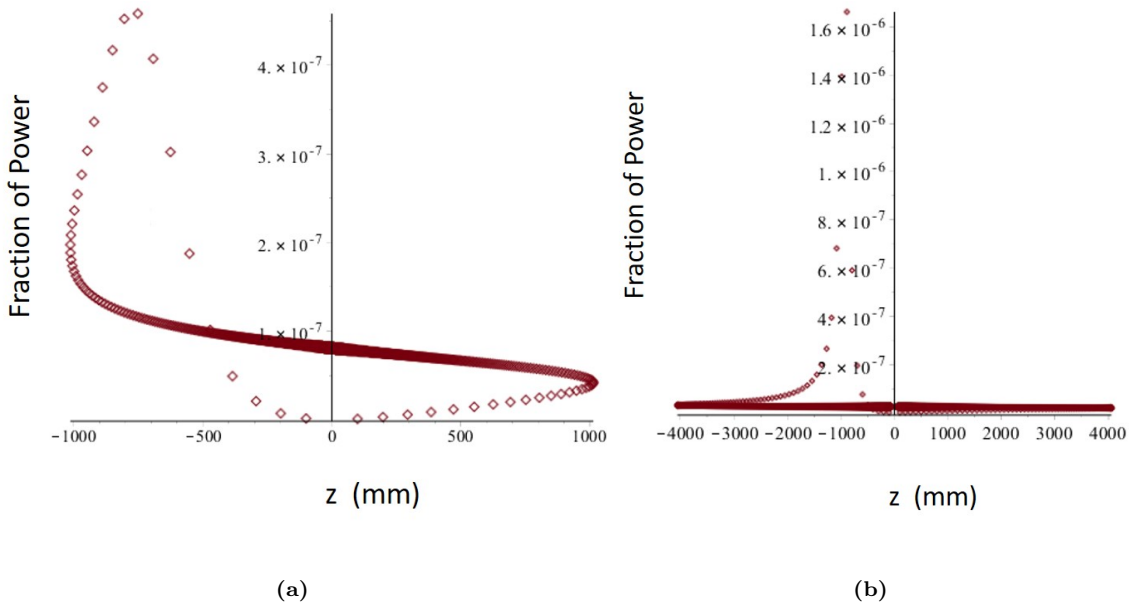

(a) **(b)**

Figure 4.9 Fraction of power for different input beam sizes: (a) w_0=1 mm and (b) w_0=2 mm.

Furthermore three different interferometric designs, with no alignment errors, Ip = 10,50,90 % were simulated for different input beam sizes. The ratio of

their output power (P_1/P_2), where P_1 is the power output of the Gaussian beam model and P_2 the throughput of the ray tracing model, was plotted as a function of z_R/L (L being the distance travelled to reach the polarising beam splitter for the second time). Figure 4.11 suggests that one of the two models breaks for small beam sizes. This will be the ray tracing model as it does not include diffraction (it assumes an infinitely small beam). The disadvantage of the Gaussian beam model is that it can only simulate designs with no misalignment errors.

Therefore it has been shown that the two models, though fundamentally different, agree with each other when the beam size is not too small and thus confirm that the AMS model can be experimentally developed. Furthuremore, it was shown that there is an optimal focusing point for the beam which will result into a maximum throughput.

4.4 Mach Zehnder interferometer

Before building the AMS interferometer, it was important to gain some background on the technical work regarding the alignment of a system and the generation of a quadrature signal. An interference pattern with high visibility can only be obtained if the two beams (coming from the two arms of the interferometer) are exactly on top of each other. A Mach Zehnder

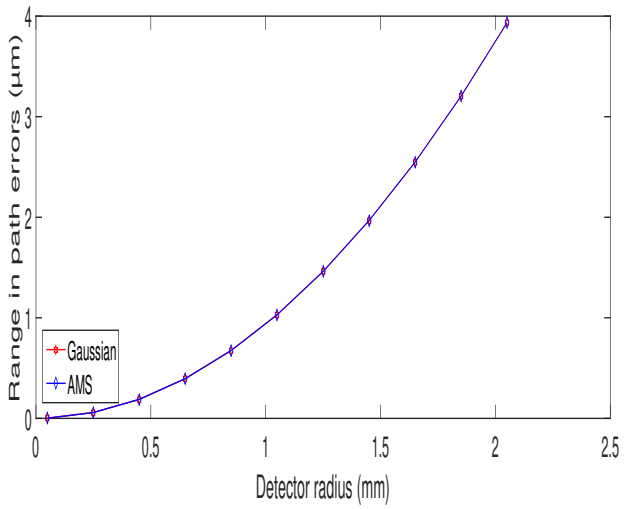

Figure 4.10 Range in path errors vs detector radius for the ray tracing and Gaussian model. The plots appear to overlap meaning that the models agree with each other.

interferometer was built as shown in Figure 4.12. An interesting fact in this experiment was the use of a supercontinuum fibre which generated white light. Therefore, the interference fringes will only appear if the path length difference between the two arms is zero (all wavelengths have an intensity maximum at that point - Figure 4.13[73]). The first step was to align the interferometer while making sure that the two beam paths were almost the same distance. As can be seen in Figure 4.12, two mirrors in the second arm of the interferometer were mounted on a platform whose motion was controlled via a LabVIEW program. In this way, it was possible to move the platform back and forth while controlling the speed of the movement. A time trace was recorded using an oscilloscope where the sampling rate was varied.

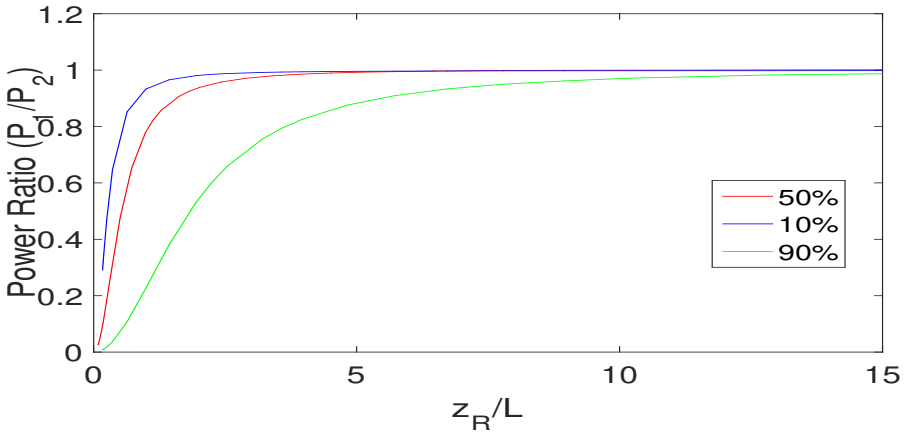

Figure 4.11 Ratio of powers (P_1/P_2) of the two computation models (Gaussian and ray tracing respectively) for three interferometric designs.

For the detection of the white light fringes the detectors were placed after the recombining beam splitter. The quadrature detection will be explained in Section 4.4.2.

4.4.1 White Light Fringes

By carefully determining the difference in the path length, the position of the platform was adjusted in order to record the fringes (see Figure 4.14). The next step was to determine the visibility of the system using Equation 2.2, which was found to be 0.93±0.02 ($I_{\max}$ = 1.69 and $I_{\min}$=0.06).

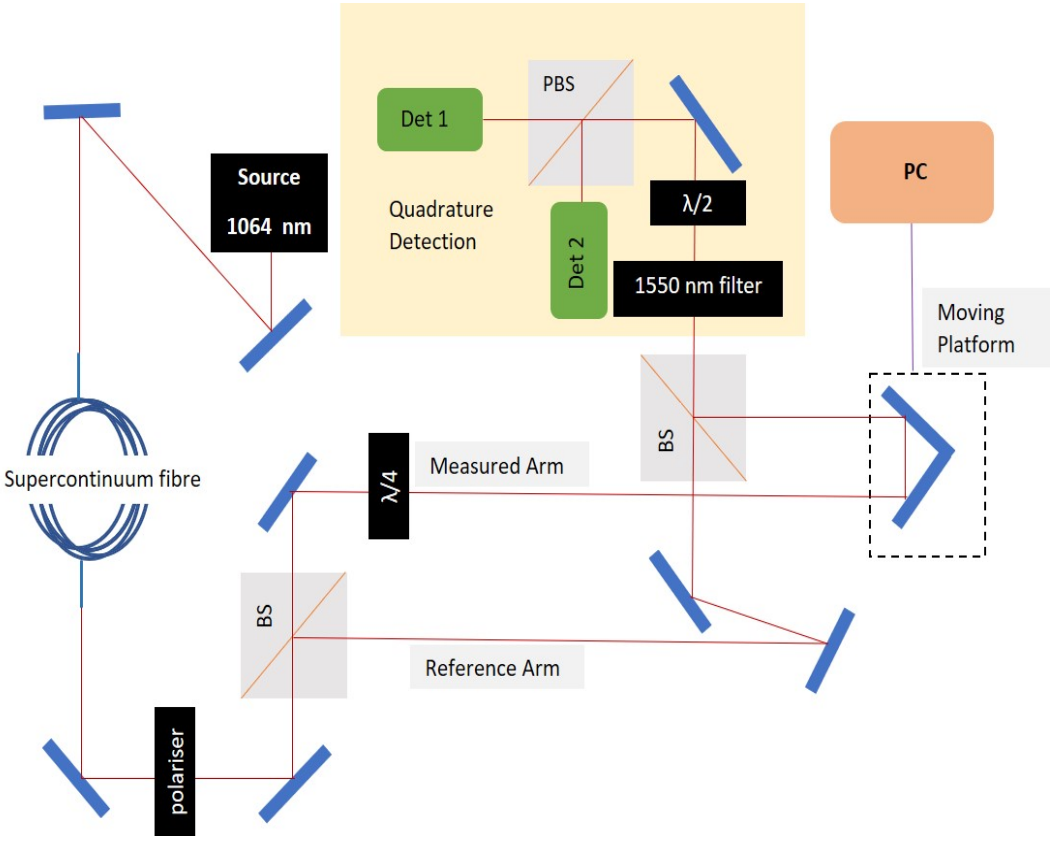

Figure 4.12 Experimental apparatus. The first beam splitter (BS) splits the beam into two, travelling in the reference and measured arm and then they recombine again at the second BS. For the white light fringes the detector (not shown in the figure) is placed after the second BS whereas for the quadrature detection a half waveplate and a polarising beam splitter are placed before the detectors. A quarter waveplate is also placed in the measured arm.

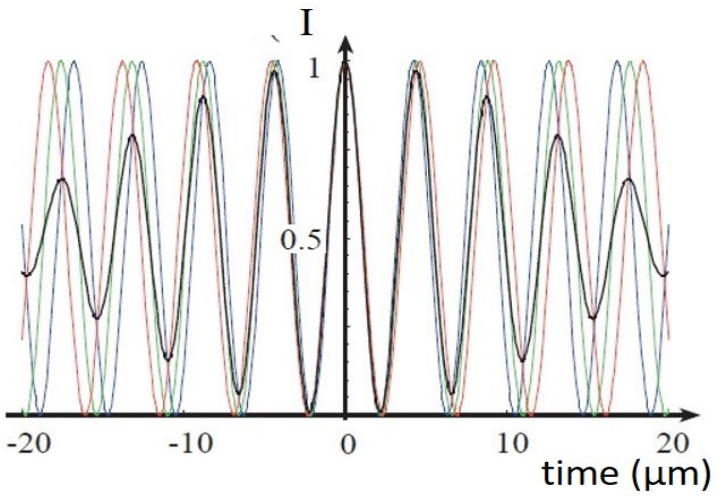

Figure 4.13 Zero optical path length difference gives maximum intensity (black) as all the colours of the spectrum are in phase at that point [73].

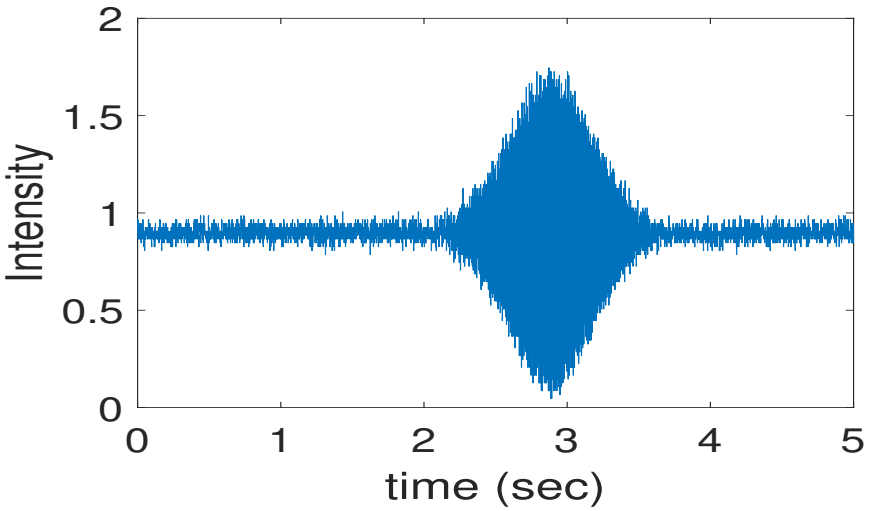

Figure 4.14 White light fringes from the Mach Zehnder interferometer. The signal was recorded using an oscilloscope as the platform shown in figure 4.12 was moving.

4.4.2 Quadrature Analysis

The next step was to implement to the system the quadrature detection. This was achieved by introducing a $\lambda/4$ waveplate in the second arm and a polarising beam splitter (PBS) and a $\lambda/2$ after the recombination of the two beams. A polariser was added in order to induce vertical polarisation to the system. As shown in Figure 4.12, the first non-polarising beam splitter (NPBS) splits the beam into two beams which are in phase with each other. The reflected beam is not subject to any polarisation change, whereas the transmitted beam has to travel through a quarter waveplate. The $\lambda/4$ (set to 45°) rotates the polarisation from linear to circular. The beams will recombine at the second non-polarising beam splitter. The beam will then travel through a half-waveplate (set to 22.5° from vertical) followed by a polarisation element i.e. a polarising beam splitter, which will separate it again in two beams which are in quadrature with each other. This can be justified as follows[74,75]:

A plane wave from the laser is described as:

$$\vec{E} = \hat{x} A_0 \cos(\omega t), \tag{4.3}$$

where $\vec{E}$ is the field vector, A_0 is the amplitude of the plane wave and ω is the frequency of source ($\omega = 2\pi c/\lambda$). The unit vectors $\hat{x}$ and $\hat{y}$ are the unit

vectors in plane and orthogonal to the table. Equation 4.3 can also be written as:

$$\vec{E} = \hat{x}' A' \cos(\omega t) + \hat{y}' A' \cos(\omega t), \tag{4.4}$$

where $A' = A_0/\sqrt{2}$, $\hat{x}'$ and $\hat{y}'$ are the unit vectors in the coordinate frame which is rotated 45° from $\hat{x}$ and $\hat{y}$ (the coordinate frame of the $\lambda/4$ plate).

The reference beam will reach the recombining beam splitter which can be represented as:

$$\vec{E}_{\text{ref}} = \hat{x}' A \cos(\omega t) + \hat{y}' A \cos(\omega t), \tag{4.5}$$

where $A = A'/\sqrt{2}$ is the amplitude of the beam. In the measured path, the beam will travel through a quarter waveplate and therefore becomes:

$$\vec{E}_{\text{mes}} = \hat{x} A \cos(\omega t+\phi)+\hat{y} A \sin(\omega t+\phi) = \hat{x}' A \cos(\omega t+\phi)+\hat{y}' A \sin(\omega t+\phi), \tag{4.6}$$

where ϕ accounts for the optical path difference between the two arms of the interferometer. Though the coordinate system has been rotated by 45°, it wont affect the circular polarisation. The beams will then recombine:

$$\vec{E} = \vec{E}_{\text{ref}}+\vec{E}_{\text{mes}} = \hat{x}' A[\cos(\omega t)+\cos(\omega t+\phi)]+\hat{y}' A[\cos(\omega t)+\sin(\omega t+\phi)]. \tag{4.7}$$

The $\lambda/2$ will rotate the coordinate system back to orthogonal with the table:

$$\vec{E} = \hat{x}A[\cos(\omega t) + \cos(\omega t + \phi)] + \hat{y}A[\cos(\omega t) + \sin(\omega t + \phi)], \tag{4.8}$$

and the polarising beam splitter will split the beam into its x and y components:

$$\vec{E}_{\mathrm{x}} = A[\cos(\omega t) + \cos(\omega t + \phi)] \tag{4.9}$$

$$\vec{E}_{\mathrm{y}} = A[\cos(\omega t) + \sin(\omega t + \phi)] \tag{4.10}$$

The intensities of the two components were found by:

$$|E_{\mathrm{x}}|^2 = A^2[\cos^2(\omega t) + \cos^2(\omega t + \phi) + \cos(2\omega t + \phi) + \cos(\phi)] \tag{4.11}$$

$$|E_{\mathrm{y}}|^2 = A^2[\cos^2(\omega t) + \sin^2(\omega t + \phi) + \sin(2\omega t + \phi) + \sin(\phi)] \tag{4.12}$$

And the time average signal is:

$$I = \langle |E_{\mathrm{x}}|^2 \rangle = A^2(1 + \cos(\phi)) \tag{4.13}$$

$$Q = \langle |E_{\mathrm{y}}|^2 \rangle = A^2(1 + \sin(\phi)) \tag{4.14}$$

The pair of signals is $\pi/2$ out of phase. For this experiment a 1550 nm optical filter was implemented to the system and it was placed after the recombination beam splitter. Figure 4.15 shows that the quadrature signal

was achieved using the above interferometric arrangement. The important property of the quadrature is that you can identify whether the moving arm of the interferometer is moving either right or left. Figure 4.15(a)&(b) show the signal obtained from the two detectors when the platform was moving from point A to point B and from point B to point A, respectively. It can be seen that when the platform was moving forwards (i.e. from A to B - Figure 4.15a) the signal from the first detector is at its maximum when the second signal is moving down the slope, whereas in Figure 4.15b the platform is moving from point B to A and therefore the signal from the second detector is moving up the slope. Figure 4.16 shows the intensity of detector 1 vs intensity of detector 2 (oscilloscope in spatial x-y mode) which forms a circle, as expected. Note that the previous notations (intensity of detector 1Vs2 and x-y spatial mode) are the I and Q, given by equations 4.13 and 4.14.

Building a simple Mach Zehnder interferometer proved to be quite a useful experiment before building the AMS interferometer. Apart from gaining experience on how to align such a system, demonstrating mathematically and experimentally that quadrature detection can be achieved was important as the AMS interferometer is a complex version of a Mach Zehnder interferometer.

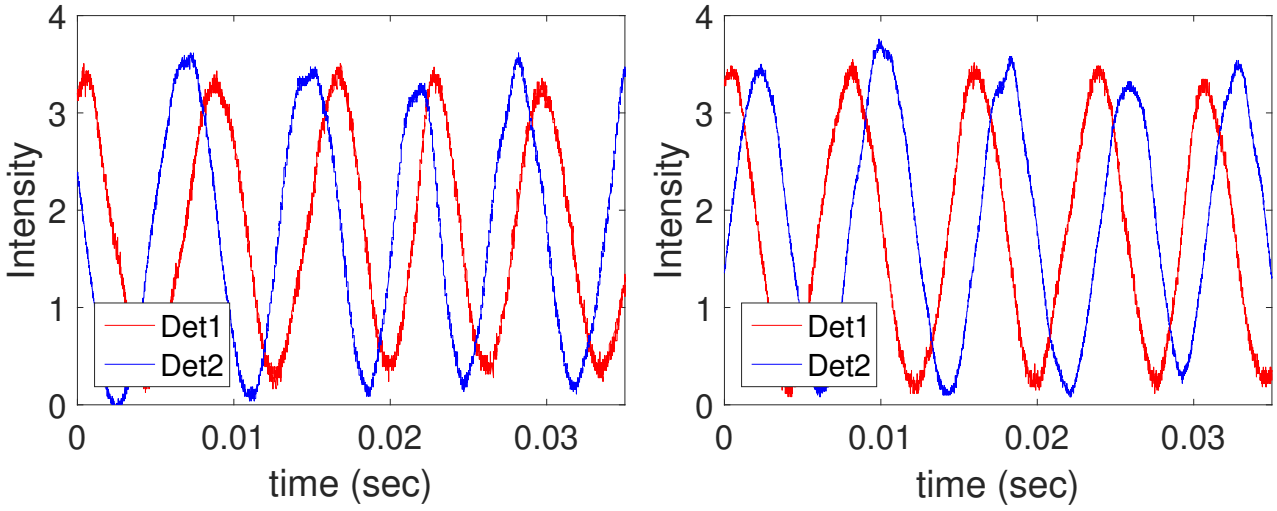

(a) (b)

Figure 4.15 Quadrature detection for the Mach Zehnder interferometer. The platform moves backwards and forward and therefore the relative phase of the signals in (a) and (b) is different. (a) Moving from A to B. (b) Moving from B to A.

4.5 Experimental work on AMS

4.5.1 Initial Arrangement

The interferometer optics and detectors can be miniature, as the interferometer is only required to work along the straight line between two spheres. The AMS design was earlier introduced in Section 4.1. However, the first attempt in building the interferometer involved two plane mirrors instead of spheres (see Figure 4.17). Spheres can cause significant divergence to the beam therefore it was decided to align the system and gather some data with a simplified version.

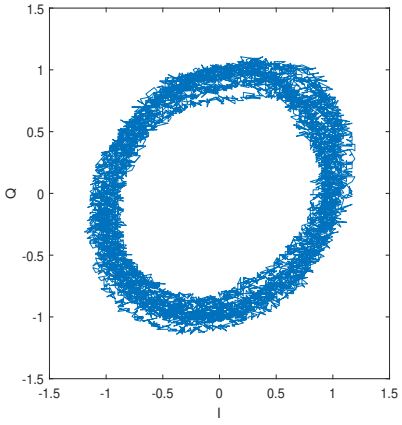

Figure 4.16 X-Y mode of the oscilloscope forms a circle.

Using the AMS configuration four different signals (I,$\bar{I}$,Q,$\bar{Q}$) can be implemented. The source, which operated at 1550 nm, is vertically polarised and a polarisation maintaining (PM) fibre was used to guide the light at the first optical component. The half-waveplate (adjusted to 22.5°) rotates the polarisation from vertical to 45° in order to split the beam into two beams of equal power when it passes through the polarising beam splitter (PBS). Adjusting the half waveplate in a position that will allow more power to reflect off the polarising beam splitter (and therefore travel in the measured arm of the interferometer), was also investigated. This adjustment had a negative impact on the visibility levels of the system. The two beams (reflected and transmitted) were vertically and horizontally polarised respectively. The reflected beam will reach the first sphere but it will first have to pass through a quarter waveplate. The $\lambda/4$ is passed twice before the

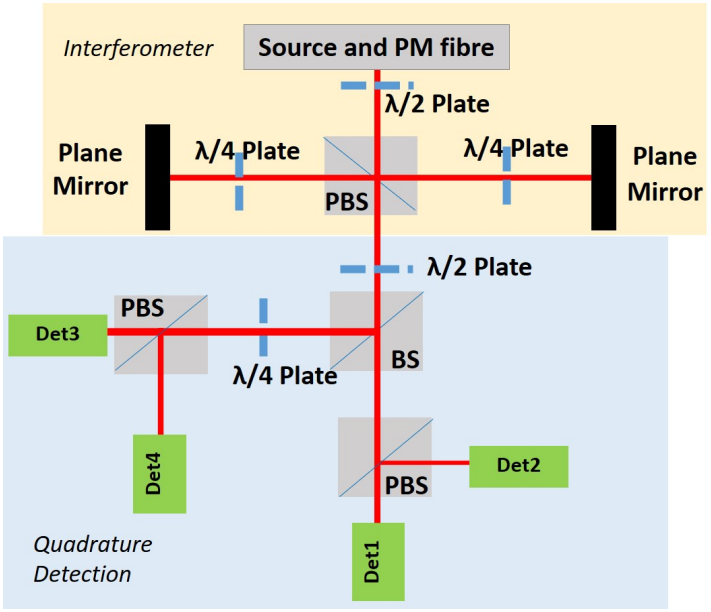

Figure 4.17 Simplified version of the AMS interferometer with the two spheres replaced by plane mirrors. The optical arrangement for the quadrature detection can be seen after the second $\lambda/2$.

beam returns to the polarising beam splitter, which causes a 90° rotation of the polarisation state. In other words, the beam that was reflected from the first polarising beam splitter will get transmitted during the second pass through the polarising beam splitter and therefore it will reach the second sphere. It then travelled back to the first polarising beam splitter where it was reflected as there was another double pass through a quarter waveplate which was placed just before the second sphere.

The beam travelling in the measured arm was then overlapped with the beam of the reference arm. Another half waveplate (adjusted at 22.5°)

rotates the polarisation by 45° for both components, vertical and horizontal, so that they lie at +/- 45° with respect to the vertical. The two beams were then split into two using a non-polarising beam splitter (NPBS) - note that the beams are orthogonally polarised and they have not interfered yet. One beam travelled directly through a polarising beam splitter so a pair of interference patterns was produced that was 180° out of phase (I,$\bar{I}$), whereas the second beam passed through a $\lambda/4$ (90° phase shift of the two polarisation components) and therefore an additional $\lambda/4$ delay to the OPD was produced. This beam also travelled through a polarising beam splitter, which produced a pair of interference patterns that is out of phase (Q,$\bar{Q}$) and at them same time 90° out of phase with I and $\bar{I}$. The four ports were fibre coupled, using standard patch cables, so as to guide the light into the detectors. Thus, four different combinations can be made in order to record a quadrature signal and the equations that support this can be found in Appendix A [76].

4.5.2 The laser

To achieve high accuracy measurements from an interferometric design it is also essential to have a high stability laser. Therefore, a low noise tunable laser from Pure Photonics was bought. It provides a very narrow linewidth of about 10 kHz and a range of operating wavelengths from 1527.605 nm to 1564.496 nm (191.162 THz - 196.250 THz). The output power can vary from

6dBm to 16dBm (4 mW - to 40 mW).

A wavelength calibration was performed by using a gas cell, filled with acetylene (C_2H_2). The cell was purchased from Photonics Technologies with a pressure of 20 Torr, 2° wedged fused silica window, 50 mm optical path length and a diameter of 9 mm. The advantage of using this gas is that its absorption lines are known with subpicometre accuracy and at the same time it is not sensitive to environmental conditions. Acetylene is widely researched as wavelength standard i.e. wavelength calibration reference for the range of 1510 nm - 1540 nm[77]. The experimental apparatus is shown in Figure 4.18a). Figure 4.18b) shows the transmission lines of acetylene C_2H_2 as defined by literature[78,79].

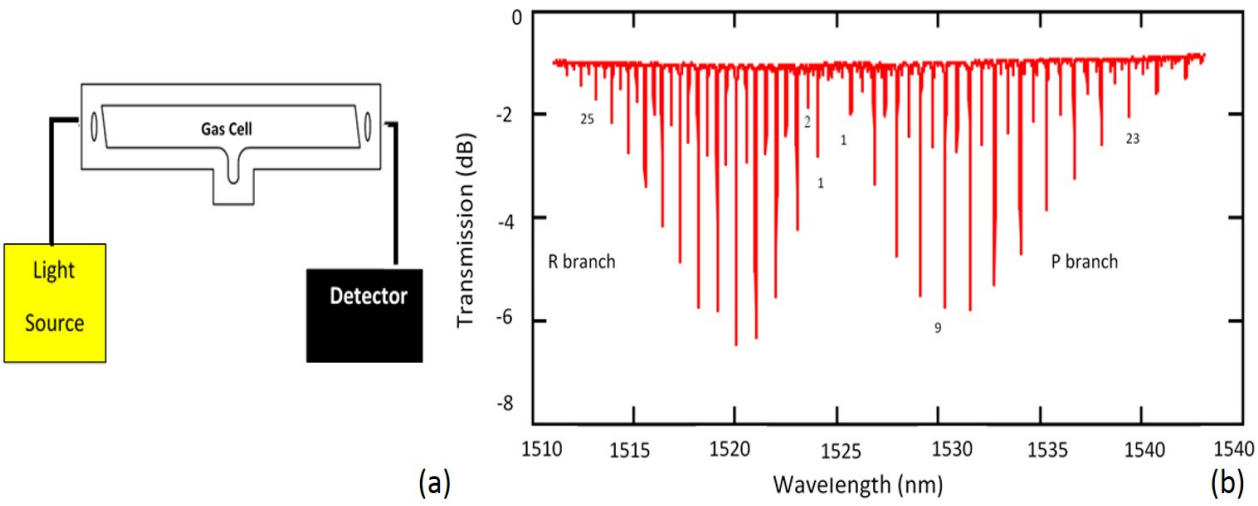

Figure 4.18 a) The experimental setup that was used to identify the absorption lines and (b) the absorption lines of acetylene (C_2H_2) as determined by literature[79].

The aim of this experiment was to identify where the peak nine of the P branch of acetylene appears with the new laser source and compare it with literature (1530.3711±0.0003 nm or 195.89526±0.00004) [79]. The power was recorded for every set frequency of the laser, starting from 195.8932 THz to 195.8983 THz with a stepsize of 0.1 GHz. The peak (Figure 4.19 blue) was found to be at 195.8953 THz which agrees with the literature within 0.1 GHz. The absorption linewidth of the peak was determined by fitting a Gaussian function (Figure 4.19 red). This function gives the shape of spectral lines, when the spectrum broadening is caused by movement of gas atoms (Doppler broadening) in acetylene. The FWHM was found to be 730±40 MHz whereas Wang *et al* defined it as 760 MHz [80]. They stated that their results were valid as the FWHM corresponds to the expected pressure (∼9 MHz/mbar) and Doppler broadening [81]. Thus, the Pure Photonics laser was considered stable enough for the initial tests with well-defined wavelengths.

4.5.3 System's Performance

Once the system, shown in figure Figure 4.17, was completed, a few changes were required in order to optimise its performance. By carefully aligning the system so that the beam passes through the centre of the optical components, the throughput was increased from 50% to almost 80%. The throughput in this case is the power at each detector over the power after the polarisation maintaining (PM) fibre of figure 4.17.

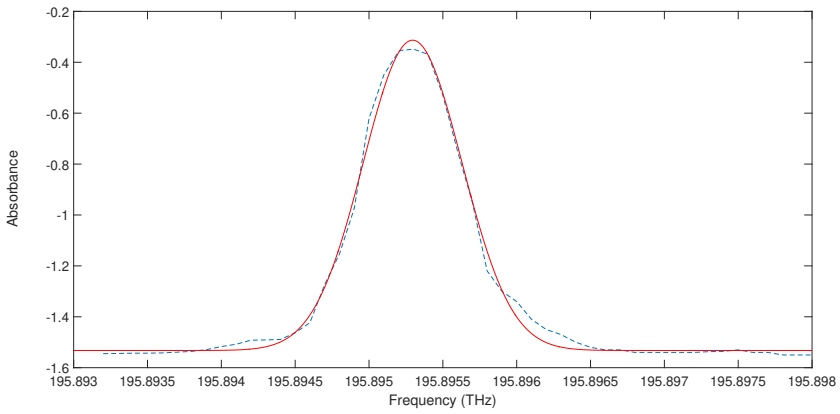

Figure 4.19 Peak 9 of the acetylene absorption spectrum. Blue dash: Experimental data Red solid: Gaussian fit.

An oscilloscope (in spatial x-y mode) was used to initially monitor the stability of the system. It was expected that any major change in the fringe pattern will only occur due to variations in the optical path difference. However, it was found that the fringes were moving constantly in random directions along the circle. To investigate this, data were recorded over long periods of time during the day and night (where a temperature change was a expected). The fringes were also recorded while a constant vibration was induced to the system. The results suggested that neither of the two factors was the major source of this random change in the interferometric pattern. After careful consideration of all the factors that can possibly cause this issue, it was found that "small" interferometers were formed between the optical components of the system. This is a common problem in the field of

interferometry, though in this case it is a major issue as the optical bench which is suitable for miniature optics was designed so that the components can only be placed in a straight line. In other words, if the first polarising beam splitter (PBS) was rotated by a large angle e.g 30° (see Figure 4.20), there will be no place on the micro-bench to place the rest of the optics so that the beam will pass through their centre. Therefore, the first polarising beam splitter was rotated by a small angle (8°) so that the transmitted beam can still travel through the centre of the optics. However, the two quarter waveplates which seem to cause most of the problem, were removed from the main micro-bench and placed on individual micro-benches away from the polarising beam splitter. This solution did not change the order of the arrangement of the optical components.

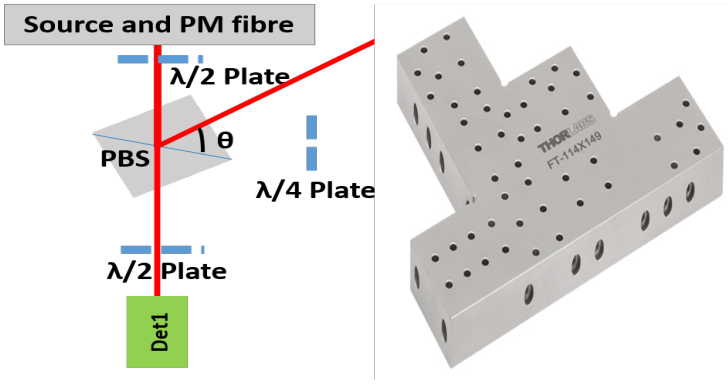

Figure 4.20 Left: Simplified version of the AMS interferometer. To prevent the formation of small interferometers between the optical components, the polarising beam splitter (PBS) must be placed in angle. This is a problem for the miniature optics as the micro bench (right) will not allow the components to be placed in an angle [82].

To further test the stability of the interferometer, the acetylene cell (used in Chapter 4.5.2) was used simultaneously with the interferometer. In order to implement the acetylene cell in the system a set of new optical components (polarisation maintaining fibres and optical isolators) were also introduced to the system. It was found that this set of new optical components had affected the coupling efficiency as the powers at the four collection ends of the interferometer (see Figure 4.17) were randomly varying by more than 30 to 40% at times. This effect was not another parasitic interferometer somewhere in the system as the laser was set to scan and there was only one clear interferometric signal on the oscilloscope. Power fluctuations were also recorded just after the input stage of the interferometer. The last two observations led to the conclusion that the polarisation at the input of the interferometer may not have been vertical (and continuously varying) even though all the optical components in the system were polarisation maintaining.

To minimise the effect, a polariser was placed at the beginning of the interferometer allowing only the vertical polarisation to go through the system. In Chapter 4.5.1 it has been shown that the polarisation at the input of the interferometric set-up had to be vertical in order to produce a quadrature detection system. Furthuremore, the optical fibres involved were

taped on the bench using Kapton tape in order to prevent any further movement that can cause changes in the polarisation. Figure 4.21a) shows an example of how sensitive the polarisation maintaining fibres were just by gently touching them. The two interferometric signals ($I\&Q$ - blue and red), were very sensitive to small changes in the position of the fibres. However, repeating the experiment after the polariser was introduced into the system showed that the fluctuations had vanished (Figure 4.21b). A system without the polariser will cause the ratio of the interferometric signals to vary and this has a negative effect on the quality of the interferometer.

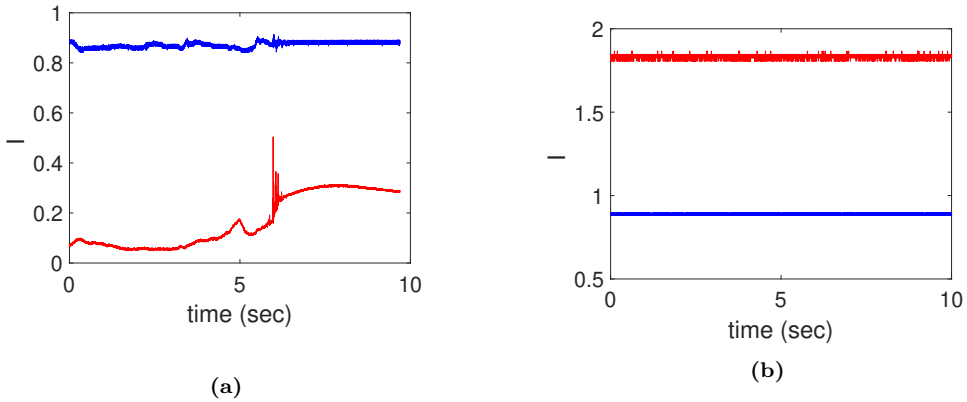

Figure 4.21 Interferometric signals (I&Q - blue and red) recorded when: (a) moving the fibres with no polariser and (b) moving the fibres with a polariser in the system. The signals are affected by a small change in position of the polarisation maintaining fibre when a polariser is not part of the experimental setup.

The focus was then set on the procedure that calculates the phase of the signal and then unwrap the phase using a quadrature signal. If all the

problems have been resolved then any variations of the interferometric signal are real and need to be analysed. To calculate the phase of the signal, the four quadrant arctangent function was used which can be calculated using the following equation:

$$a\tan2(I,Q) = \begin{cases} \tan^{-1}[\frac{I}{Q}], & \text{I>0 and Q>0 } 1^{\text{st}} \text{ quadrant} \\ \tan^{-1}[\frac{I}{Q}] + \pi, & \text{I>0 and Q<0 } 2^{\text{nd}} \text{ quadrant} \\ \tan^{-1}[\frac{I}{Q}] - \pi, & \text{I<0 and Q<0 } 3^{\text{rd}} \text{ quadrant} \\ \tan^{-1}[\frac{I}{Q}], & \text{I<0 and Q>0 } 4^{\text{th}} \text{ quadrant} \end{cases}, \qquad (4.15)$$

where I and Q are real numbers and in this case they represent the amplitude of the two normalised interferometric traces in quadrature[83]. A circle was fitted to the data using the least square fitting function in MATLAB and it was then shifted so that point (0,0) was the centre of the circle. Many traces have been recorded where a vibration or a change in the optical path, or a fine tuning of the laser frequency (of the order of a few MHz), can change the fringe pattern. Figure 4.22 (left) shows IVsQ when a change in optical path was induced to the system. Figure 4.22 (top right) shows the phase of the signal. The graph of IVsQ suggests that the pattern has not moved by an entire fringe (less than 2π phase change), as the plot has not formed a complete circle. It has however moved to the next (or

previous) fringe e.g movement from fringe N to fringe $N + 1$ with less than 2π phase change, as the system has been modelled so that the change to the next fringe is the point between the second and third quadrant of the full circle that can be formed in figure 4.22 (discontinuity point). As the pattern had moved to the next fringe, the wrapped phase graph failed to provide the correct results. In this case, the amplitude of the phase change will exceed the $\pm\pi$ range and therefore it will be wrapped in order to stay in that range. This means that the unwrapped phase graph will contain at least one π jump and as shown in figure 4.22 (top right) the interferometric pattern has moved to the next fringe e.g fringe *N+1* and back to fringe *N*, multiple times.

A procedure is therefore needed that will unwrap the phase. This was achieved by calculating the difference between two consecutive samples. If the difference is larger than π, then 2π should be subtracted from that sample (and all the following samples). If the difference is smaller than -π then 2π should be added to the sample[83]. Figure 4.22 (bottom right) shows the unwrapped phase which does not exceed the $\pm 2\pi$ range, as expected. A fine tuning of the laser frequency (of the order of a few hundred MHz) was then applied to the system and the data were analysed in order to unwrap the phase. As shown in Figure 4.23, the unwrapped phase will exceed the $\pm 2\pi$ range which agrees with the IVsQ graph. Therefore it has been shown

that the code works and it will be further developed and discussed in Chapter 5.

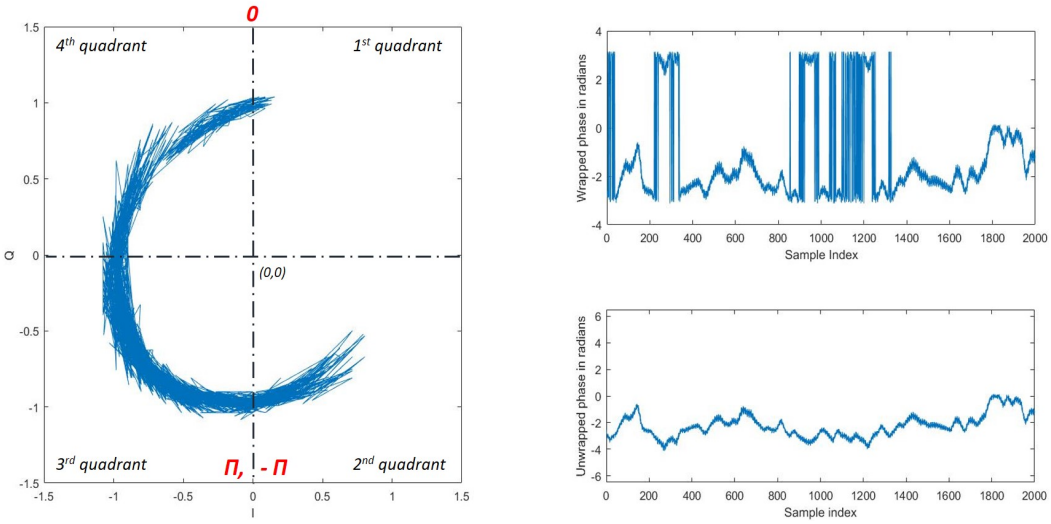

Figure 4.22 Left: IVsQ for an induced change in the optical path. Top Right: The phase of the IQ signal. Bottom Right: The unwrapped phase.

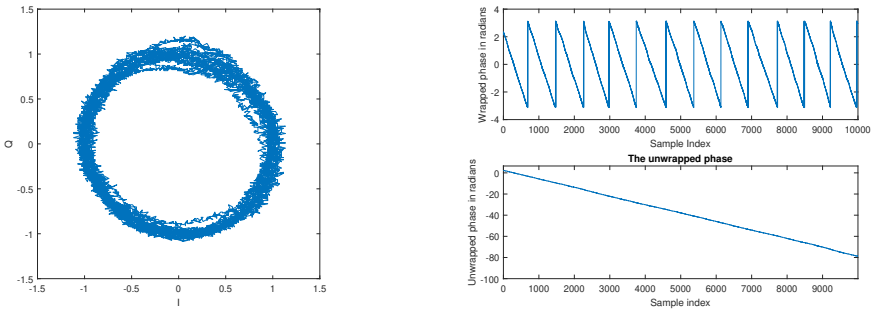

Figure 4.23 Left: IVsQ for an induced change of the laser frequency. Top Right: The phase of the IQ signal. Bottom Right: The unwrapped phase.

4.5.4 Spheres with n=2

The final part of this experiment was to replace the two mirrors with spheres in order to fully build the AMS interferometer shown in figure 4.1a. Instead of replacing them with polished steel spheres, the mirrors were replaced with spheres that have a refractive index of 2 (S-LAH79 OHARA with 8.5 mm radius). This is essentially a retroreflector. Even though a polished steel sphere can reflect more light off its surface than a n=2 sphere, its highly divergent nature will cause a very significant power loss. The beam reflected off of the n=2 sphere will be collimated. Figure 4.24 shows the reflection of an individual ray from a) spherical retro-reflector, b) n=2 sphere and c) polished steel sphere. The retro-reflector requires two highly reflective mirrors to be placed perpendicular to each other (two for reflection in a plane and 3 for reflection in 3D). The ray leaving the retro-reflector is parallel to the incoming ray and the reflection is $\sim$ 100%. The direction of the ray leaving the n=2 sphere is similar to the retro-reflector. The main difference is that most of the light will be transmitted through the back of the sphere and only $\sim$ 9% will be reflected. The polished steel sphere reflects $\sim$ 100% of the incoming ray but only a very small fraction of power reaches the detector due to the large angle of reflection. This was shown to be true in Chapter 4.2.1 where only a very small fraction of power (10^{-9}) reaches the detector.

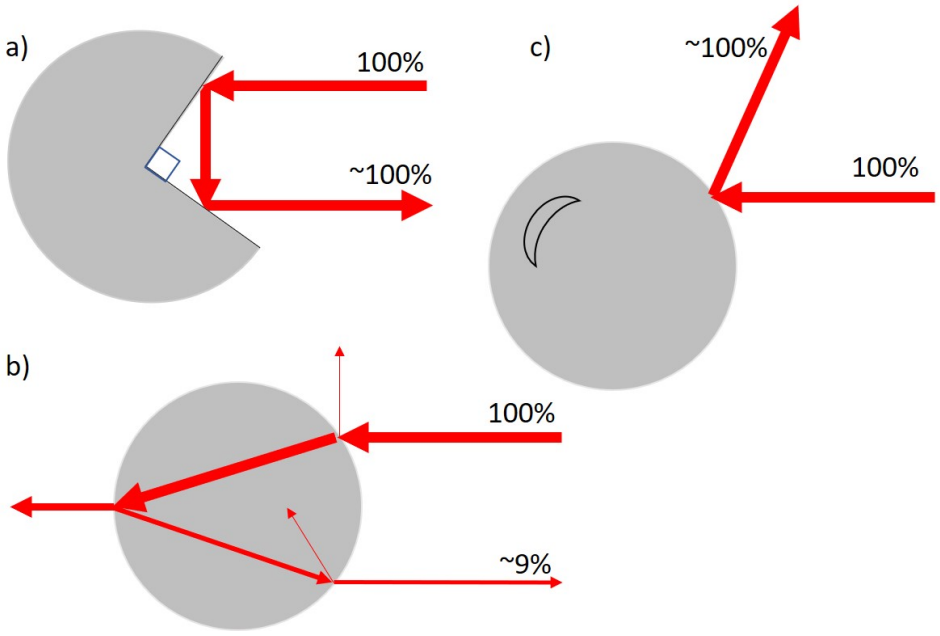

Figure 4.24 Reflections of a ray from: a) Spherical retro-reflector b) n=2 sphere c) polished steel sphere.

Each sphere was glued on top of a 3D printed plastic alignment stage (designed and made by Dr. Richard Bowman - member of the CPPM group). The stages were designed so that they can move in x&y-axis by 1mm and they have a hole at the back that was used to align the beam (see figure 4.25). The 3D stages were placed on top of a micrometer for movement in the z-axis. Plastic has a lower thermal expansion compared to metal meaning that the stages are less susceptible to temperature fluctuations (compared to a metallic stage). However, plastic sags more when weight is placed on top of it and this can be a limiting factor for the stability of the experiment.

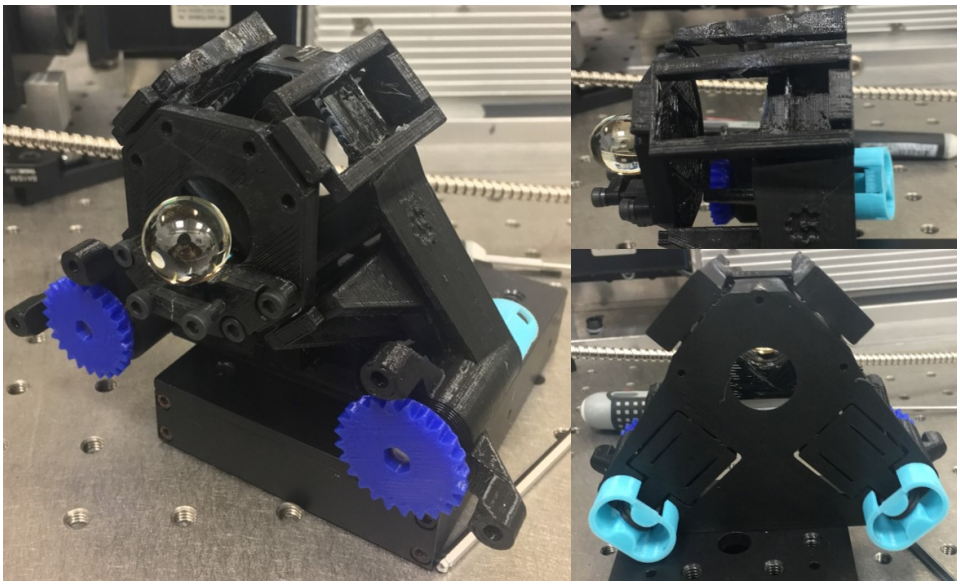

Figure 4.25 Images taken of the n=2 sphere on a 3D printed plastic stage.

Nonetheless, the flat mirrors were replaced by the n=2 spheres and the results of the phase measurement graphs are shown in figure 4.26. Even though the figure itself does not show any interesting features, the ability to create this graph suggests that there are no concerns regarding shot noise when the n=2 spheres are used. The ray tracing model (see Section 4.2.1) presented a system with two polished steel spheres where the total throughput is of the order of 10^{-9}. This very low throughput would have made the initial alignment of the interferometer (without any feedback signal) very difficult. However, with the n=2 it was possible to align the system and generate the IVsQ and fringe counting graphs.

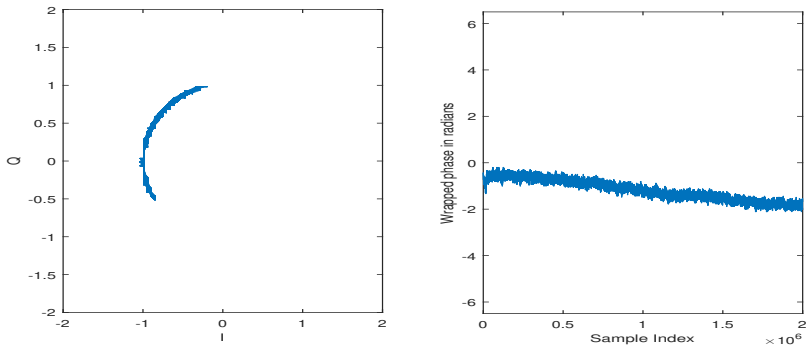

Figure 4.26 Left: IVsQ for an induced change of the laser frequency. Right: The phase of the $IVsQ$ signal for the interferometer with the n=2 spheres instead of the flat mirrors. As the interferometric pattern did not move to the next or previous fringe there is no need to unwrap the phase.

This was a very important result showing that a single scale bar and potentially a network system can be built with a high throughput. Furthuremore, the mechanical properties of the 3D printed stages must be investigated to determine whether or not they affect the alignment of the system over long time scales. The n=2 spheres were used in this experiment to aid alignment but since the results show that they can provide a stable signal over a long period of time it is worth investigating the possibility of replacing the polished steel spheres in the original design. Though their implementation was simple whilst aligning the interferometer, it is necessary to determine their uncertainty budget (similar to Table 1 in Muelaner *et al*[70]) before considering replacing the polished steel spheres with the n=2 spheres. Implementing them in the two AMS computational models (ray tracing and Gaussian beam) was not necessary as it has already been proven

with figure 4.26 that they can provide a clear signal when placed in the AMS interferometer. The polished steel spheres were originally chosen as they are mechanically strong, durable and cost effective in comparison to the n=2 spheres.

4.6 Future Work

Unfortunately the work on the AMS interferometer was never finalised. The remaining tasks involve the conversion of the current set-up to a portable self-aligned scale bar that can also be a part of a network of scale bars around an object to be measured. The AMS interferometer will be re-visited in Chapter 5 (and 7) as the interferometric signals can assist in improving the quality of the laser frequency locking system.

This system will help minimise potential fluctuations from the laser source that affect the interferometric signals. Eliminating these effects brings the interferometer one step closer to its original task i.e. provide high accuracy length measurements without being affected by external parameters.

Chapter 5

Laser-frequency stabilization

5.1 Motivation

In Chapter 1 it was mentioned that the AMS interferometer will use an absolute distance measurement. However, in Chapter 4.5.3, the *IQ* signals were not tested during frequency scans but only with a fixed frequency laser. Though the phase measurement graphs are not an absolute distance measurement, they can indicate whether or not the interferometer is stable and if any background noise is significant enough to affect the interferometric signals. Furthuremore, if the interferometer can work with a fixed wavelength laser it would be easy to implement a scanning laser instead and therefore perform the FSI measurements. A fixed wavelength laser is also a more cost effective solution compared to an FSI system. The laser and the electronics of such systems tend to be expensive as the data acquisition is required to

analyse millions of data points in real-time for each scan. The main advantage of using the FSI system over a phase measurement graph and fringe counting is the fact that the FSI is an absolute distance measurement (ADM). However, a technique called synthetic wavelength can be used, which is an ADM within some range and can work alongside the phase measurement graph as it requires fixed wavelength lasers (at least 2) [84].

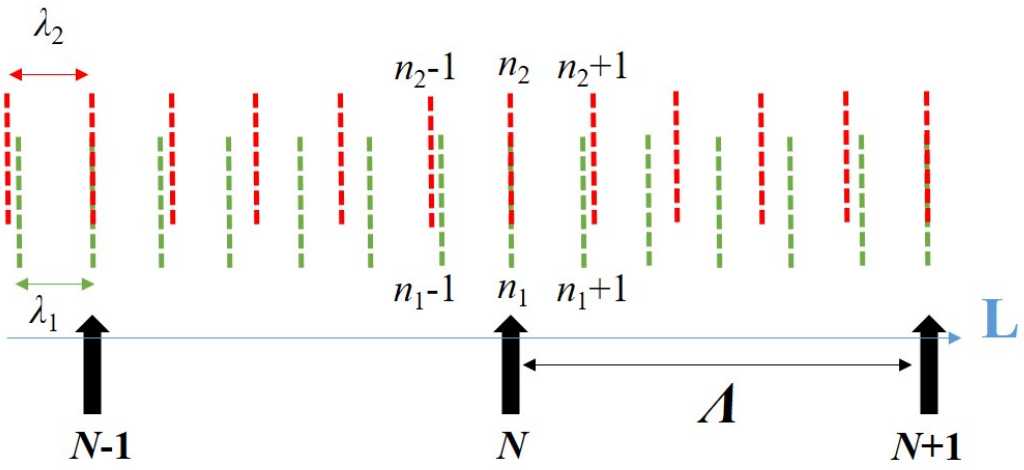

Figure 5.1 Two different wavelengths λ_1 and λ_2 overlap at 3 possible L values (3 black arrows) within this range, after measuring ϕ_1 and ϕ_2.

For an interferometer the optical path length difference, L, is given by:

$$L = \lambda_1(n_1 + \frac{\phi_1}{2\pi}), \tag{5.1}$$

for λ_1 where ϕ_1 is the measured phase. The green lines on figure 5.1 show L for different n_1, given that ϕ_1 is measured.

For λ_2, the optical path length difference is given by:

$$L = \lambda_2(n_2 + \frac{\phi_2}{2\pi}). \tag{5.2}$$

The red lines on figure 5.1 show L for different n_2, given that ϕ_2 is measured. Therefore the real length L must satisfy equations 5.1&5.2 simultaneously, which has three possible values in figure 5.1 (as shown with the three black arrows N-1, N and N+1).

De Groot *et al* has done some more in-depth analysis which shows that the spacing between the possible values of L (N-1, N and N+1 of figure 5.1), is given by:

$$\Lambda = \frac{\lambda_1\lambda_2}{\lambda_1 - \lambda_2}. \tag{5.3}$$

With the use of the synthetic wavelength technique it is possible to increase the range of unambiguity of an interferometric measurement, as shown in figure 5.1 and provide a good absolute accuracy based on literature[85–87]. For years, the measurement range of this technique was limited however, it was found that the unambiguous range can be extended by utilising the phase measurements for each operating wavelength[88]. Provided that N (see figure 5.1) has been determined correctly the absolute accuracy of the system

can be determined within a fraction of the wavelength[85].

The following set of experiments can determine whether or not any parasitic interferometers and other effects have been eliminated. Determining frequency stability Δf, can determine (with the use of numerical simulations) whether or not the system can support a cost-effective absolute distance measurement.

5.2 Experimental Setup and its Basic Principles

In some applications, such as ours, the frequency stability of the laser plays an essential role in the quality of the measurement. Building a measurement system with no back-reflections and minimizing temperature variations is not enough to provide an accurate reading for a distance measurement. It is therefore important to suppress any laser noise and stabilize some laser parameters. Other applications that require laser stabilization are experiments that involve laser cooling, trapping of atoms and spectroscopy applications. Usually a diode laser is used. This is because they are cost effective, compact and they are available in all sorts of wavelengths and can be tuned over a few hundreds of megahertz. Though they emit a very narrow line of frequencies, fluctuations of temperature and current can cause small frequency variations.

It is possible to narrow the range of frequency fluctuations with various techniques that have been developed over the years. These techniques can be divided into passive and active. Active stabilization requires some sort of electronic feedback which then "acts" on the laser and corrects for any frequency deviations. It involves the conversion of the fluctuation of some laser parameters to an electronic signal [89]. On the other hand, no electronics are required for a passive laser stabilisation technique. It relies only on purely optical effects such as the Kerr effect [90].

For this task, an active technique was used which involved the use of a lock-in amplifier (SR850 DSP Lock-In Amplifier). The aim was to create a control signal i.e. an error signal that can be used to stabilize the laser frequency. A small frequency modulation, ω_1, was imposed on the laser frequency by using a frequency generator (sine wave with frequency of 70 kHz and amplitude of 100 mV peak-to-peak).

In Chapter 4.5.2 an acetylene gas cell was used in order to determine the stability of a non-stabilised tunable diode laser. It was shown that the laser frequency was tuned in very small increments in order to determine the peak position of a specific absorption line. It is expected that the absorption signal

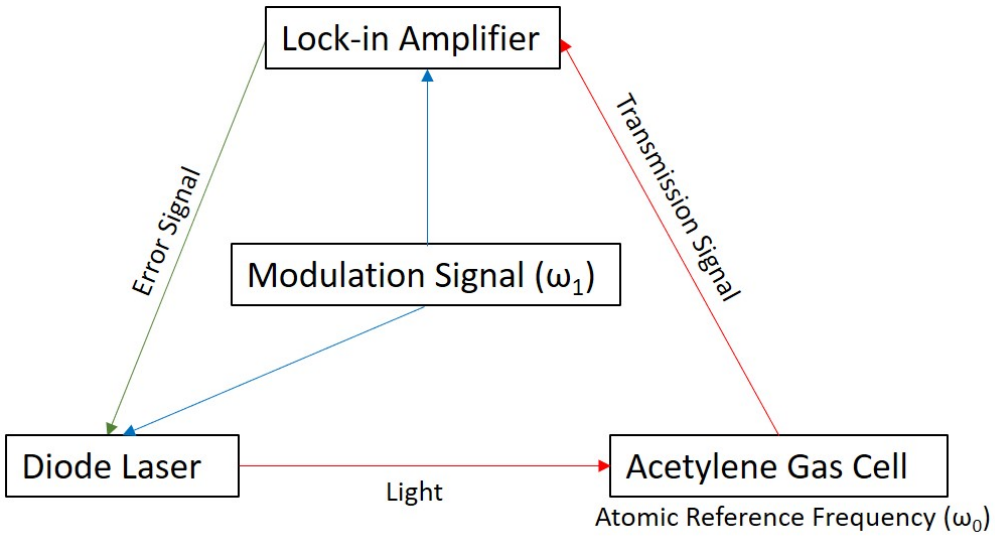

Figure 5.2 Simplified schematic of the components involved in the measurement. A frequency modulation is applied on the tunable diode laser around the frequency ω_0, which generates the transmission signal and subsequently the error signal [91].

will follow the curve as the frequency is tuned. This method is good enough for the purpose of determining the accuracy of a free-running laser. When long term stability is required this technique cannot be used to determine the frequency of the laser as the amplitude of the curve is exactly the same on both sides of the line centre. Therefore, sign becomes an issue and an error signal that can identify the difference is required.

In general locking a laser to an absorption line without providing an uncertainty is considered an easy task. Using a gas reference cell with absorption atomic lines along the range of interest, in this case an acetylene cell with absorption peaks between 1510 nm and 1540 nm, is the best method

to confirm that the laser is stabilised at a well-defined frequency. The challenge is to be able to lock the laser to the desired frequency with the smallest possible uncertainty. The laser frequency was manually tuned in small increments (similar to the technique used in Chapter 4.5.2) until the detection signal from the transmission signal was giving the minimum value -this is the closer it could get to the line centre before crossing to the other side of the peak. For consistency purposes the laser frequency was always tuned from high to low i.e. starting from the left side of the absorption peak and moving toward the centre. Using the acetylene gas cell, with transition frequency of ω_0, a transmission signal is then obtained which is then sent to the input channel of the lock-in amplifier. The output of the lock-in amplifier (the error signal) measures the amplitude of the modulated signal (that is proportional to the gradient of the peak i.e. how steep the absorption is) and is essentially the derivative of the transmission signal. The error signal is fed back to the tunable laser as shown in figure 5.2.

Figure 5.3 shows the absorption peak with central frequency ω_0. The amplitude of the modulated signal changes as the laser frequency varies. When the laser frequency matches ω_0 (i.e they are in resonance), the amplitude of the modulated signal is 0. Thus the absorption signal shown in figure 5.3 can be used by the lock-in amplifier in order to produce the error

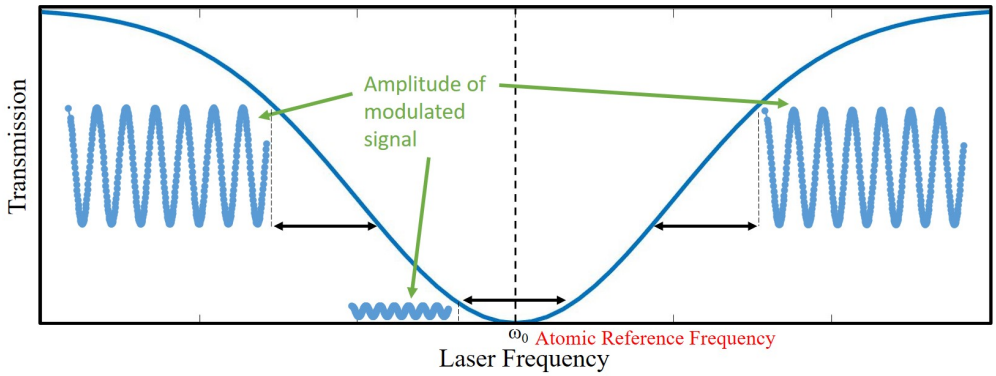

Figure 5.3 Transmission of an atomic reference frequency. The amplitude of the modulation frequency ω_1 changes as the laser frequency varies. Away from the absorption peak the modulation is ω_1 and when the laser frequency matches the reference frequency the signal becomes 0.

signal (derivative of absorption signal), shown in figure 5.4. Therefore, when the laser frequency drifts away from ω_0, the lock-in amplifier can force it to return back to the optimal position using an error signal that is proportional to the amount of the drift. A positive error signal corresponds to a drift at a lower frequency than ω_0 and vice versa, a negative error signal corresponds to a drift at a frequency higher than ω_0. An error signal is not required when the laser frequency matches ω_0. Thus the error signal of the lock-in amplifier is able to recover the stability of the laser frequency and respond to any sudden drifts, at all times. It is also worth noting that this procedure will fail in case the drift exceeds the maximum and minimum peaks of the error signal shown in figure 5.4[91].

Figure 5.5 shows the complete experimental set-up that was developed for

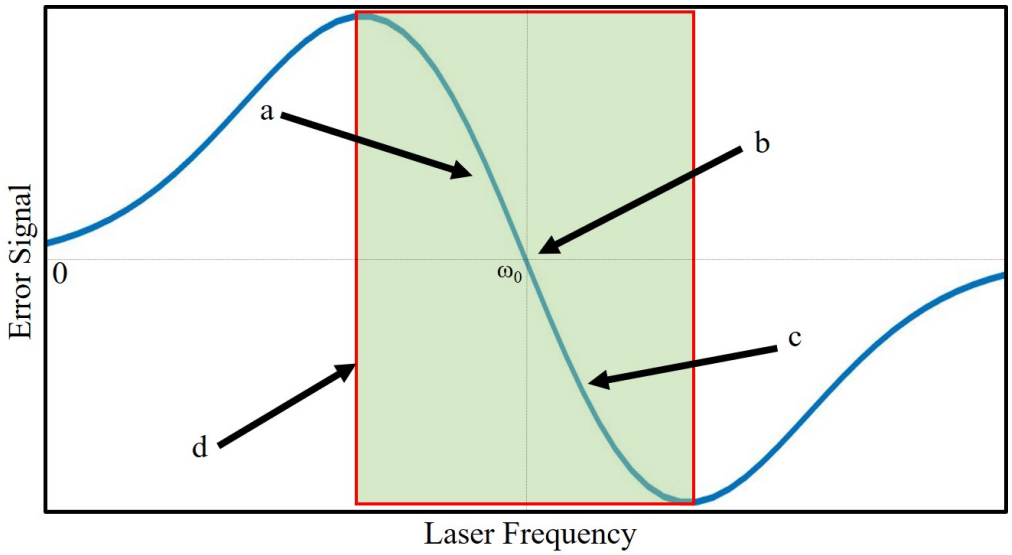

Figure 5.4 Error signal using the lock-in amplifier for the absorption peak show in figure 5.3. The laser frequency is: a) lower than ω_0, b) equal to ω_0 (on resonance) and c) higher than ω_0. d) shows the limits of this procedure.

attempting to lock the Pure Photonics PPCL300 low-noise tunable laser. As shown, the beam that travels through the acetylene cell is collected by the detector and it is then fed into the lock-in amplifier.

The same modulation signal is sent to the lock-in amplifier and works as the reference signal which takes the form of[92]:

$$V_{ref}\sin(\omega_{ref}t + \theta_{ref}), \tag{5.4}$$

where V_{ref} is the amplitude of the reference signal, ω_{ref} and θ_{ref} are the frequency and phase of the reference signal respectively. In the same way, the

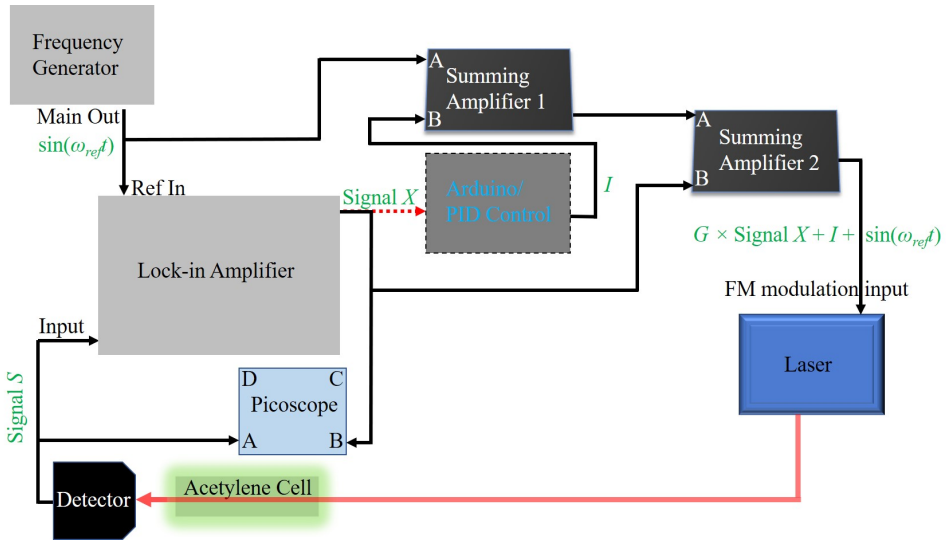

Figure 5.5 Complete experimental set-up for laser frequency stabilization. A signal from the laser is sent through the acetylene cell that then reaches the detector and then sent to the lock-in amplifier (Signal S). At the same time the frequency generator provides a reference signal through the "Ref in" port of the lock-in amplifier. The error signal, "Signal X", is sent to the second summing amplifier and PID controller. The two summing amplifiers combine the signals from the PID controller, "Signal X" and the modulation from the frequency generator and they are sent back to the laser through the FM modulation port. A second output from the lock-in amplifier (not shown in the figure for simplicity) was used to monitor various parameters of the system through an oscilloscope. The signal through the acetylene cell along with the error signal "Signal X", were recorded for long time scales using the Picoscope.

signal sent to the lock-in amplifier via the detector (Signal S on figure 5.5) takes the form of:

$$V_{sig}\sin(\omega_r t + \theta_{sig}), \tag{5.5}$$

where V_{sig} is the amplitude of the signal, ω_r is the frequency of the signal and θ_{sig} is the phase of the signal. The lock-in amplifier takes the input signal, amplifies it and multiplies it by the reference signal. The output signal (V_{out})

takes the form of:

$$V_{out} = V_{ref}V_{sig}\sin(\omega_r t + \theta_{sig})\sin(\omega_{ref} t + \theta_{ref}). \tag{5.6}$$

Equation 5.6 can we written as:

$$V_{out} = \frac{1}{2}V_{ref}V_{sig}\cos([\omega_r - \omega_{ref}]t + \theta_{sig} - \theta_{ref}) - \frac{1}{2}V_{ref}V_{sig}\cos([\omega_r + \omega_{ref}]t + \theta_{sig} + \theta_{ref}). \tag{5.7}$$

Thus, when $\omega_{\mathrm{ref}} = \omega_{\mathrm{r}}$, and provided that you average for long enough, equation 5.7 becomes:

$$< V_{out} >= \frac{1}{2}V_{ref}V_{sig}\cos(\theta), \tag{5.8}$$

where θ is the phase difference between the signal and reference. The half factor and V_{ref} can be adjusted to give 1. This is the "Signal X" output from the lock-in amplifier that is sent to the second summing amplifier and the Arduino, for the PID controller, through a serial connection (RS232 - TTL). All the other connections were analogue. The lock-in amplifier has second output (not shown in figure 5.5 for simplicity) that was used to monitor various parameters of the system such as X, Y, R and θ through a DSO-X 3032A digital oscilloscope.

Two summing amplifiers were used to combine the error signal from the lock-in amplifier along with the corrections of the PID control and as mentioned earlier, the modulation from the frequency generator. The second summing amplifier has a switchable gain (G - initially set to zero) that can amplify the signal from the lock-in amplifier i.e. the error signal "Signal X" and when activated the locking procedure is enabled. Before amplifying the "X" signal, the laser frequency was manually tuned until the lock-in amplifier reads the smallest possible "Signal X" value, that is close to zero. This was done in order to minimize the required work of the feedback loop. The PID input can then be enabled.

5.2.1 PID controller

As mentioned in the previous section a PID controller was used to optimise the system. In general an open loop system, see figure 5.6(b), requires an input to act on the system to be controlled which will eventually provide an output. In such open loop scenarios, the system's performance does not provide the best results when accuracy is a major requirement[93–95]. A simple 1D example is shown in figure 5.6(a), where a system, centred at point A is programmed to move to point B. A possible approach is to determine its movement speed and therefore calculate the time it needs to get to the final point. This type of commanding is called an open loop as the required time to get to the final point is not adjusted based on the actual position of

the system. However, it is possible that the system will end up at point B' or B'' if it moves slightly slower or faster that the calculated speed respectively. In both cases the system will not reach point B as there was no input to compensate for such errors and make its own adjustments[93]. For the purpose of the laser stabilisation experiment we are dealing with one dimensional problem. When switching on the laser its default frequency value is A and it will be asked to move to frequency B. However, due to imperfections of the system it will probably end up at frequency B' or B'' and unlikely to be equal to B.

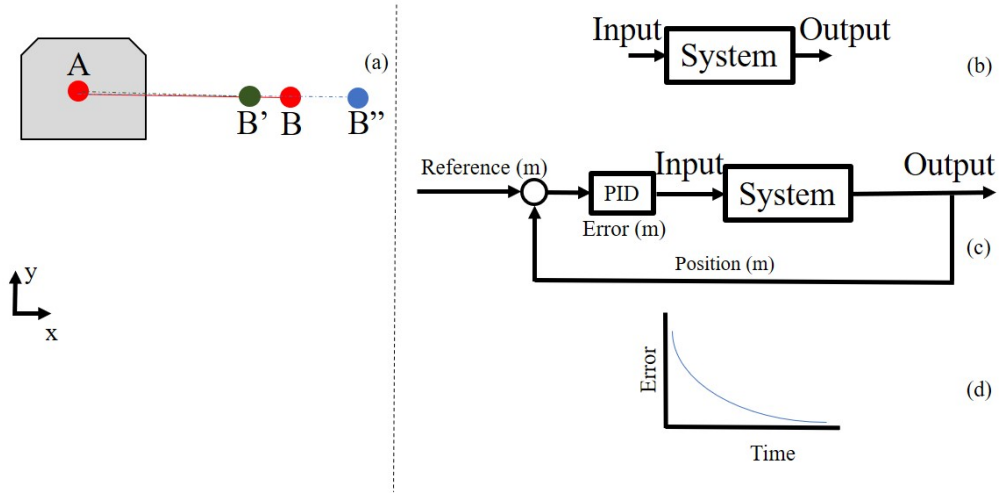

Figure 5.6 a) System programmed to move from A to B though some errors in the measurement can lead to point B' or B'' b) open loop system c) controlled system and d) optimal error signal response.

An effective way to improve the accuracy of the system is to introduce a feedback control which will essentially use the output of the system and feed it back. The system will therefore be able to make adjustments accordingly

(figure 5.6c). In a feedback control system, there will a reference signal which will be the desired value i.e. in this case the distance AB (measured in meters). This value is then compared to the measured one i.e. the system's current position (also given in meters). The outcome of this process will be an error signal that is essentially the difference between "where you are" and "where you want to be". The challenge here is to be able to convert an error signal (with units same as the output of the system) to an input that may or may not have the same units, that will force the signal to eventually reach the desired value (B). This is exactly what a controller does; it converts the error signal into a command that is sent back to the system. Furthermore, as time progresses the error (or difference between measured and desired position) is driven to zero (figure 5.6d). When there is no error present in the system it means that the measured position matches (or more realistically, is the closest it can be to) the desired position and the system is at a perfect state[93,95].

There are lots of types of controllers with the most famous being the PID controller (and its variations). PID controllers are simple, efficient and effective in a wide range of applications. The term PID is an acronym that stands for Proportional, Integral and Derivative. Each one of these terms describes how the error term is affected prior to being summed and sent back

into the system[93,94]. In the proportional path the error term is multiplied by a constant K_{P}, in the integral path the error term is integrated and then multiplied by K_{I} and in the derivative path it is differentiated and then multiplied by K_{D} (figure 5.7). The controller output is therefore the sum of the three different paths. Furthermore, one can refer to them as gains and they can be adjusted to any value in order to optimise a particular system that needs to satisfy certain requirements. By lowering or increasing each one of these gains it is possible to alter how sensitive the system is to each of these three paths. It is not necessary to have the three paths active simultaneously. For example, if the associated gain of derivative path (K_{D}) is set to zero, you can refer to the controller as PI, or refer to it as P if both K_{I} and K_{D} are set to zero.

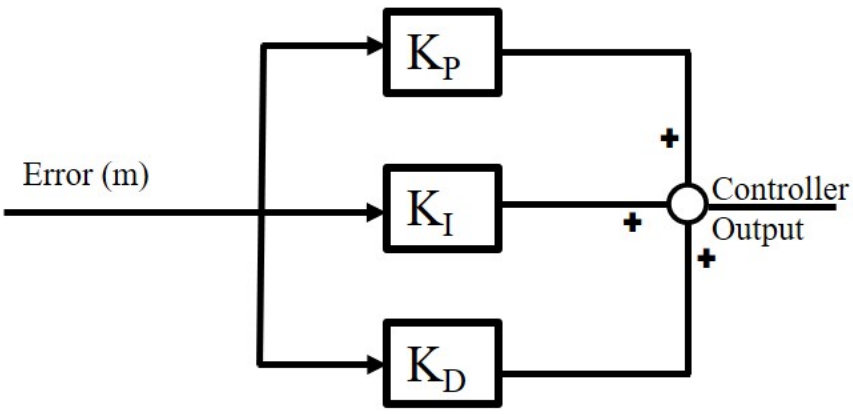

Figure 5.7 PID control system with three variable gains.

Figure 5.8 shows how the system is affected by each path with the blue line

representing the error in the system over time. For the first path P (figure 5.8a), the output is a scaled version of the error (depending on K_{P}). Therefore a large output will be produced when the error is large and the output will be zero when the error is zero. In the second path I, the error will be continuously summed and then multiplied by the K_{I} factor. In figure 5.8b it can be seen that the area under the sections of the graph are the integral path. The main reason why I is used is due to the fact that it can remove systematic errors present in a system [95]. Even if the error is very small at a given time, the summation will eventually prove that the error was significant enough to make adjustments to the output. The final path D (see figure 5.8c) is the rate of change of the error. When the change is slow the derivative path is small and when there is a faster change in the error the derivative will get bigger too. The summation of these three paths (or at least the active ones) is the output of the PID controller.

A simplified explanation of the contributions of each individual component P, I and D is essentially: P - provides stability over time but not accuracy, I - provides accuracy and D - is useful for sudden changes and setpoint variation. As the laser has an internal temperature/current control and as there cannot be any sudden changes in the acetylene spectra, D was not required and thus set to 0 for all the recordings.

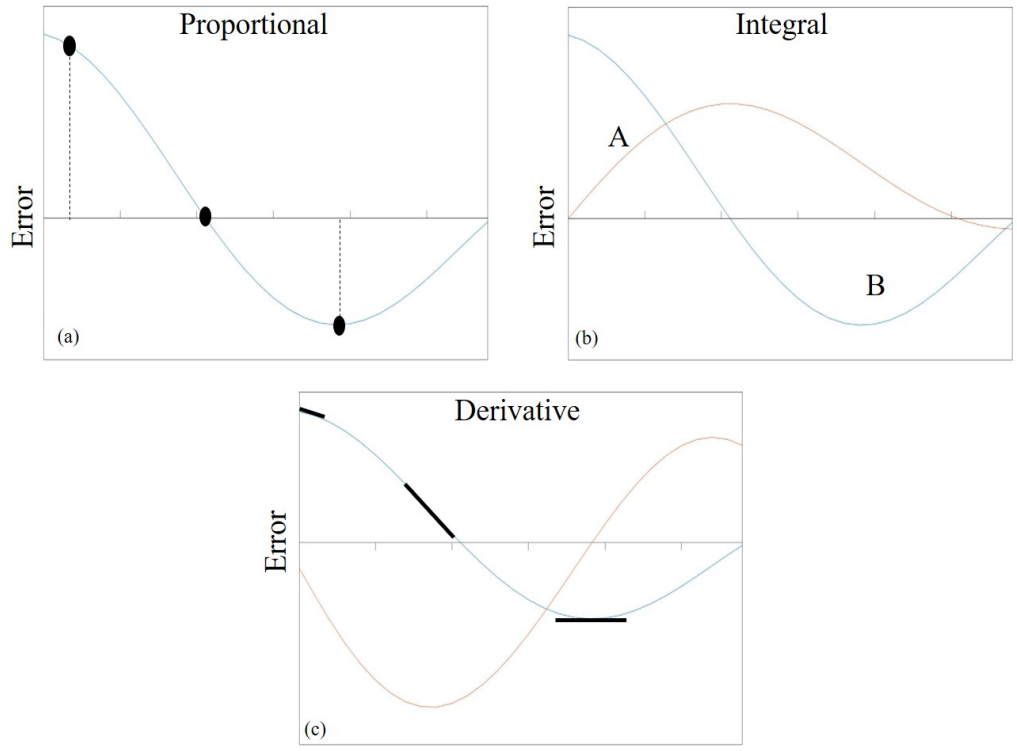

Figure 5.8 Individual effects of the three PID paths on error a)proportional path b) integral bath and c)derivative path.

For this experiment the laser can be locked by amplifying the "X" signal of the lock-in amplifier using the second summing amplifier. This is essentially a locking technique using only a P component. If the Arduino (PID input shown in figure 5.5) is also activated, then there can be a second P component. Initially the P component of the PID controller was set to 0.

A final point worth mentioning, is that when the gain(s) is set to a high value, the signal (in this case the interferometric signals) will begin to

oscillate. When this happens it is important to reduce the gain immediately until the signal stops oscillating. From literature it was found that determining the gain value where the signal starts oscillating helps optimising the PID controller (usually optimal gain value is the gain value before the signal starts oscillating divided by 2) [95–97].

5.2.2 Beat Frequency Measurements

Usually when referring to a laser being locked to a certain frequency, an uncertainty needs to be given i.e. the laser is locked to peak 9 of C_2H_2 ± 20 MHz. An easy way to specify the uncertainty of the locking system is to compare it with another system that has been locked to the same atomic line with higher accuracy. For this purpose, a Lasy 1550 from TEM Messtechnik was purchased. This is a stabilised tunable diode laser with an acetylene-referenced absolute frequency stabilisation system. Its stability was specified to be < 10 MHz. Thus, a set-up was constructed (figure 5.9) in order to beat the Pure Photonics laser, which was externally locked using a lock-in amplifier and a PI controller, against the Lasy 1550 which was locked internally. When beating two lasers i.e. when two beams are superimposed on the photodetector, the frequency generated is equal to the difference between the two.

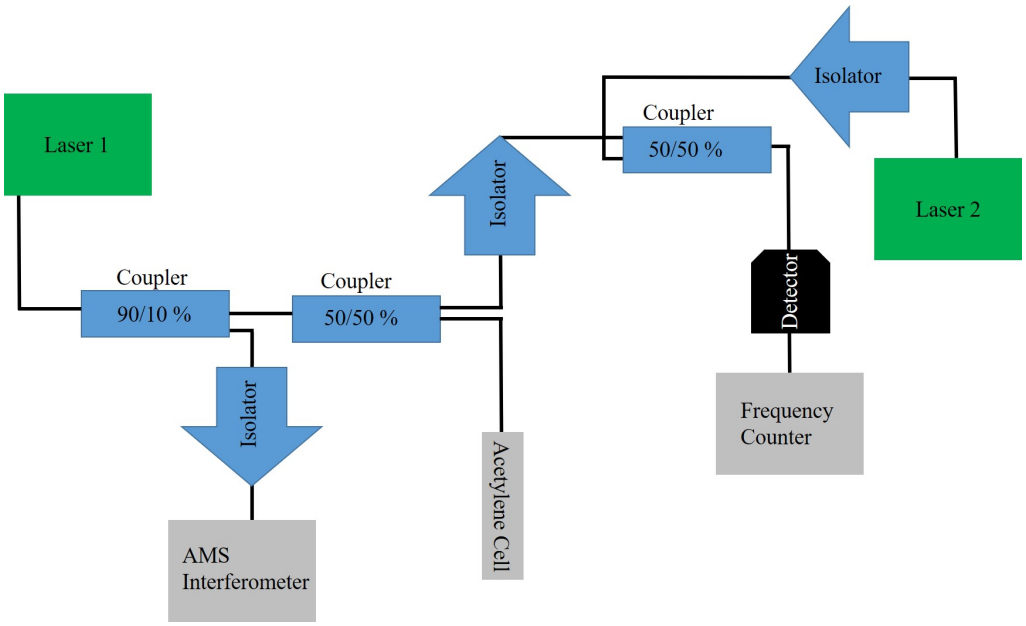

Figure 5.9 Beat frequency setup between Laser 1 (Pure Photonics) and Laser 2 (Lasy 1550). The light from Laser 1 is split into three (uneven parts using the optical couplers) and is sent to the interferometer, the acetylene cell and the frequency counter. The light from the Laser 2 was only sent to the frequency counter. Optical isolators were placed in the system in order to ensure that no light is sent back to the two lasers.

The two lasers that are used can be described with the following equations:

$$y_1 = A\cos(2\pi f_1)t \tag{5.9}$$

and

$$y_2 = A\cos(2\pi f_2)t \tag{5.10}$$

where y_1 and y_2 represent the electric field of each laser, f_1 and f_2 are the frequencies of Laser 1 and Laser 2 respectively and A the amplitude which is assumed to be the same for both lasers. When beating the two signals, y_{12}

can be written as:

$$y_{12} = A[\cos(2\pi f_1 t) + \cos(2\pi f_2 t)] \tag{5.11}$$

Using trigonometric identities ($cos(a + b)$ and $cos(a - b)$), equation 5.11 can be written as:

$$\cos(2\pi f_1 t) + \cos(2\pi f_2 t) = 2\cos(2\pi(f_1 t + f_2 t)/2)\cos(2\pi(f_1 t - f_2 t)/2) \tag{5.12}$$

From this is can be seen that the equation contains two frequencies, the average frequency f_{average} and ΔF, the frequency difference:

$$y_{12} = 2A[\cos(2\pi\Delta f/2)t][\cos(2\pi f_{average}/2)t]. \tag{5.13}$$

Thus, by summing two signals (from two different sources) that have a slight difference in frequency, the resulting amplitude will oscillate at a rate that will be equal to the difference between the two frequencies. This is known as the beat frequency.

For this experiment the purpose was to determine the stability of the Pure Photonics laser when locked and therefore the beat frequency of the two lasers will be able to provide this frequency stability. As shown in figure 5.9 the two signals were sent to the Frequency Counter (Digimess UZ2400) using a series of fibre coupled optics. The signal from the Pure Photonics laser

(Laser 1 in the figure) needs to be simultaneously sent to the interferometer, the acetylene absorption cell and the frequency counter. The signal from Lasy 1550 (Laser 2) was only required for the beat frequency. An optical coupler combined the two beams that were then sent to the photodetector and then to the frequency counter. The photodetector used was an InGaAs switchable Gain Amplified Detector (Thorlabs PDA10CS-EC) and the optical frequency difference of the two lasers lies within its bandwidth. The isolators were placed in the setup in order to prevent any back-reflections from reaching the two lasers. The frequency counter is a device that can measure the frequency of a repetitive signal by counting the cycles of a signal over the gate time that is manually set by the user. The results can be read directly on the display screen although the data were collected and sent to MATLAB for further investigation.

Figure 5.10 shows the beat frequency, for a 12-hour recording, of the two lasers when Laser 1 was in an unlocked state. This suggests that the frequency of at least one of the lasers is fluctuating by ∼20-30 MHz. As Laser 1 was not locked during this measurement (and Laser 2 was internally locked), it is safe to assume that most of the fluctuations observed on the trace were coming from Laser 1. By locking Laser 1, it is expected that the beat frequency will be reduced to a few MHz.

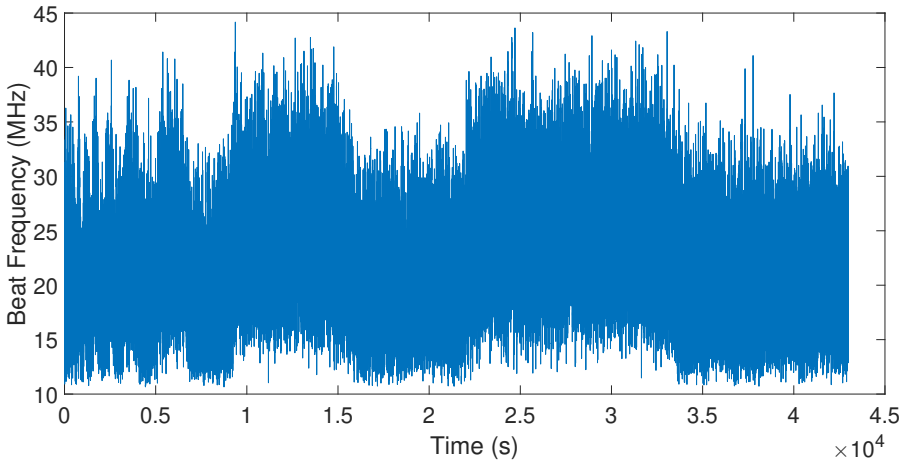

Figure 5.10 Beat frequency extracted from a 12-hour recording of Laser 1&2 whilst Laser 1 was in an unlocked state and Laser 2 being internally locked.

5.2.3 Allan Deviation

Using the data collected from the frequency counter it is possible to extract information about the noise within the recorded signal over time. The data can be presented in a graph that is usually referred to as the Allan Deviation graph. This is essentially a measure of the frequency stability of a system and it also provides insight into determining different sources of noise. This is because it is possible to correlate them to the time-scales on which they occur on the graph. The Allan deviation is given by:

$$\sigma_y(\tau) = \sqrt{\frac{1}{2}\langle(\bar{y}_{\mathrm{n}+1} - \bar{y}_{\mathrm{n}})^2\rangle}, \tag{5.14}$$

where τ is the time period of the observation, $\bar{y}_{\mathrm{n}}$ is the average frequency of the n^{th} set of points over the time period τ.

A common Allan deviation graph that describes the frequency stability ($\Delta\nu$) of a system is presented in a log-log graph and at very short time-scales (ΔT) it is expected to be high due to noise (limited fundamentally by Fourier Transform and for this system, very short time scales is $\sim 10^{-6}$ seconds). At longer time-scales as the noise averages out, the Allan deviation decreases. At even longer time-scales the Allan deviation will be slightly higher as the laser is expected to start drifting. This is the case when the laser is not stabilised. When the laser is locked to a certain frequency there will not be any drift at long time scales[98,99]. One main source that causes this drift is temperature fluctuation. The data collected for the beat frequency (described in the previous sub-section) were also used to plot the Allan deviation for this experiment.

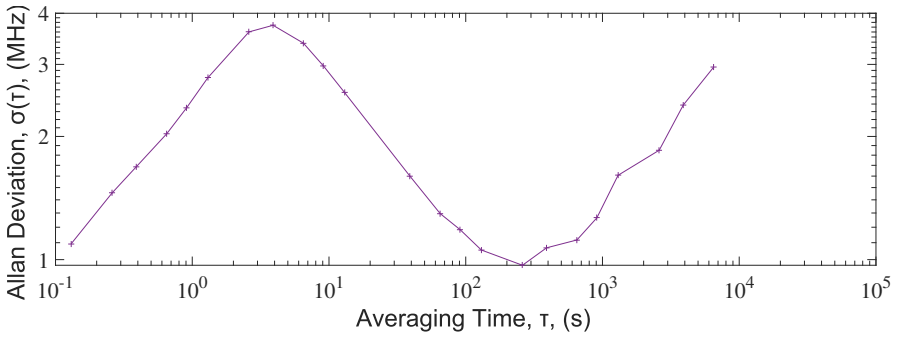

Figure 5.11 Allan deviation extracted from the beat frequency of figure 5.10

Figure 5.11 shows the Allan deviation extracted from the beat frequency data of figure 5.10 where Laser 1 is unlocked. The plot agrees with literature and shows that at longer time-scales the trace is affected by drift. It is also expected that by locking Laser 1 and repeating the measurement, the frequency stability at longer time scales will be reduced to less than 1 MHz.

5.3 Interpretation of Data & Improving System's Performance

In this section the beat frequency measurements and the Allan deviation graphs along with the interferometric signals are analysed in order to extract information about the stability of the laser(s).

When locking the Pure Photonics laser, the aim was to minimise "X" (output of the lock-in amplifier described in Section 5.1) until it gets as close to 0 as possible. By manually fine tuning the frequency of the laser, by a few MHz at a time, it is possible to reduce "X" before activating the feedback loop. This does not affect the quality of the system but it is recommended as it minimises the required work of the feedback loop. The laser was locked at peak 15 of acetylene's P branch (defined by literature as 1534.0987nm±0.0003)[79]. This peak is different to the one used in

Section 4.5.2 when an initial characterisation of the laser was performed. This is because the second laser used for the beat frequency measurements was internally locked at that frequency.

Thus, once the first laser (Laser 1) was manually locked, long (and short) term recordings were taken for the interferometric signals along with the beat frequency and the Allan deviation, using the set up shown in figure 5.9. The interferometric signals ($I\&Q$) along with the error signal of the lock-in amplifier and the transmission signal through the acetylene cell were recorded using a digital oscilloscope (3403D Picoscope). The frequency counter was used to collect the beat frequency of the two lasers. The data were sent to the computer for further analysis in order to extract the Allan deviation.

Figure 5.12-5.15 show the data that were taken for a 12-hour recording: Figure 5.12 shows part of the 12-hour long recording (33minutes and 20 seconds) using the Picoscope and figure 5.13 shows IVsQ for the set of data that are shown in figure 5.12 along with the wrapped/unwrapped phase.

The main observations here were that $I\&Q$, the interferometric signals (blue and red) of figure 5.12, were fluctuating more than the green signal (signal through the acetylene cell) and that there was an interferometric drift that

was happening throughout the recording. This drift was more obvious at ∼20 minutes onwards. From figure 5.13 it can be seen that the interferometric drift was not very large as the measured phase did not require unwrapping (unwrapped and wrapped phase were explained in Chapter 4.5.3). The interferometric drift ΔL was a slow change over the entire trace which suggests that it was caused due to thermal effects, such as the increase in room temperature over time. Vibrations can also affect ΔL but in a much shorter time scale ($\ll$ second), which was not the case in this trace. As for the amplitude fluctuations observed in the interferometric signals of figure 5.12, they were not present on the signal that was passing through the acetylene cell (or the error signal - yellow trace of figure 5.12). This means that fluctuations of the interferometric signals were not caused by frequency instabilities Δf. Therefore the cause of these fluctuations was most likely to be variations in the refractive index Δn ($\leq$ second). The fluctuations are also visible in the unwrapped phase of figure 5.13.

However, the graph for the beat frequency (acquired by simultaneously running the Lasy 1550 laser - see Section 5.2.2) was found to be unexpectedly unstable (see figure 5.14). The graph shows a large number of spikes that did not appear in figure 5.12&5.13 of this 12-hour recording. The measurement was repeated N times with similar features seen. There are actually two

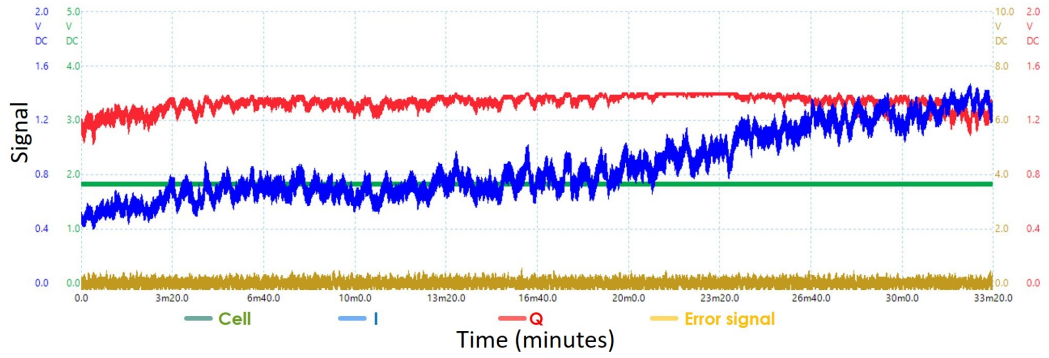

Figure 5.12 33 minutes and 20 seconds trace of a 12-hour recording of the interferometric signals I and Q (blue and red respectively), the signal that goes through the acetylene cell (green) and the error signal of the lock-in amplifier (yellow). At ∼23 minutes Q, the red signal, had reached the top of the fringe - the detector was not saturated at this point.

different sets of features in this measurement. Figure 5.15 shows two different time periods of the beat frequency measurement shown in figure 5.14. Figure 5.15a) suggests that there is a short term frequency glitch that is present in the entire 12-hour trace. Figure 5.15b) shows a long term frequency fluctuation that is present only a few times in the 12-hour recording.

Looking at the data presented so far for this experiment, it was obvious that Laser 1 (the Pure Photonics laser) cannot be the source of either of the two effects. Since the laser was used to calculate the interferometric signals $I\&Q$, and figures 5.12 and 5.13 though a bit noisy, do not show any of these two effects, it was therefore sensible to exclude this laser as a potential source. Calculating $I\&Q$ using Laser 2 (the TEM Lasy 1550) will therefore

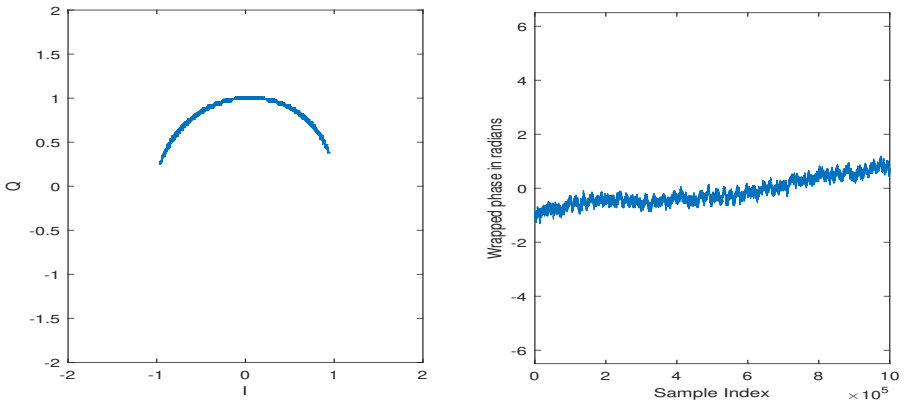

Figure 5.13 Left: IVsQ for the 33min20. Right: The phase of the IQ signal. As the interferometric pattern did not move to the next or previous fringe there is no need to unwrap the phase.

determine whether or not it is responsible for these frequency fluctuations.

Thus, the interferometric signals $I\&Q$ as well as the signal through the acetylene cell were recorded for a short period of time using Laser 2. The results are shown in figure 5.16. This trace shows enough evidence to support that both frequency fluctuations, short and long term, are caused by this laser. One can argue that the fluctuations on the two interferometric signals (blue and red) can be a result of temperature variations or length instabilities of the interferometric set-up. However, the third trace (signal through the acetylene cell, green) is not susceptible to any of the two factors and it is still affected in the same way. Furthermore, since the power is rising when Laser 2 is misbehaving, it indicates that the laser is not switching itself off. Unfortunately there was no way to resolve either of the two issues,

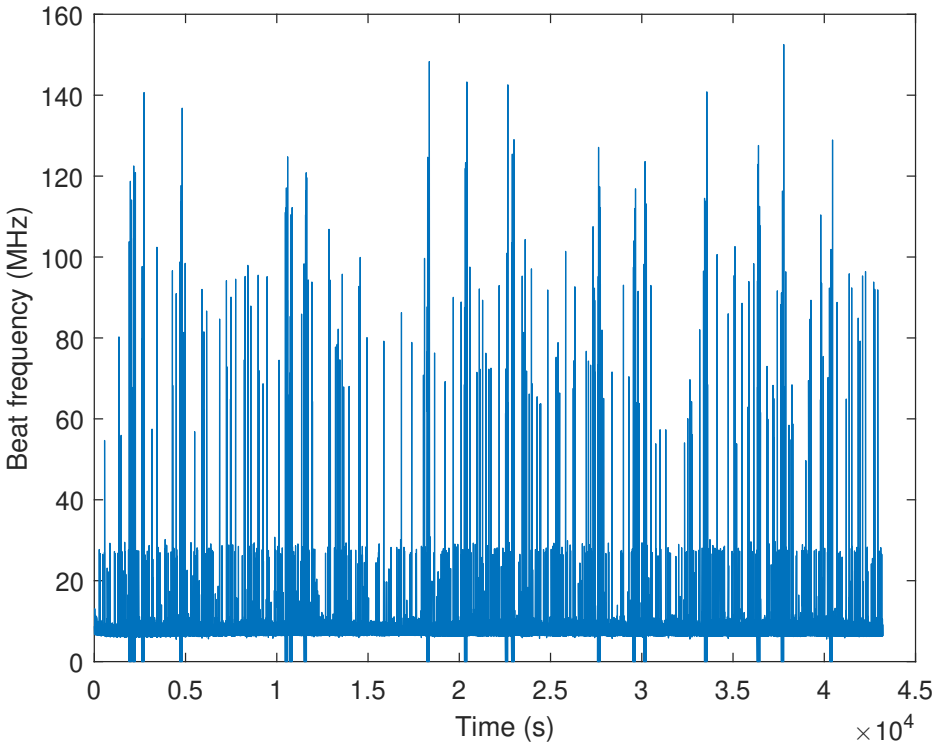

Figure 5.14 Beat frequency graph between the two lasers for a 12-hour recording.

though it was discovered that the long term frequency fluctuations were a result of the laser being in an unlocked state. It is worth mentioning again that this laser has an internal frequency stabilisation system.

Nonetheless, the Allan deviation of the beat frequency measurement was calculated and is shown in figure 5.17. As described in Section 5.2.3, the Allan deviation at very short time-scales is expected to be high. Then as the noise averages out, the Allan deviation decreases. However, in this case, at

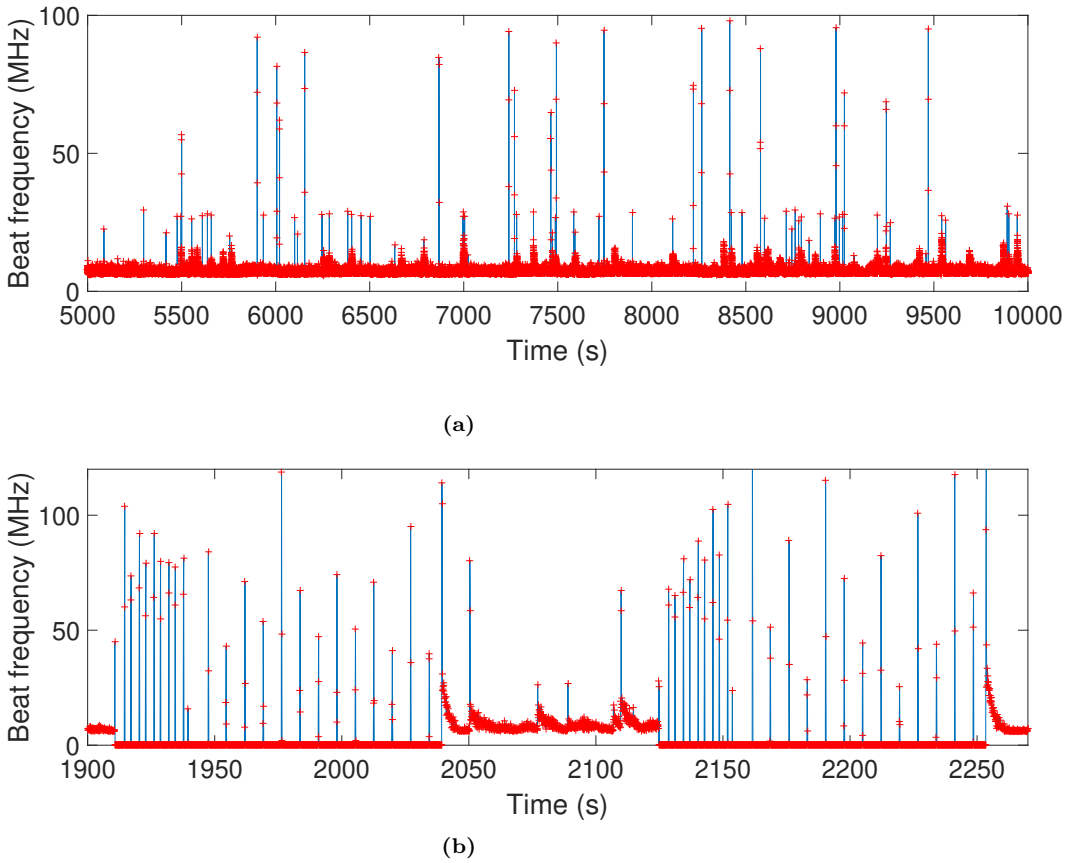

Figure 5.15 Two different effects in the measurement (a) some sort of short term frequency glitch casued by one laser and (b) some sort of longer frequency fluctuation caused by one of the two lasers.

100 seconds the Allan deviation increases and this corresponds to the Laser 2 randomly unlocking itself. At even longer time-scales the Allan deviation will be slightly higher as the frequency of the laser is expected to start drifting. This is the case when the laser (in this case Laser1) is not locked. When the laser is locked there will not be a frequency drift and the Allan deviation is low as shown in figure 5.17. This is a significant decrease at long time-scales compared to the Allan deviation where Laser 1 is unlocked (see figure 5.11).

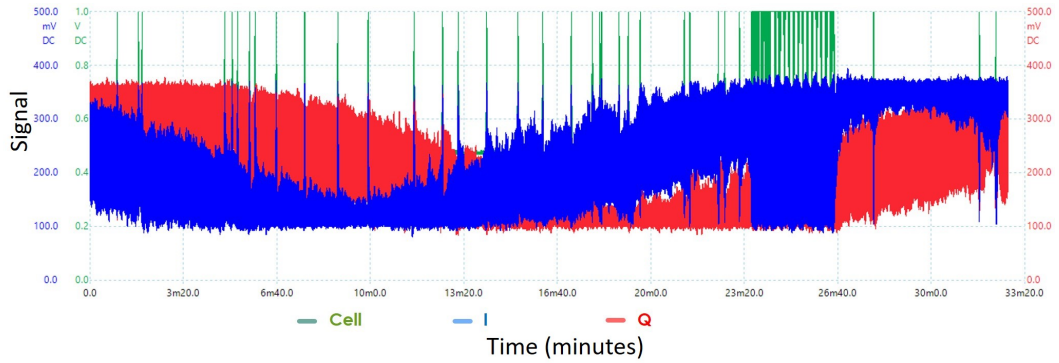

Figure 5.16 Using Laser2 i.e. the TEM Lasy 1550 in the interferometer. Figure shows the signal through the acetylene cell (green) and I&Q (blue and red respectively).

Though Laser 2 was not completely reliable the experiments were continued in order to optimise the locking system of Laser 1. A series of recordings were taken with Laser 1 not being frequency stabilised, being frequency stabilised with P component only and being frequency stabilised whilst applying a PI control. Figure 5.18 shows the Allan deviation plotted for six 12-hour recordings. The constants for PID control were set to: K_{P}=0.1, K_{I}=400 and K_{D}=0 (this was essentially a PI control loop). K_{P} was set to a very small number as the feedback loop without the PID controller (Arduino) is essentially providing the "P" term.

From figure 5.18 it can be seen that when the PI controller is activated i.e. PI (1)&(2), the Allan deviation is similar to the Allan deviation of P. This was expected as the integral term I of the PID controller provides accuracy

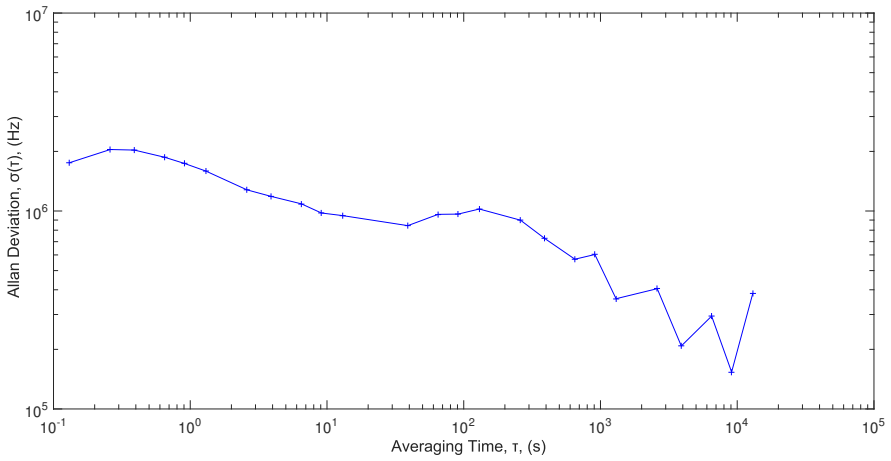

Figure 5.17 Allan deviation of the beat frequency measurement shown in figure 5.14, for a 12-hour recording, where both Laser 1&2 are locked.

to the system and the Allan deviation graph is an indication of the stability of the system. The difference between the laser being frequency locked and not being frequency stabilised (always referring to Laser 1) can also be seen from the same figure. Figure 5.18 contains 3 plots, unlocked (1),(2) and (3), where Laser 1 did not have any external systems controlling its frequency. This is a confirmation that the feedback loop(s) are indeed improving the stability of the system at short and long times scales. At short time scales (3 seconds) the feedback loop has corrected for fluctuations that correspond to an internal temperature (or current) control system and at long time scales the feedback loop has corrected for the frequency drift. Furthuremore, an interesting feature of this graph is plot "unlocked(1)" (this is figure 5.11). The noise at 100 seconds is not present i.e. Laser 2 did not go to an unlocked

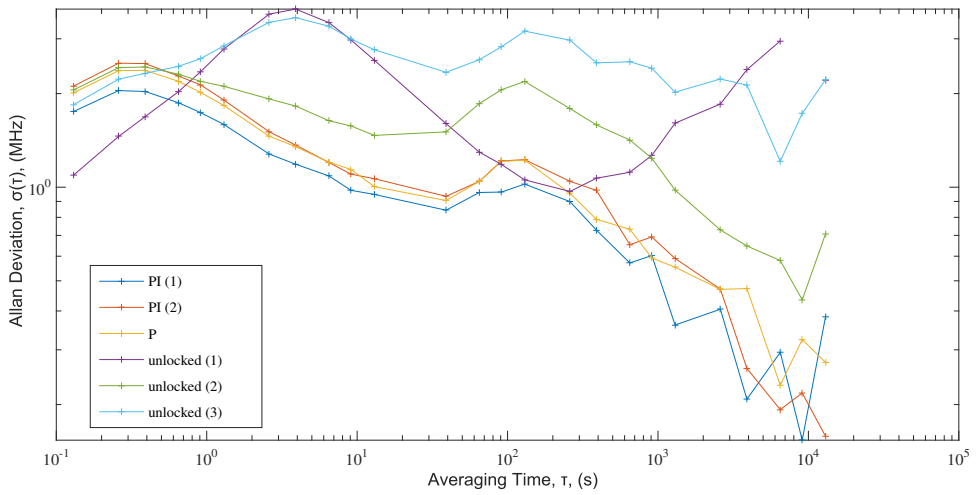

Figure 5.18 Allan deviation plotted for multiple 12-hour recordings when the Laser 1 was not frequency stabilised - unlocked (1),(2) and (3), was frequency stabilised with P only - P, and was frequency stabilised using the PI control - PI (1)&(2).

state during the recording and there is no peak at short time scales (0.3 seconds) i.e the short term frequency glitch is not present either. This was the only recording that was acquired where the frequency of Laser 2 was stable throughout the measurement. Unfortunately, as Laser 1 was unlocked during the measurement it is impossible to extract information about the quality of the lock-in amplifier or the PI controller. A combination of the beat frequency and Allan deviation graphs thus led to the conclusion that at these two time scales (short and long term frequency glitch at 0.3 and 100 seconds respectively) it is indeed impossible to extract information about the behaviour of Laser 1 (as the dominant frequency fluctuation is generated by Laser 2), but the rest of the data is valid.

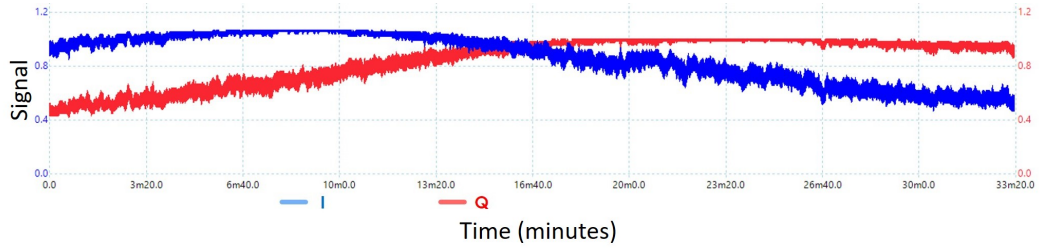

(a)

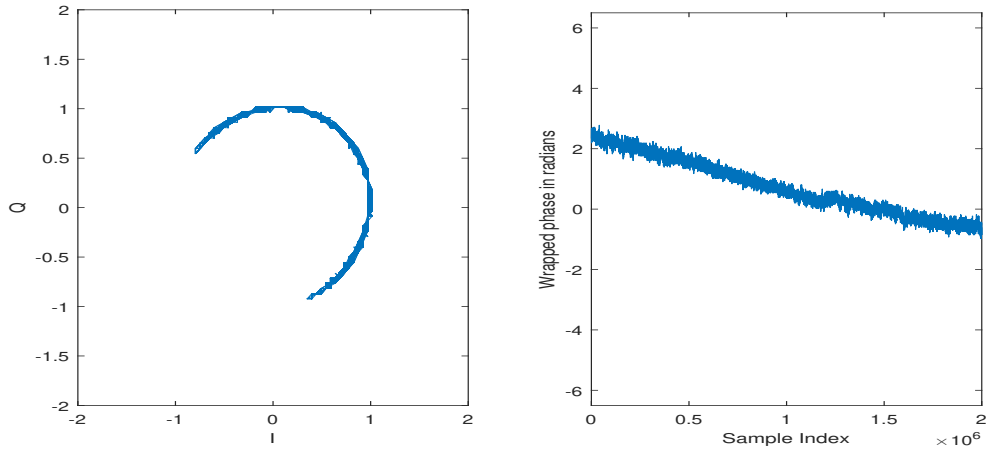

(b)

Figure 5.19 (a) Interferometric traces I and Q. At ∼8 and at ∼23 minutes I and Q respectively, had reached the top of the fringe - the detectors were not saturated at these points. (b) Left: IVsQ for the 33min20. Right: The phase of the IQ signal. As the interferometric pattern did not move to the next or previous fringe there is no need to unwrap the phase.0

The noisy traces shown in figure 5.12 were also a concern. Fortunately this was an easy fix by covering the interferometer so that any movement and air flow will not affect the measurement. Figure 5.19 shows the interferometric traces (I&Q) along with the $IVsQ$ for a 32 minutes recording (part of a 12-hour recording). As the effect of air flow was minimised and the

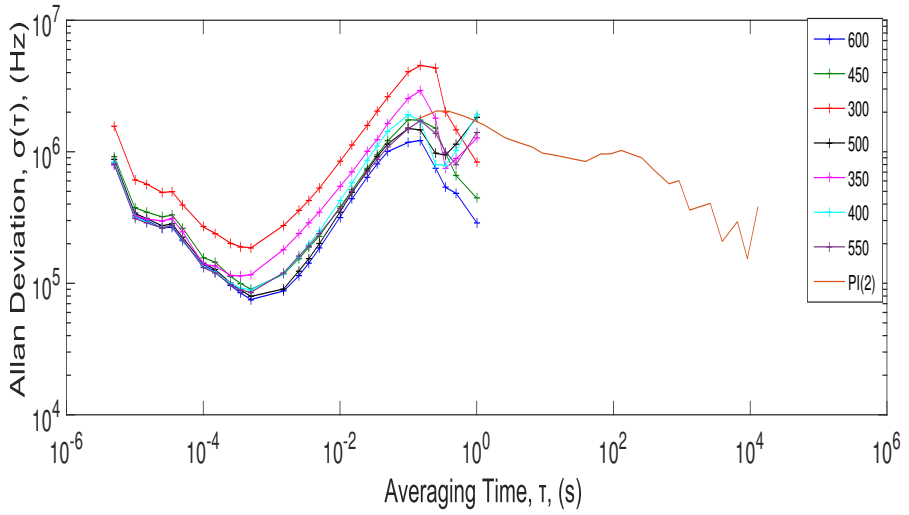

Figure 5.20 Allan deviation of the interferometric traces for short time scales for different I gain values. Red: I=300, Green: I=350, Blue: I=400, Black: I=450, Pink: I=500 and Light Blue: I=400 and Purple: I=600. The plot PI (2) from figure 5.18 is also shown.

interferometer was stable over time, the I gain component was optimised.

Figure 5.20 shows the Allan deviation at very short time scales of the interferometric traces for different I gain values for Laser 1. The graph contains plots with different I gain values (from 300 up to 600, with 50 step change). Beyond this range, the increase of the I gain seemed to have an effect on the interferometric signal $I\&Q$ (the signals began to oscillate). An attempt was made to increase both I and P (using the switchable gain on the summing amplifier) but the interferometric signals were distorted - the interferometric signals were oscillating. This suggests that the default P gain was enough. The plot PI (2) from figure 5.18 is also included in this graph.

The data obtained agree with the data provided by the manufacturer (in magnitude and time scale) from 10^{-4} to 10^{-1}. The drift on short time scales is an effect that the feedback loop system cannot correct for as its bandwidth is 1Hz (1 second). The bandwidth of the feedback loop is set by the integration time of the lock-in amplifier. Reducing the value to below 1 second had a negative effect on the system i.e. the signal became unstable .

5.3.1 Further Discussion & Comments

In this Section, a series of graphs along with their interpretation were presented. Unfortunately, due to some technical issues with Laser 2, the graphs of beat frequency and Allan deviation in Section 5.3 were negatively affected. Nonetheless there are a few points worth discussing.

Even though the beat frequency graphs (see figure 5.14 and 5.15) have an excessive amount of fluctuations caused by two effects (short and long term frequency glitch of Laser 2), it is worth noting that when none of the effects are present the beat frequency is stable to less than 7 MHz (baseline of figure 5.14). This suggests that Laser 1 is stable over a long time. By repeating the same locking technique multiple times and looking at the beat frequency data each time, it was found that the baseline was always at 7 MHz (maximum difference of 0.2-0.4 MHz between traces). This suggests that the

accuracy of the system was high. Both lasers were locked to the centre of the same acetylene peak but the beat frequency measurement suggests that there is a 7 MHz difference. This is an effect of pressure shift of the two acetylene cells (the 20 Torr cell shown in figure 5.5 and the cell inside Laser 2). From literature it was found that the expected pressure shift is 0.29 MHz/Torr which agrees with the beat frequency measurement as the pressure of the acetylene cell inside Laser 2 is 40 Torr[81].

One of the main tasks of this experiment was to be able to determine the uncertainty of the frequency stability of Laser 1. Though it is impossible to determine the number with high accuracy, figure 5.17 can give a good estimate. The graph suggests that Laser 1 was locked to better than 0.4 MHz at 10^4 seconds.

A final point of discussion for this chapter is the limitations of the frequency measurements. The device i.e the frequency counter transfers the data to the computer via an RS-232 connection. This is rather slow. The device records data for 100 ms and it requires 30 ms to transfer the data. Making the assumption whether or not the 30 ms is a substantial time interval, the gate time during the post-processing analysis can be interpreted as 100 ms or 130 ms. Thus, using the same set of recorded data (see figure 5.21), two

slightly different Allan deviation graphs can be plotted. At short time scales the points of each graph have different x and y positions. At long time scales the magnitude of the two plots are the same and there is a small difference in the x-position of each point. One sensible way to overcome this problem is to plot both Allan deviations for each set of data and look at the plot with 100 ms gate time for short time scales and the plot with a 130 ms for long time scales. However, figure 5.21 illustrates that the effect i.e. the difference between the two plots, is very small.

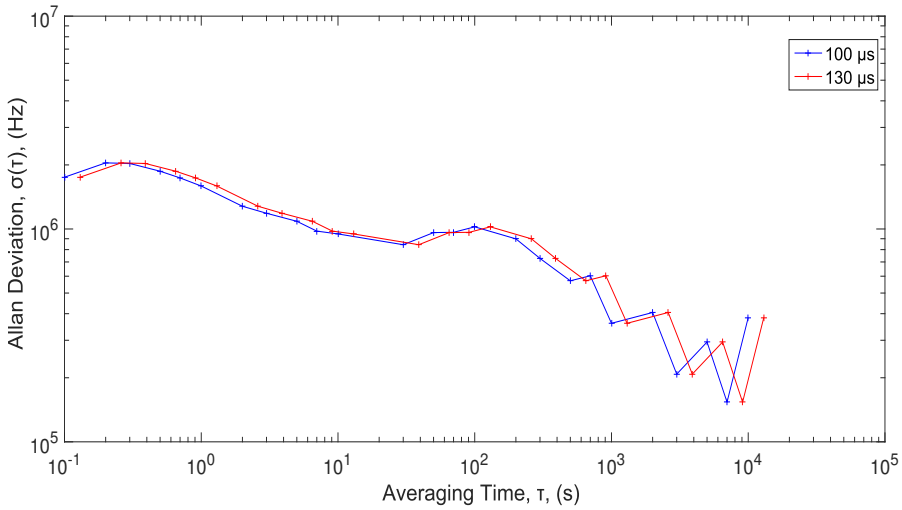

Figure 5.21 Allan deviation of one set of data plotted for different integration times. Blue: 100 ms and Red: 130 ms.

This Chapter's focus was the quality and improvement of the frequency stability system for a diode laser. The stability of the laser without any feedback control loop is ∼30MHz whereas when it is locked its stability is

$\sim$0.4MHz. Translating frequency stability (Δf) into distance uncertainty, for an open system, gives Δd=153 nm. This can be done by extracting Δd from equation 2.1 and plugging it into Δf=c$\Delta\lambda/\lambda^2$. Then $\Delta d/d$=$\Delta f/f$, where d=1 for the AMS interferometer. For a controlled system the distance uncertainty is Δd=2 nm. The laser, though incredibly stable without any external systems, has its frequency stability improved by the addition of a feedback loop, which will help the AMS scale bar to achieve the precision that it is promising in its measurements[70].

Chapter 6

Developing an Acetylene Fibre Gas Cell

6.1 Fabrication

Fibre fabrication is actually a complicated and very delicate process. Different research groups have different approaches but as mentioned in Section 3.2 the stack and draw method was used. The application (mentioned in Chapter 1.4) required only a flat transmission band at 1550 nm - Single mode and low bend loss were not required. This was not technically a demanding design.

When fabricating a new optical fibre, literature can assist in determining important parameters of the design. These factors were discussed in

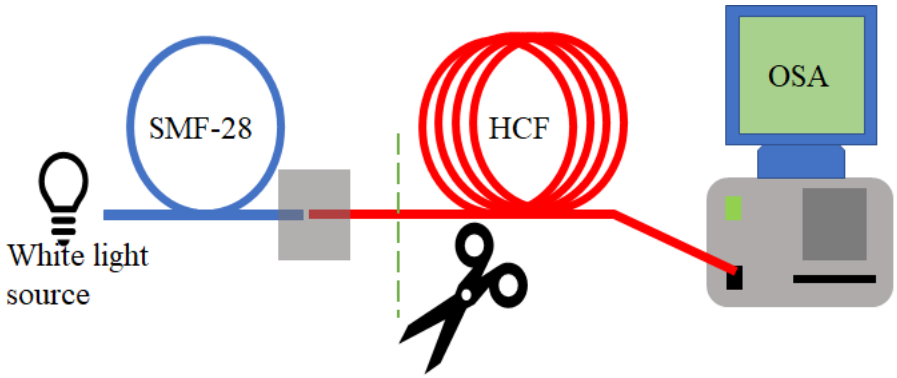

Figure 6.1 Experimental setup for cut-back measurements of the hollow core fibre.

Section 3.1.3. Furthermore, a computational design (in COMSOL or MATLAB) can also help optimising certain parameters before attempting a draw. COMSOL is mainly used when designing a new structure as it can simulate the electromagnetic model.

For the purpose of this research, a simpler model in MATLAB was used which simulates the fit of $2N$ rings (N resonators and N gaps) inside a circle. A maximum size tolerance for the resonators was set to $\sim 0.5\%$. Ideally this number must be set to the lowest possible, but sometimes the diameter monitor system (see figure 3.9a for the resonators and 3.9b for the fibre) might be slightly misaligned. This is also crucial when it comes to uniformity along the length of the fibre. The negative curvature of the fibre will be affected if the resonators do not maintain their size. From a practical perspective, the stacking process also becomes difficult; if the resonators are

bigger than the desired size they will not fit in the stacking tube and one or more can potentially break. If the resonators are smaller than the desired size the stack will be too loose and can easily move when placed vertically on top of the cane tower.

Uniformity is indeed important when high transmission bands are required. However, it is hard to control this during the fibre fabrication. The laser diameter monitor that is placed just underneath the furnace of the fibre tower (figure 3.9b) can measure the outer diameter but this does not guarantee the uniformity of the microstructure.

Furthermore, it was found that the drawing temperature must be set to the lowest possible temperature. Higher temperatures correspond to lower tension and this can potentially cause the resonators to collapse in the cladding (low tension means less control, thus more variation in the structure). From experience it was found that in order to reach and maintain the desired tension, the "correct" temperature was within the range of 1980-2000°C and it was always dependent on the condition of the element inside the furnace on the day of the draw.

Pressurising the resonators, and only the resonators, whilst keeping the core

open to atmospheric pressure was the most delicate part of the fabrication. A procedure was developed where UV glue was used to completely isolate the core from the resonators on one end of the preform. The inflation of the resonators needs to be done carefully during the fabrication as it does affect the position of the transmission bands (Equation 3.8) and how lossy the fibre will be. From experience, a 80-90% resonator inflation is considered the most efficient design (maximum inflation is defined as the diameter of the resonators when they touch each other).

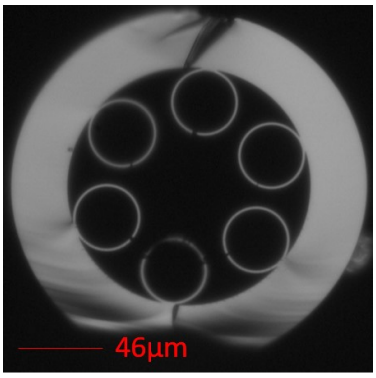

(a)

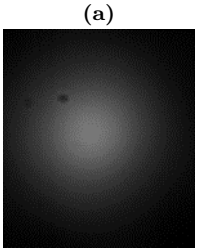

(b)

Figure 6.2 The 6-ring hollow core fibre design. a) Microscope image and b) Far field shows the leaky mode of the fibre using an IR camera.

After careful consideration of the previous points, a 6-ring hollow core fibre was designed and fabricated in an attempt to satisfy the only requirement of the application: flat transmission band at at 1550 nm. Though it was stated that single mode is not necessary for this application, such a fibre will easier to characterise.

In order to characterise a hollow core fibre (i.e. measure its attenuation), one needs to do a cut-back measurement. As shown in Figure 6.1, a single mode fibre at 1550 nm, SMF-28e, with 10 µm core size was used to couple light from the white light source (Energetiq Xenon Lamp LDLS) into the hollow core fibre. The other end of the hollow core fibre was plugged into an Optical Spectrum Analyser (OSA) which can provide a transmission spectrum from 400 nm to 1700 nm. The process is as follows: take a spectrum measurement with a long piece of hollow core i.e. 60 m, cut ∼40-50 m off the fibre and then repeat the measument with only 10-20 m left in the system. When removing a piece of the hollow fibre it is essential to leave the coupling end untouched in order to ensure that input power in both cases is the same. Both measurements can be repeated a few times in order to ensure consistency. The attenuation of the cut piece can be determined by:

$$\alpha(\lambda) = \frac{1}{\Delta L} 10 log_{10} \frac{P_2(\lambda)}{P_1(\lambda)}, \tag{6.1}$$

where P_2 and P_1 are the spectral power densities measured at the output of the short and long piece respectively and ΔL is the length difference between the two pieces[100].

It was previously stated (Section 3.1.3) that in order to achieve single mode guidance in a hollow core photonic crystal fibre the ratio between the diameter of the resonators and the core diameter must be $\sim$0.66[66]. Taking this into account along with all the information above, a 6-ring fibre was made (Figure 6.2a) and the transmission loss and bend loss can be seen in Figure 6.3 and 6.4. The fibre has a 160 µm outer diameter, 46 µm core diameter and the diameter of the resonators is 28 µm. Both mechanical and optical properties of this design satisfy the requirements of the experiment and the fibre is single mode over 60 m (Figure 6.2b). Therefore, this hollow-core fibre design was implemented into the acetylene gas cell experiment.

6.2 Vacuum and Gas Handling System

The purpose of this experiment was to determine whether the hollow core fibre design that was fabricated can provide a set of acetylene absorption peaks (once filled) at low pressures with the smallest possible pressure shift.

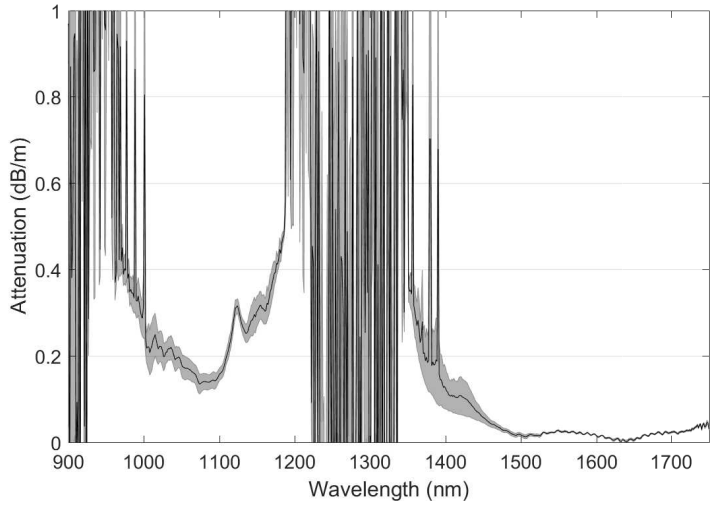

Figure 6.3 Attenuation over 1m obtained through a cut-back measurement of the 6-ring hollow core fibre design. There is no transmission bellow 900 nm and between 1250 nm and 1330 nm for this design.

It was also interesting to observe the difference between a fibre gas cell and the acetylene reference cell that was previously used for the laser calibration. It was expected that the shift of the absorption peaks will be more noticeable at higher pressures. Figure 6.5 shows an initial experimental setup that involves both the acetylene reference cell and the hollow core fibre. A tunable diode laser (Yenista TUNICS T010S-HP) with 100 nm tuning and sweep range (1500 nm-1600 nm) was used. A 90/10 coupler split the light to the reference cell and the hollow core fibre. A set of mirrors and lenses (20x and 10x) was used to maximise coupling efficiency. The fibre was placed in between two glass windows as shown in figure 6.5. These windows are essential for the light transmission whilst the fibre is sealed from atmospheric

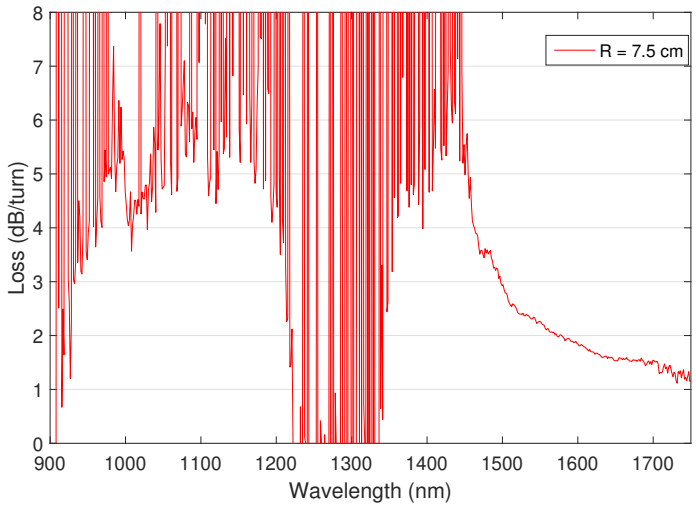

Figure 6.4 Bend loss measurement of the 6-ring hollow core fibre for bend radius of 7.5 cm.

pressure and filled with acetylene. The input and output window is a 5 mm and a 7 mm thick AR coated glass window (Thorlabs) respectively. The location of the gas cell is outlined by the dashed box. The parts involved in filling and releasing the pressure in the fibre cell are shown in Figure 6.6.

The two cells with the tightly fixed AR glass windows were connected to the vacuum pump through a metallic tube and there were two valves for controlling the flow. The original design was developed by Dr. Samuel Bateman and a more detailed explanation can be found in his thesis[101]. The real time pressure inside the cells was always shown by the gas pressure monitors. The hollow core fibre was carefully placed at the back side as shown in the image (on top of red plastic surface), with no tight bends. The

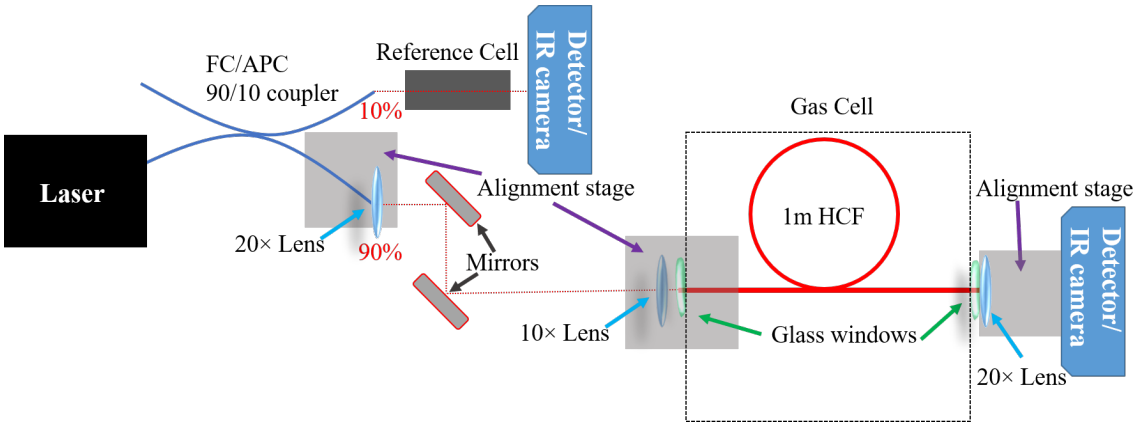

Figure 6.5 Schematic representation of the experimental setup. This does not include the vacuum and filling system. 10% of the light is sent to the reference cell that was previously used for the laser calibration and 90% of the light is sent to the hollow core fibre. A set of mirrors and lenses was used to maximise coupling efficiency. The edges of the hollow core are sealed with 2 AR coated glass windows. A detector and an IR camera were used to record the transmission spectrum and look at the modes of the fibre. The location of the gas cell is outlined by the dashed box.

two ends of the fibre were first cleaved and then fixed inside a metal tube. The tube was then clamped onto the cell, with the fibre being very close to the AR window. Any air gaps between the fibre and the metal tube were prevented by the addition of o-rings. In the same way an o-ring was placed between the metal tube and the cell. The input cell was also connected to the acetylene vessel and by enabling a series of valves the fibre gas cell can be filled.

Monitoring the pressure of the cell in order to determine the leakage rate was very important. In such experiment it is essential to maintain the same pressure throughout a full set of measurements. In order to test this, the cell

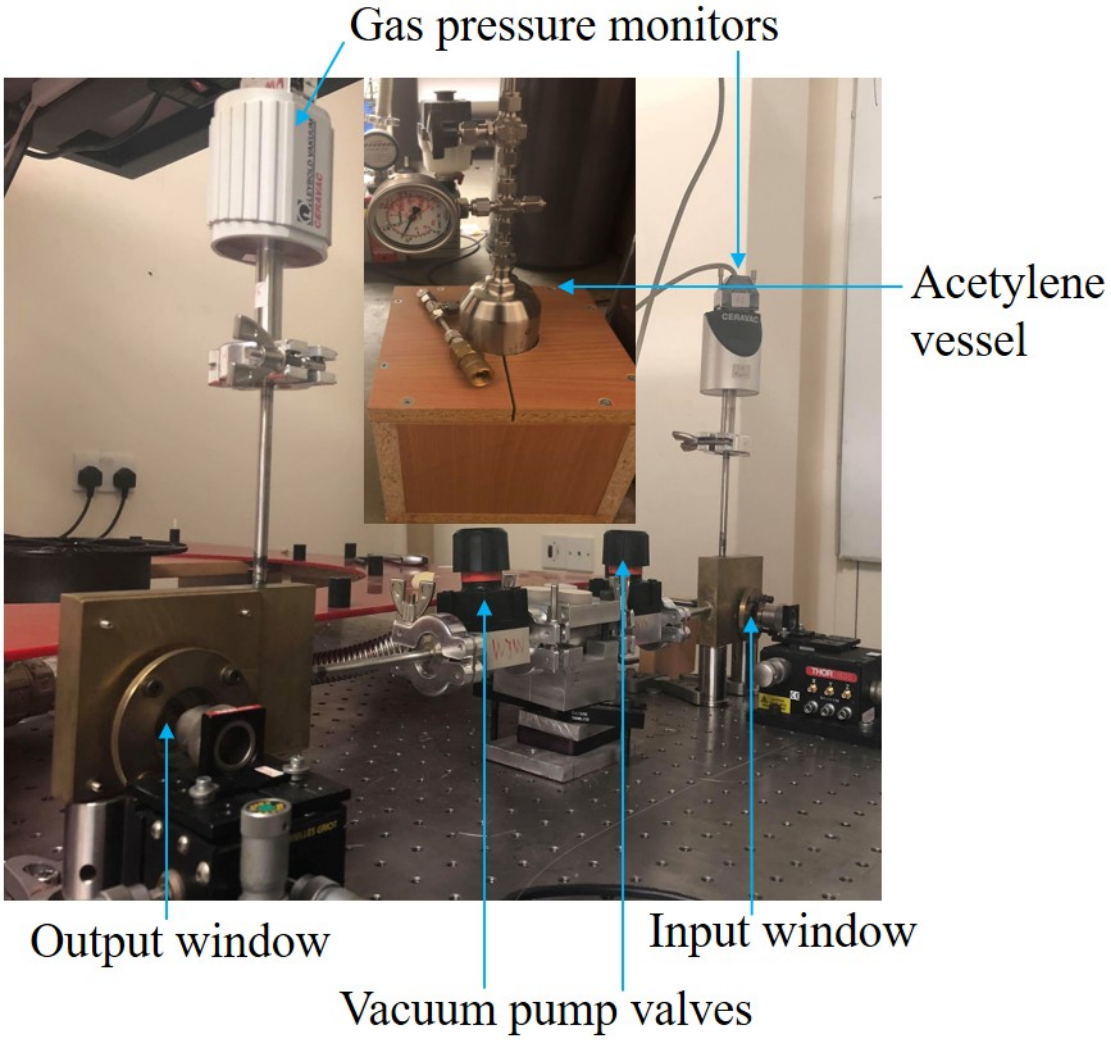

Figure 6.6 Parts involved in the fibre cell design. Input and Output windows: they seal the optical fibre from atmospheric pressure and allow light to be transmitted, vacuum pump valves: control the pressure flow of the system, gas pressure monitors: monitor the pressure at the two ends of the cell, acetylene vessel: small vessel containing a total of 1-2g of acetylene.

was completely evacuated and left at that state for day. It was found that a total of 0.001 83 mbar was leaked into the fibre after 24 hours, which means that the pressure inside the fibre can be easily maintained for a few hours. Once the fibre was completely evacuated, it had to be filled with acetylene gas. The time taken to fill the fibre with a gas is given by:

$$\tau = \frac{128\eta l_t^2}{\pi^2 d_t^2 P_0}, \tag{6.2}$$

where l_t is the length of the fibre, d_t is the diameter of fibre, P_0 and η are the pressure and viscosity of the gas respectively at room temperature[102]. The time taken to fill the fibre to the pressure of 1 mbar ($\eta \sim 9.43 \times 10^{-6}$ Pa s) is $\sim$10 min.

6.3 Data Collection & their interpretation

The best way to test the quality of the fibre acetylene cell was by implementing it into NPL's experimental setup and comparing the data with their acetylene cell (50 Torr Gas Cell). Figure 6.7 shows a schematic of our collaborator's experimental setup along with fibre gas cell and the 20 Torr gas cell.

The laser was scanned along the R and P branch of acetylene at a rate of 300 nm/s, for different pressure values (and fibre lengths) of the fibre cell,

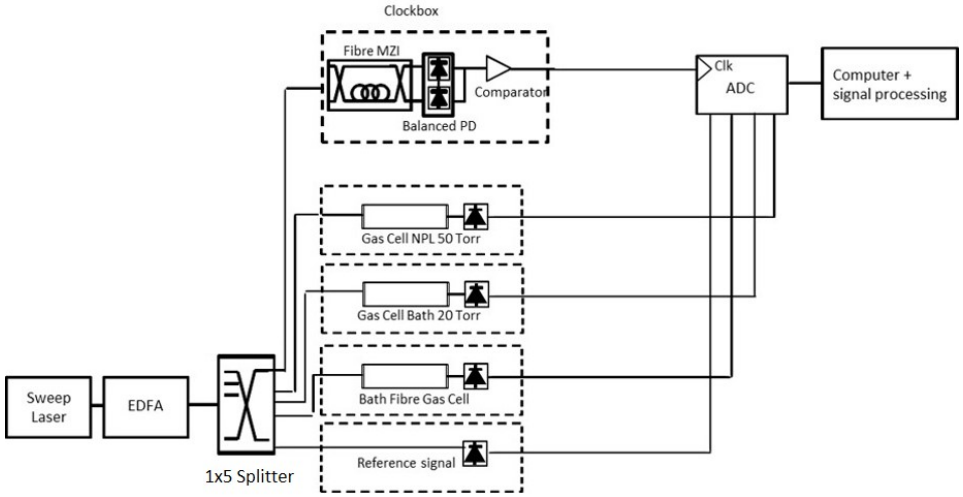

Figure 6.7 NPL's experimental setup (designed by Michael Campbell) along with the fibre and 20 Torr gas cells. The laser was scanned along the R and P branch of acetylene with different pressure values for the fibre gas cell. The 3 gas cells were measured simultaneously.

and the three gas cells were measured simultaneously. In order to linearise the tuning rate of the laser, a reference Mach Zehnder interferometer (labelled as fibre MZI on figure 6.7) was used to generate a clock signal with equal laser frequency spacing, rather than equal time spacing. The reference interferometer is ∼43 m in length with dispersion compensation. The reference interferometer essentially works as a clock for collecting the measurement data as the laser does not tune linearly in time. As shown in figure 6.7 the interference pattern was used as a clock signal input in the ADCs for the measurement data. When the interference pattern crosses the zero on the upsweep, it uses this as the point to sample the measurement data.

For the NPL's FSI system, the relationship between distance and frequency is given by equation 2.8. The frequency of the clock signal also follows equation 2.8 as it is the same process. Therefore the frequency of the clock signal is determined by the length of the reference interferometer and the tuning rate of the laser. It is worth mentioning that this process is constrained by the Nyquist sampling theorem, therefore the frequency of the sampling needs to be at least twice the frequency of the maximum measurement distance.

In Chapter 2.3.2 the importance of the gas cell in NPL's FSI system was highlighted as it can determine the tuning rate of the laser, α. The reference interferometer is used as a clock to sample the measurement signal, sampling with constant change in frequency, as the laser sweeps. The tuning rate of the laser also needs to be determined, although now it needs to be determined in terms of change in frequency with sample, instead of change in frequency with time. Therefore the gas cell is sampled with the same clock. From the absorption peaks it is possible to extract the frequency of the laser at certain samples and thus determine the rate of tuning of the laser with sample.

When the fibre gas cell was implemented into NPL's system, 50 scans were taken for each measurement. A reference signal was also recorded for each set of measurements in order to remove the background. The data was then aligned and averaged over the 50 scans to remove noise - this is a standard procedure that the NPL follows as the trigger of their system seems to be slightly inconsistent. Figure 6.8a) shows all the fibre and 20 Torr spectra collected after removing the background. From the graph it can be seen that there are still some fluctuations in the background, on the slow and fast scales, of both the fibre and cell data. Figure 6.8b) shows the fibre spectra with the background subtracted from figure 6.8a) but only the spectra with sensible line strength for all lines. A combination of pressure and length can result into saturation of the peaks or not enough signal to see the peaks. The pressure was varied between 0.1 mbar and 1.15 mbar for 2 and 1.5 meters of fibre (1.0 Torr = 1.3 mbar = 0.132 kPa).

The next step was to fit a Gaussian or a Lorentzian lineshape for the fibre and cells spectra. Figure 6.9 shows 3 absorption lines with their fits for line R9, where a) is taken from the fibre cell spectrum, b) is taken from the 20 Torr cell spectrum and c) is taken from the 50 Torr cell spectrum. As it can be seen from the plots, the fits are reasonable for a)&c) with a Gaussian and Lorentzian fit respectively, whereas b) is a Voigt profile. When a Gaussian

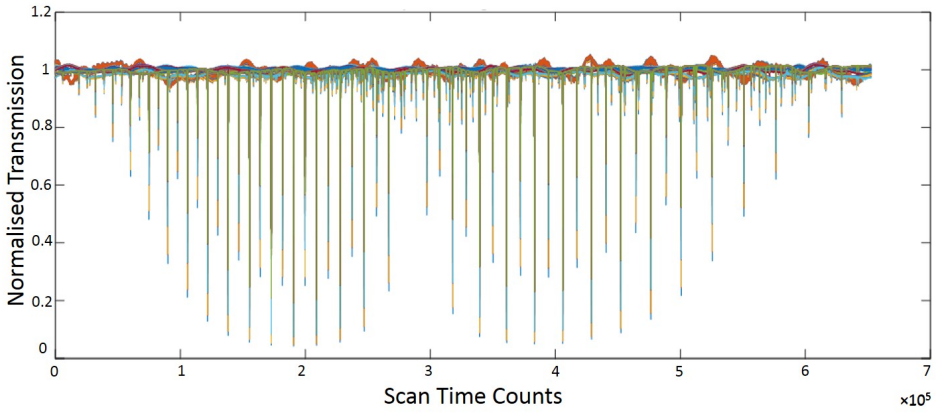

(a)

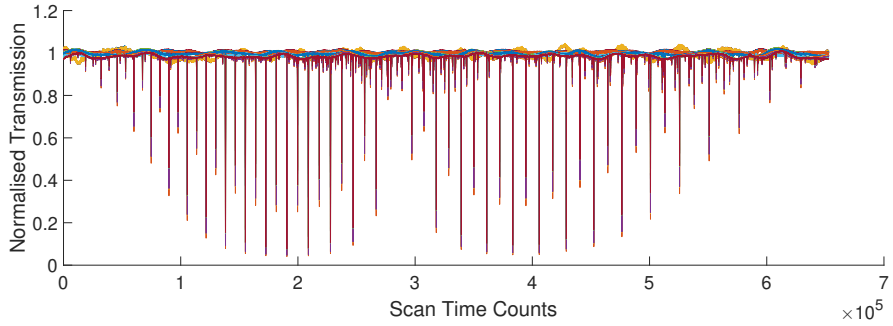

(b)

Figure 6.8 a) All the spectra from the fibre and 20 Torr gas cells for the R and P branch of acetylene b) Selection of fibre spectral lines from figure 6.8a with sensible line strength for both branches.

lineshape can be fitted to the data it means that the dominant mechanism is Doppler broadening whereas for a Lorentzian fit the dominant mechanism is pressure broadening. This is the first indication that the fibre gas cell provides more accurate measurements with less pressure shift. Furthuremore, a Gaussian lineshape is simple function that can be fit fast and well to the data. This can be very useful when using an FSI system (collaborator's

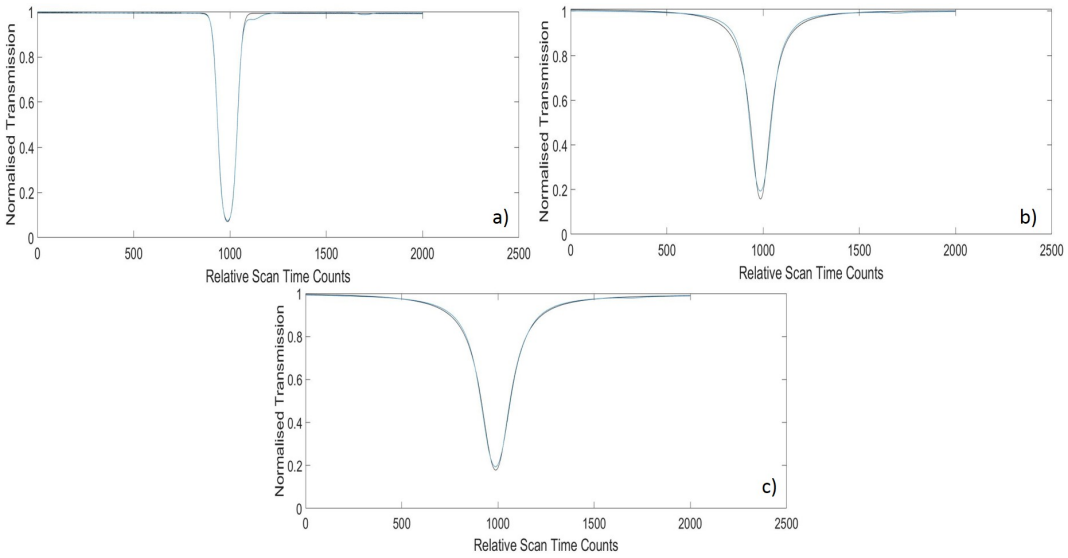

Figure 6.9 Analysis of line $R9$: a) Fibre spectrum and fit for one spectral run, b) spectrum from the 20 Torr cell and fit for one spectral run and c) spectrum from the 50 Torr cell and fit for one spectral run.

application) that scans over the entire range of acetylene and requires a system that can provide position (in frequency) accuracy at all times.

The final comparison from this investigation was the difference between line centre shifts of the fibre, the 20 and 50 Torr cells. Figure 6.10 shows the comparison in frequency difference between a) the fibre and the 20 Torr cells, b) the fibre and the 50 Torr cells and c) the 20 and 50 Torr cells. The shift is given in time counts which can be used to extract the shift in frequency (corresponds to ∼7 MHz per tick). Figure 6.10a)&b) show a measurable shift between the fibre and reference cells. The anomalies observed in the plots (at R18, P1, P18 and P19) are a result of having another absorption peak nearby

(not a result of pressure shift) and the anomalies are present in all the plots. This feature is also present in figure 6.9. In plot 6.9a) a secondary peak can be seen near the right tail of the main absorption peak. At low pressures it is therefore possible to separate the two neighbouring peaks, though in plots 6.9b)&c), where the pressure is much higher, the peaks (and therefore the profile fitting) are affected by it. This means that the peak position for plot 6.9a) can be established with higher accuracy compared to the other two plots, not just due to the lower pressure shift but also due to the anomalies present in the measurement. The feature shown on figure 6.9, which only shows the analysis for peak $R9$, was observed in multiple peaks along the tuning range.

The shift for figure 6.10b) is bigger compared to the shift in figure 6.10a) but the shape and anomalies are all the same. The data at the edges of the plots correspond to very weak lines and the analysis cannot provide an accurate fit. Figure 6.10c) does not contain any information about the fibre gas cells but it confirms that using lower pressure inside a gas cell has an effect on the shift of the line centre. It can be seen that the relative change in frequency between the fibre gas cell and the 20 Torr glass gas cell (Figure 6.10a) is lower compared to the relative change in frequency between the fibre gas cell and the 50 Torr glass gas cell (Figure 6.10b). This set of plots opens a new

investigation: how much better can we establish the peak positions by using a low-pressure fibre gas cell compared to a conventional gas cell. Furthuremore, can the true positions of the peaks be established when using a fibre gas cell since the pressure shift (and broadening) is minimised.

Multiple recordings were made in order to generate the plots shown in Chapter 6.3 which involves a combination of different pressures inside the cell (0.1 mbar - 1.15 mbar) and different cell lengths (1.5m & 2m). It is however very important to test the repeatability of these measurements. Effects such as a change in temperature or humidity might affect the measurements and therefore a calibration procedure may be required to compensate for these environmental effects. Furthuremore, a slight change in the amount of pressure inside the gas cell will affect the measurements, as well as a leak. When the measurements shown in figure 6.10 were taken, the length and pressure of the cell was constantly varied. To change the length, the gas cell had to be emptied completely and then re-filled. The whole process (including the measurements) took place in a laboratory with no temperature and humidity control for $\sim$5 hours . The peaks at the edges of the plots that involve the gas cell (see figure 6.10a&b) appear to have a large variation compared to the more central peaks. For example, for peak $R28$, the yellow and blue lines correspond to very low pressure values. For an FSI system it is

very important to know the two edges of the scan so this effect must be taken into consideration when implementing the gas cell in such systems. At higher pressures the shift of peak $R28$, on figure 6.10a, is at -25MHz $\pm$ 5MHz. On the same plot, the more central peaks, such as from $R2$ to $R18$, overlap for most of the combinations of pressure and length of the gas cell to $\geq$ 1 MHz. This observation suggests that the pressure inside the gas cell is well known and well maintained despite the fact that the work took place in an uncontrolled environment.

From literature it was found that Gilbert *et al* and Edwards *et al* attempted to define the pressure shifts and centres of acetylene peaks with high precision[45,103]. Edwards *et al* presented a system that can measure the centre of acetylene peaks with a much higher accuracy ($\sim$10KHz) than what is required for our system ($\sim$100KHz). Their system however cannot be implemented in an FSI. Gilbert *et al* have defined the pressure shifts with high accuracy for part of the acetylene spectrum. They have also provided measurements for centre lines with a $\sim$40MHz uncertainty. Our measurements suggest that it could be possible to provide a higher precision of pressure shift for the acetylene peaks compared to the precision provided by literature[45] and the experimental setup shown in Chapter 6 can

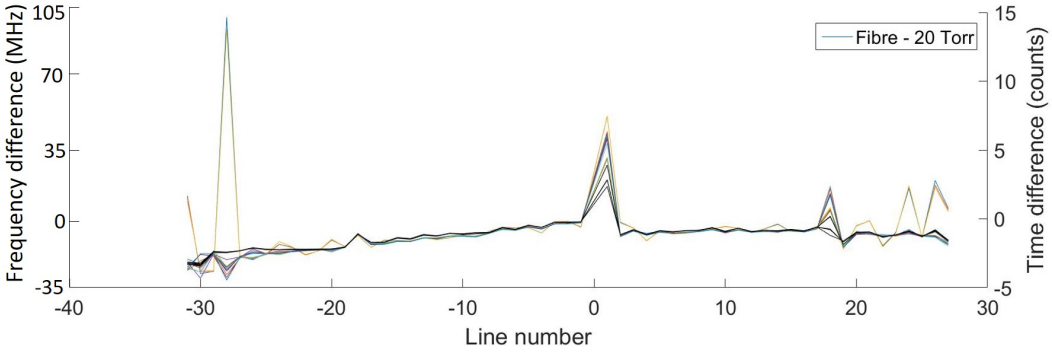

(a)

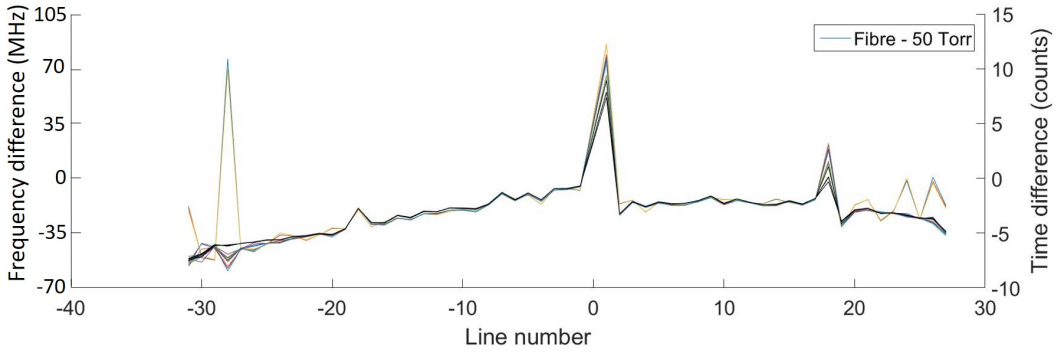

(b)

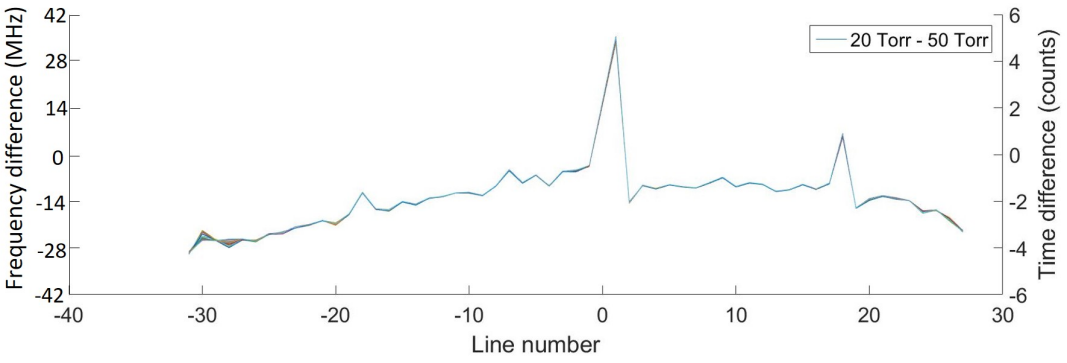

(c)

Figure 6.10 Comparison of frequency shifts for each line centre (also shown in time counts - ∼7MHz per tick) between: a) all fibre traces and 20 Torr cell, b) all fibre traces and 50 Torr cell and c) 20 Torr and 50 Torr cells (1.0 Torr = 1.3 mbar = 0.132 kPa).

be implemented in an FSI system.

6.4 Advantages of implementing the fibre gas cell into NPL's FSI system

In Chapter 2.3.2 the basic principles of frequency scanning interferometer were described. When measuring an absolute distance between a sensor and a target (see figure 2.6) a signal can be generated, the beat frequency signal that is proportional to the absolute distance measured. The beat frequency then needs to be analysed in order to provide a distance value. This is achieved by using the tuning rate of the operating laser (scale factor). When a distance measurement is provided, the two sources of uncertainty arise from the uncertainty in determining the beat frequency and the tuning rate of the operating laser. To calculate the tuning rate a gas cell can be used - it is important to choose a gas that exhibits absorption peaks across the entire tuning range. Extracting the line centre of each one of those peaks can help provide the tuning rate with higher accuracy. NPL calibrates each peak using literature i.e. NIST's calibrated frequencies[40,45].

Determining the line centre of each absorption peak is not an easy task as there are multiple sources of errors. Temperature and pressure have a

negative effect on the peaks as they cause broadening and they also cause a shift in frequency. These are the main sources of uncertainties with pressure being the dominant factor. It is therefore essential to reduce the pressure inside the gas cell for higher accuracy data (tuning rate scale factor depends on this measurement).

Another significant advantage of reducing the pressure in the gas cell is the efficiency and accuracy in fitting a profile to each absorption peak. From the profile, the line centre of each peak can be extracted. For the analysis of the fibre gas cell in Chapter 6.3 all the lines were measured and a profile was fitted to all of them. An example was shown in figure 6.9 where one peak was characterised under three different pressure values. It was therefore shown how a reduced pressure follows a simple Gaussian profile which provides an accurate fit and it is less computationally intensive compared to a Lorentzian or a Voigt profile.

Furthuremore, an effect described as anomalies was discussed in Chapter 6.3. Unfortunately sometimes neighbouring peaks can contaminate each other if they overlap due to collision broadening. Reducing the pressure can reduce how broad the lines are which will reduce the number of anomalies across the range and at the same time reduce the line centre uncertainties. From the

investigation in Chapter 6.3, multiple scans were taken for different pressure values in the fibre gas cell. It was found that at lower pressures such as 0.03 kPa, the linewidths are much smaller and the number of anomalies was significantly reduced compared to higher pressures. It was estimated that the pressure shift coefficient uncertainty for peaks affected by anomalies was 7 times higher that unaffected peaks. Therefore the advantage of reducing the pressure in this case is that that more lines can be separated so that more lines with lower uncertainties can be used to determine the tuning range.

A practical advantage of using a hollow core fibre gas cell over a glass tube is the flexibility in the experimental arrangement. A longer gas cell can be very beneficial as the depth of each absorption peak can be increased by extending the length of the gas cell. This improves the quality of the fitted profiles, especially when dealing with low pressure inside gas cells. Therefore it is practically beneficial to use a fibre gas cell as you can easily adjust its length whilst occupying a very small space in the experimental set-up instead of having a bulky glass gas cell. It is worth mentioning that hollow core fibres have a high bend loss therefore the radius of the loop (or the spool) should be long enough so that the bend loss cannot interfere with the data.

The following analysis was done by Dr. Micahel Campbell from the National

Physical Laboratory (NPL): He used the NIST calibrate data to simulate different pressures from which the scale factor can be calculated whilst assuming that there were no associated error to the fitting profile of each absorption peak[45]. The NIST line centre uncertainties and pressure shift uncertainties were used to simulate scale factors and associated uncertainty for various pressure values. Figure 6.11 shows the scale factor uncertainty as a function of pressure. As the pressure is reduced, the uncertainty in the scale factor decreases until ∼0.1 kPa where further pressure reduction has little benefit and the pressure independent uncertainties might begin to dominate. The experiments that have been carried out and described in Chapter 6.3 used gas pressures as low as 0.03 kPa showing that such measurements are feasible (1.0 Torr = 1.3 mbar = 0.132 kPa).

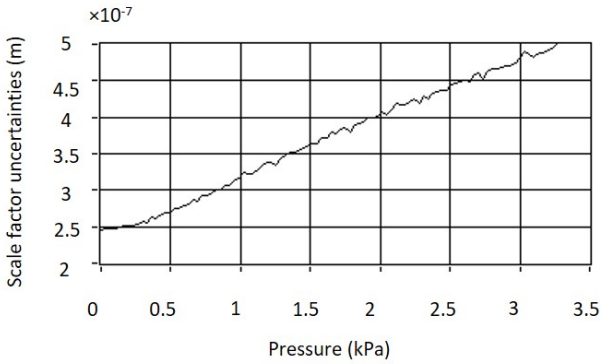

Figure 6.11 Scale factor uncertainty as a function of pressure. Line centre uncertainties and pressure shift uncertainties from NIST were used to simulate scale factors and associated uncertainty for different pressure values. Analysis done by Dr. Michael Campbell from NPL.

Therefore, if the pressure dependent pressure shift term is minimised, leaving the line centre uncertainty as the dominant uncertainty term, the scale factor uncertainty remains at ∼0.25 ppm, which agrees with the result that for less than 0.1 kPa the pressure dependent term is negligible.

The results gathered from this investigation show that our system can indeed provide a high accuracy for the central positions of the acetylene peaks. Therefore, the next step was to convert this experimental setup into an all-fibre gas cell device. In this case, back-reflections were a problem. The fibre spectra data shown in figure 6.8b) show that there are indeed some back-reflections in the system but they did not affect the quality of the measurement. When building the AMS interferometer, back-reflections were also a big concern as multiple parasitic interferometers were observed. The issue was eliminated by making all the fibre interfaces angled. Similar techniques were investigated in the following sections of this Chapter.

6.5 Tapers

One of the main challenges of developing a fibre gas cell was to couple light (with high efficiency) into a hollow core fibre. The fact that the fibre gas cell needs to be sealed from the atmosphere raises the difficulty of this task. The plan was that by the end of this set of experiments the gas cell would be a

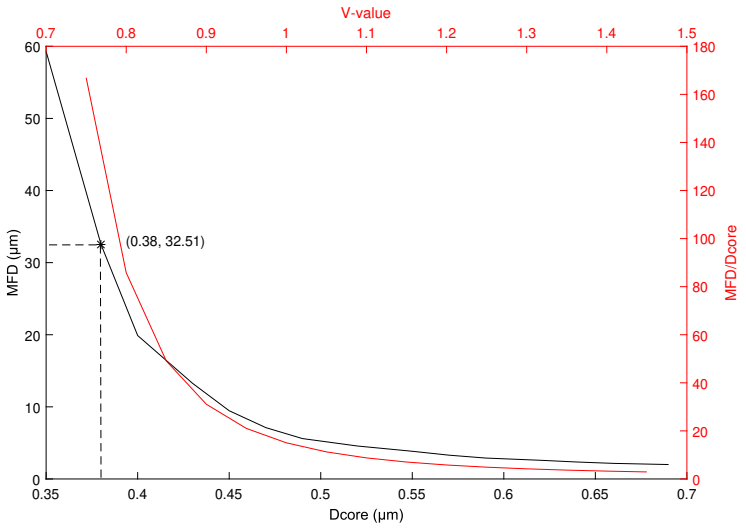

Figure 6.12 Simulations provided in order to determine optimal taper diameter. The data (black) show the Mode Field Diameter (MFD) plotted over the core diameter (D_{core}) and the V-value plotted over the MFD as a fraction of the core diameter.

portable all-fibre device. In the previous section, light was coupled into the hollow core fibre using a lens from a free space beam, though the coupling efficiency was only ∼30%. Furthermore, it was essential that back-reflections had to be minimized. High coupling efficiency was also beneficial as the allowed maximum pressure was very low (as discussed Chapter 6.2). Back-reflection can be created when there is a change of the refractive index in the propagation medium i.e. when beam of light in free space (with n_1) is coupled into an optical fibre (with n_2) and $n_1 \neq n_2$.

The idea proposed here involved tapering an SMF-28 and inserting it into the hollow core fibre that was previously designed. Tapering a fibre so that

the mode is much larger than the taper means that the mode will interact with less amount of silica and therefore the back-reflections will be less compared to the back-reflections that are generated when the beam leaves a fibre with a size of a few hundred microns. Due to the large mode field diameter mismatch, between the hollow core and the SMF-28 taper, it was expected that the device will be very lossy but minimizing back-reflections was considered a bigger concern. From literature it was found that other research groups have tried to couple light into a hollow core e.g. using a high power laser to align a taper to the core of a hollow fibre using the optical tweezers effect [104]. Most of the other high efficiency coupling papers involve free-space and high power and are not focussed on back-reflection [105,106].

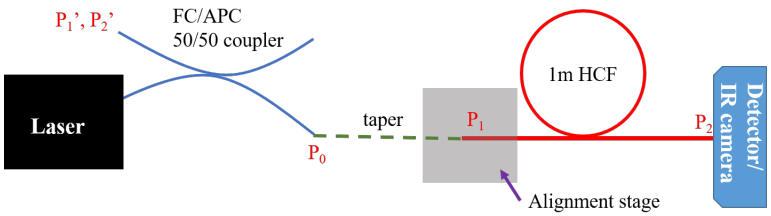

Figure 6.13 Experimental setup for measuring throughput and back-reflections when inserting a taper into a hollow core fibre.

Professor Birks (member of the CPPM group), provided a series of computational results for the mode field diameter (MFD) of a silica core in air, as shown in figure 6.12. The graph contains a plot of the MFD as the core diameter varies (black line) and the V-value plotted over MFD as a

fraction of the core diameter (red line). His model assumed that λ=1550 nm and n_{silica}=1.44402. He generalised equation(3) from *Artiglia et al* to use intensity defined by Poynting's vector[107]. He also calculated the mode field diameter as a fraction of core diameter for a cylindrical ideal-mirror waveguide (mimicking a hollow core fibre) to be 0.66. The core diameter of the 6-ring hollow core fibre was 46 µm (0.66×46=30.36 µm). Therefore the closest mode field diameter data point from figure 6.12 is 32.51 µm. Thus, the diameter of the taper must be ∼0.38 µm in order to maximize mode matching and therefore coupling efficiency. At this point it is worth mentioning that since the taper is inserted into the hollow core fibre the mechanism involved in this process is not coupling but excitation. Therefore if the mode field diameter of the taper is bigger than 32.51 µm the modes will still be excited. If light was coupled into the hollow core fibre from the taper then the size of the taper needs to be very accurate in order to maximize coupling efficiency. As can be seen from figure 6.12 (black), the mode field diameter (MFD) varies rapidly as the size of the core changes. Figure 6.13 shows a schematic representation of the experimental design. The work took place inside the Taper-rig lab of the CPPM group and credit needs to be given to Dr. Yerolatsitis for making the tapers that were tested in this set-up. The laser was set to 1550 nm with 8 mW output power and a 50/50 angle polished coupler was used to couple light into a piece of SMF-28 with an angled

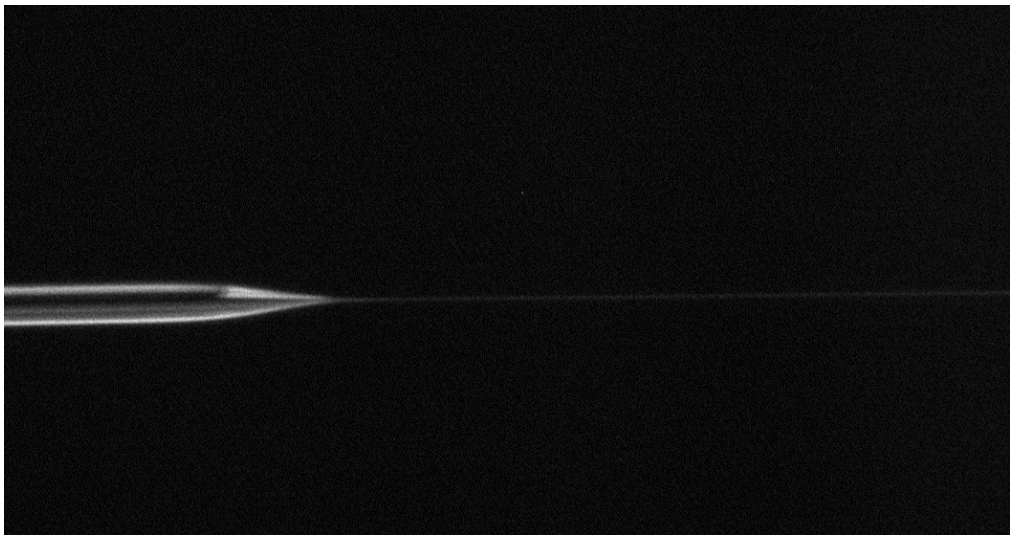

Figure 6.14 Image taken whilst tapering a single mode fibre down to a point.

polished end. The other end of the fibre was tapered down to size and then carefully placed on the alignment stage (Throlabs - NanoMax). As shown in the figure 6.13, one end of the hollow core fibre was placed on the same stage in order to couple light into it. The taper was carefully inserted into the hollow core fibre using the 3 alignment axis of the stage. Throughout the experiment, the power was monitored at P_0 (sanity check that power from the laser was constant and thus P_0=4 mW), P_1 (power at the end of the taper), P_2 (power at the far end of the hollow core), P'_1 (back-reflections once the taper is inserted in the system) and P'_2 (back-reflections once the hollow core fibre is inserted in the system). The detector that was used was an ANDO AQ2140 (optical multimeter) with two identical heads - one constantly monitoring the back reflections and the other the forward power.

The first taper design is shown in Figure 6.14. The taper was made by manually moving one of the stages away with constant speed. The outer diameter of the SMF-28 is 125 µm and the fibre was tapered down until it broke. From literature it was shown that when the V value, given by:

$$V = \frac{\pi d NA}{\lambda} \tag{6.3}$$

where d and NA are the diameter and the Numerical Aperture of the fibre respectively, is lower than 0.6, the core is not a good waveguide anymore. For a V<0.6 (and NA=0.11) the diameter of the fibre d must be less than 1 µm to affect its guiding properties. The taper was placed under the microscope and though its actual size was not determined, it was definitely less than 1 µm. This suggests that the light in this tapered fibre cannot be trapped in the core and it will spread out. Thus the light will interact with a small amount of silica (when leaving the taper) which will reduce back-reflections. The power at the end of the taper was 1.30 mW and the back-reflections were low, 112 nW. The next step was to place the taper in the hollow core fibre and measure the powers. Due to the small size of the taper it was impossible to manually align it by eye. Therefore, the alignment stage was placed under a microscope, which made the process much easier and the optical head that was measuring the forward power was temporarily replaced by an IR camera

in order to confirm that the light is indeed coupled in the core of the fibre. Though the power at the end of the taper was very high, the power at the far end of the hollow core was very low (500 nW). This was justified by the fact that the taper transition was not adiabatic - the transition was very rapid. This means that the light was not kept in the fundamental mode during the transition. Instead the light was coupled into high order modes. Therefore, when coupling into the hollow core fibre the taper has a very high NA and the light will diverge fast, making it impossible to get trapped in the hollow core efficiently.

For the next taper design, the aim was to make the transition adiabatic. A LabVIEW software was used to make the taper and the fibre was tapered down to 0.3 µm with a 30 mm transition. The power at the end of the taper was 2.6 mW and the back-reflections were 130 nW. A similar procedure was followed in order to place the taper in the hollow core. However, as the length of this very thin taper was so long it was extremely difficult to control and it seemed to stick on one side of the hollow core. Using an anti-static air blow off gun caused the taper to entangle itself. Therefore, it became apparent that this taper design was definitely not ideal. The maximum power at the far end of the hollow core was 5 µW with 120 nW back-reflections. Even if the measured powers seem slightly better that the

first design, the design itself was not ideal and its durability was low.

A third and final design was made and is shown in Figure 6.15. The aim was to design a taper that will be adiabatic, be easy to use (inspired by the first design) and have high output power (inspired by the second design). Therefore, a multi-step taper design was made with adiabatic transitions and with good mechanical properties. The power at end of the taper and the back-reflections were 3.1 mW and 90 nW respectively. When placed in the hollow core, the power readings were 1 mW and 90 nW. This was definitely the best taper design as it combined good mechanical properties and high throughput. The back-reflections unfortunately still remain a problem (-42.7dB) but nevertheless it was considered a good attempt.

The small diameter of the taper was probably the biggest challenge in this experiment. From figure 6.12 it can be seen that the mode field diameter (MFD) varies rapidly as the core size changes. A taper with bigger diameter than the desired size can have a negative impact on the coupling efficiency of the design. At the same time, some of the equipment used for the experimental set up was not ideal. For example, a better technique needs to be used when placing the taper in the hollow core. Using the microscope in order to see the transverse side of the two fibres and couple one into the

other was effective. However, it was impossible to see whether or not any of the two cross sectional areas were damaged during the process and whether or not the taper was actually inserted in the core rather than the cladding. Furthermore, a smaller flame size (obtained by a smaller burner needle) would have allowed smaller changes of the taper per unit length. A smaller flame would have also increased the accuracy of the desired taper diameter. For these reasons the experimental work on the taper rig was stopped and a final attempt to reduce back-reflections is described in the next section.

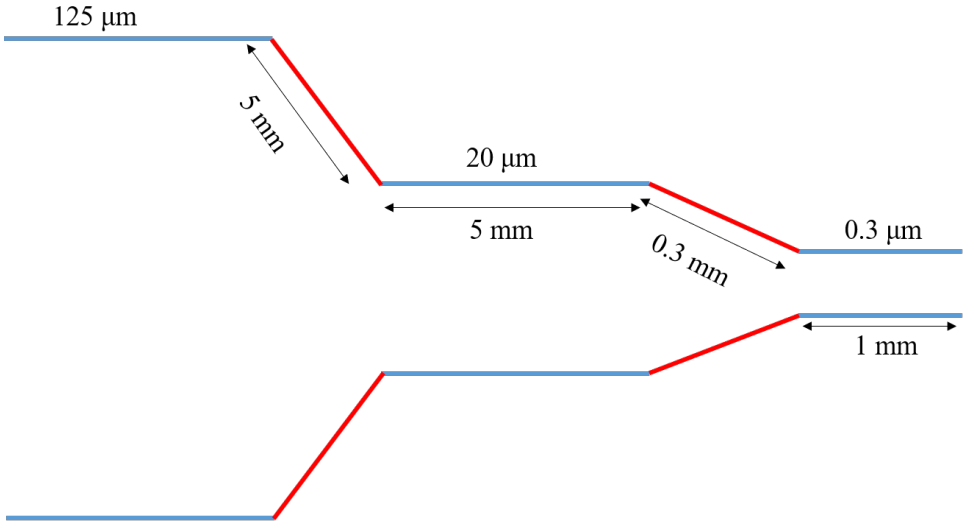

Figure 6.15 Multi-step taper design with adiabatic transitions.

6.6 Back-reflection investigation measurements

As shown in the previous section, a taper can give -42dB back reflection noise. A final attempt to reduce the back-reflections even more was made and

the experimental set-up is shown in Figure 6.16. The figure shows a similar set-up to the one that was used for testing the back-reflections of the tapers. The difference here is that a single mode fibre was used to couple light in and out of the hollow core. In the first set-up, the SMF has flat ends - FC/PC, therefore one expects higher back-reflections and higher throughput. In the second case, the SMF has angled polished ends - FC/APC. This suggests that the back-reflections can be much lower (referring back to the back-reflection issues that were found in the interferometer - Chapter 4.5.3) and potentially lower throughput as the 8° angle of the FC/APC can cause coupling issues. The positions where forward power was measured are marked as P_0, P_1, P_2 and P_3) as well as the back-reflection that corresponds to each experimental configuration (P'_0, P'_1, P'_2 and P'_3).

The results are shown in Table 6.2:

Table 6.1 Throughput and back reflection measurements for the flat and angled configurations.

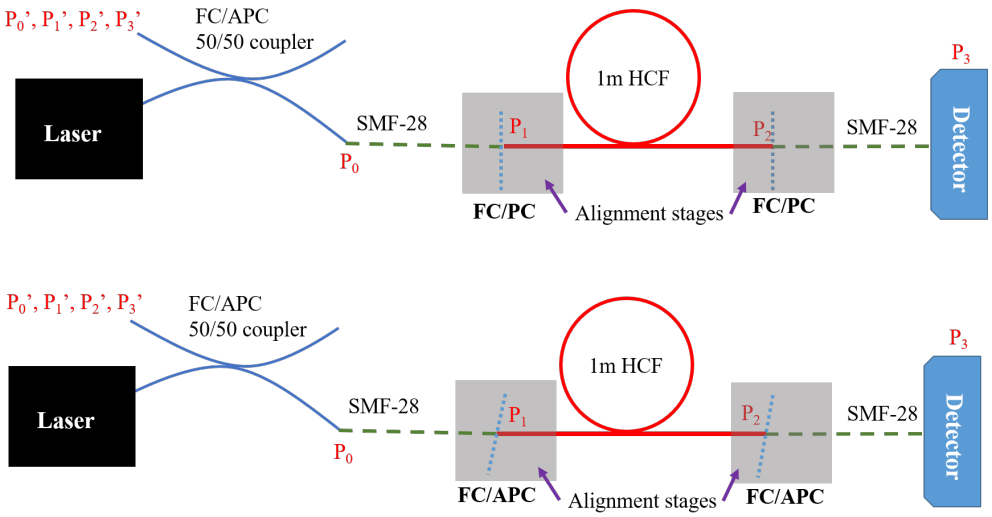

Figure 6.16 Experimental set-up(s) for further investigation of back-reflections. The difference between top and bottom is that a flat (FC/PC) and angled (FC/APC) polished single mode fibre respectively, was used to couple light in and out of the hollow core fibre. The back-reflections and forward power were recorded at each step.

	FC/PC	FC/APC
P_0	4.24 mW	4.24 mW
P'_0	488 pW	488 pW
P_1	4.24 mW	4.24 mW
P'_1	37 µW	488 pW
P_2	1.05 mW	1.02 mW
P'_2	37 µW	488 pW
P_3	436 µW	400 µW
P'_3	37 µW	488 pW

From table 6.2 it can be seen that the forward powers in both setups are roughly the same, with the "flat" configuration being slightly higher. However, looking at the back-reflections the "angled" configuration shows that the detector was unable to pick any signal (488 pW is the offset of the detector) and the back-reflection at the end of the hollow core were calculated to be less than -66.3 dB. The measurements provided for FC/PC show that the back-reflections are too high (-8.28 dB - the third taper design gave -42.70 dB) and even if the forward power is slightly higher it suggests that this configuration should not be implemented in the gas cell. The experiment was repeated a few times and the results were consistent. Therefore it was shown that the best configuration of the three possible cases (tapers, FC/PC and FC/APC) that combines both high coupling efficiency and low back-reflections is the angled fibre configuration.

The final part of this investigation was to interpret the data and extract information about the hollow core fibre. The data must satisfy one of the three equations:

$$P_1 = P_2 \qquad (P_2 > P_3), \tag{6.4}$$

$$\frac{P_2}{P_1} = \frac{P_3}{P_2}, \tag{6.5}$$

and

$$P_2 = P_3 \qquad (P_2 < P_1). \tag{6.6}$$

If the data satisfy equation 6.4, i.e. the power at the end of the first SMF-28 is equal to the power at the end of the hollow core, this suggests that the hollow core is a multi-mode fibre and can collect all light/modes. If the second expression is true (equation 6.5), i.e. the ratios of output powers over input powers are equal, it is suggested that the three fibres involved can only guide one mode. If equation 6.6 is correct, i.e. the power at the end of the hollow core is equal to the power at the end of the second SMF-28, then the hollow core is assumed to be single-mode and the SMF-28 a multi-mode fibre. The latest expression is definitely wrong as the SMF-28 is single mode at 1500 nm. Using the data from Table 6.2 it can be seen that equations 6.4 and 6.6 cannot be satisfied, whereas equation 6.5 is close to being true which suggests that the hollow core that was fabricated for this experiment is slightly-multi-moded.

6.7 Implementing the FC/APC fibres in the fibre gas cell

In the previous section it was shown that the back-reflections can be easily minimized when the fibres at the input and output of the hollow core are angled cleaved. However, implementing this solution into a fibre cell is not trivial.

Even though the set-up shown in figure 6.5 satisfies our collaborators needs,

it has room for improvement. Ideally the glass windows should be removed, as they are one of the main source of back-reflections. Furthuremore, making this device portable would make it easier to use and store as the rest of the measurement system used by the collaborators is placed in a 19-inch rack. Having an acetylene vessel in a working environment involves health and safety precautions that are also inconvenient. The idea that was proposed was to insert the hollow core fibre along with an angled cleaved SMF-28 (at each end) in a capillary, 4 cm-5 cm long, and provided that the fit is very tight the cores of the two fibres will be aligned. The SMF-28 has an outer diameter of 125 µm and the core size is 10 µm whereas the hollow core fibre used for all the experiments so far has an outer diameter of 160 µm and a core size of 46 µm. Based on these dimensions a tight fit for both fibres cannot be achieved unless the capillary has a more complicated design.

Based on the equipment available it was decided to slightly simplify the set-up as Dr.Rusimova provided a capillary with an inner diameter of 126 µm and a 6-ring hollow core fibre that had been fabricated in the past which can guide light at 1550 nm (see figure 6.17). The dimensions of this new hollow core is 125 µm for the outer diameter and 24 µm core size. Though the transmission band of this fibre at 1550 nm is not as low as the 6-ring hollow core fibre shown in figure 6.2&6.3, it was still interesting to test that a very

tight fit in a capillary can "replace" an alignment stage and provide high coupling efficiency.

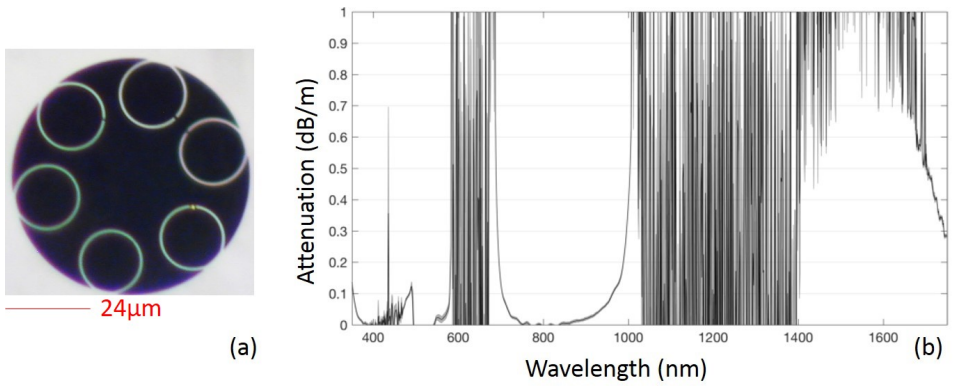

Figure 6.17 (a) Microscope image & (b) attenuation graph of the 6-ring hollow core that was inserted in the capillary. There is no transmission between 590 nm and 670 nm and between 1110 nm and 1390 nm for this design

The SMF-28 (on both sides of the hollow core fibre) was angled cleaved before placed in the capillary using an angled fibre cleaver (Newport FK12). As this hollow core fibre has never been used before for experiments in the mid-IR it was important to couple light into it (at 1550 nm) using the basic method i.e. place it on an alignment stage and couple light into it using an angled cleaved SMF-28. This essentially provided a reference that was helpful during the optimisation process of the alignment in the capillary. In other words we knew what the maximum coupling efficiency was. Setting the output power of the laser to 10 mW, and sending 90% of that to the hollow core fibre through the angled cleaved SMF-28, a total of 2.7 mW was

collected at the far end of the hollow core fibre i.e. ∼30% coupling efficiency.

Keeping the same laser settings and replacing the alignment stage with the capillary the power collected at the far end of the hollow core was 1.5 mW i.e. ∼17% coupling efficiency. It was found that even small movements of the positioning of the two fibres can affect the coupling therefore once the maximum value was reached the fibres were taped down. This suggests that the fit for at least one of the two fibres was not very tight. This was confirmed when the two fibres and the capillary involved in this experiment were looked under a microscope with a 50× lens. Figure 6.18 shows (a) the SMF-28, (b) the capillary and (c) the hollow core fibre. The two dotted lines drawn touch the edges of the capillary whereas for the two fibres there is a small space in between them (∼8 µm). This small space seems to be enough to cause issues with throughput of the experiment - cores (and mode field diameter) not well aligned for high efficiency coupling. The setup was completed by inserting the far end of the hollow core fibre into another capillary and couple light into another piece of angled cleaved SMF-28. The total power at the end of this device was 0.5 mW, i.e. ∼6% total coupling efficiency. In order to check for back-reflections the laser was set to scan from 1530 nm to 1550 nm with 2 nm per second scanning speed. A detector was used to send the signal to a digital oscilloscope (DSO-X 3032A). The traces

showed no fluctuations which means that the back-reflections were minimised (the back-reflections were lower than what the detector can see).

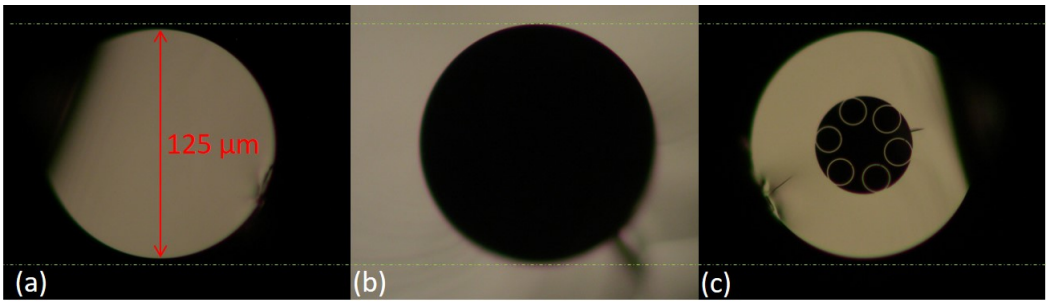

Figure 6.18 Microscope images using a 50× microscope objective. The images show: (a) An SMF-28, (b) the capillary and (c) the hollow core fibre.

Filling this device with acetylene was also considered a challenge for this experiment. Once the fibres are aligned the capillary needs to be sealed (using vacuum glue) and then filled with gas. For this, credit needs to be given to Adam Earthey (PhD member of the CPPM group of the University of Bath), who used a CO_2 laser (QCW operation at 10.6 µm) to create holes through the wall of the capillary (see Figure 6.19). Relying on the fact that the SMF-28 is angled cleaved and provided that the intercept point between the two fibres is very close to the hole, the hollow core fibre should be able to be filled with acetylene. The connection to the vacuum system will be made through a series of 1/8″ Swagelok tubes and T-pieces. Thus it has been shown based on these preliminary results that it is possible to minimize

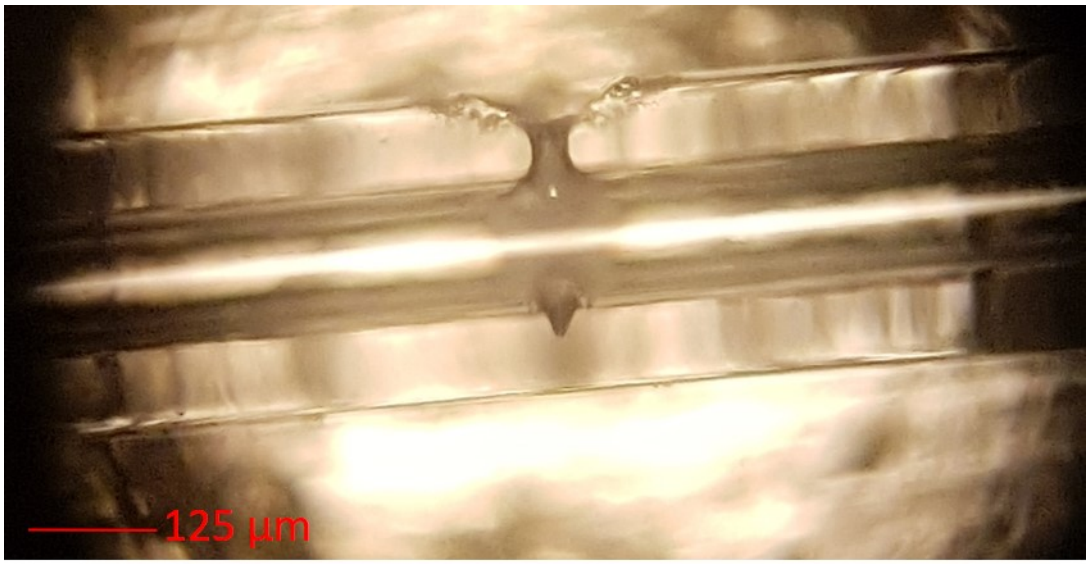

Figure 6.19 Microscope image of a capillary where a hole was burned through the wall using a CO_2 laser.

back-reflections in a fibre cell portable device. Further work would establish whether or not the absorption lines can be detected and analysed.

Chapter 7

Conclusions & Future Ambitions

7.1 Overall Performance

The focus of this research was to explore different parameters that affect the quality of a measurement. Three major systems were developed and their capabilities were explored: the AMS interferometer, the frequency stabilisation of a diode laser and using hollow core fibres filled with gas as reference gas cells.

For the AMS interferometer the focus was initially set on confirming with computational models, that the feedback from the system can be used to align the interferometer and that the power throughput is enough in order to

proceed to experimental testing. The computational models showed that the interferometric signals can provide information about the direction of the movement inside the interferometer (this can be done with the $I\&Q$ signals). This research along with an uncertainty budget for independent uncertainties for an AMS scale bar were published under the following article: "Absolute Multilateration between Spheres" [70].

Further experimental work on the interferometer showed that the polished steel spheres can be replaced by n=2 spheres as the power throughput will be higher which helps with the initial alignment. This does not change the interferometric arrangement, though an uncertainty budget for the n=2 spheres is now required.

The focus was then set on determining the stability of the AMS interferometer. Effects such as back-reflections, air flow and temperature fluctuations that can negatively affect the interferometric measurements were minimised. Laser frequency fluctuations also had to be eliminated. The laser used for this experiment was a cost effective solution, that was surprisingly stable ($\sim$ 30MHz) without any external feedbacks and it was successfully locked using a lock-in amplifier and a series of electronics. A better stabilisation system and laser could have been used but it would have made

the cost of the final system unaffordable. Having in mind that some applications would probably require multiple measurement systems, it is sensible to design a low-cost solution when building the first one.

Multiple recordings of the interferometric signals (and error signal) were collected that show the improvement in frequency stability (∼0.4 MHz) when the laser is frequency-locked. This is another major source of fluctuations of the interferometric signals that has been minimised.

The final investigation of this thesis involved the design and fabrication of a hollow core fibre to be used as a low pressure acetylene gas cell. A list of advantages of using a fibre gas cell over a commercial glass gas cell (such as reduced pressure shift and efficient and accurate peak profile fitting) can be found in Chapter 6.4. The fibre was successfully sealed and filled with acetylene gas. It was then implemented in an experimental setup that involved NPL's equipment and compared against two glass gas cells of much higher pressure. The main results showed that the difference in the shift of the peaks compared to the glass gas cell is significantly lower. Therefore when the final steps for completing the cell (i.e. place the hollow core fibre and the SMF-28 fibre inside a capillary and seal the device - see Chapter 6.7) are finalised the fibre gas cell will be introduced in NPL's FSI system. At the

same time, the fibre gas cell can be implemented in the experimental set-up of the laser stabilisation system that was used in Chapter 5.2. If the fit inside the capillary is not tight enough, which will affect the coupling efficiency between the two fibres, a more careful fabrication process may be required in order to optimise the diameter of the hollow core fibre and the diameter of the capillary. Furthuremore, a band with higher transmission at 1550 nm may also be useful.

7.2 Finalising the AMS scale bar

Earlier (Chapter 4) it was shown that significant alignment errors within the interferometer can be accommodated within the diverging beam and a combination of power and distance signals can then be used to self-align the interferometer. In order to finalise the scale bar a series of tasks must be completed. The interferometric path must be properly sealed to reduce thermal effects (as shown in figure 4.1). Furthermore, the interferometer assembly will be controlled in 4 DOF by placing the miniature optical components in a high precision positioner and make the entire system a portable device. Automated alignment of the interferometer is also an option. Once these tasks are completed, the scale bar can be implemented in any system in order to provide scale information for instrument verification.

It is expected that once the issues with Laser 2 (internally locked laser that was used for the beat frequency experiments) are resolved, the frequency stabilisation experiment will be repeated in order to acquire more information about the quality of the developed locking procedure. This will potentially reveal any unwanted fluctuations in the interferometric system that have not been eliminated yet.

In Chapter 5.1 the motivation behind the need to stabilise a fixed wavelength laser system was explained. Further computational analysis will be required in order to combine synthetic wavelength and phase measurements plots to develop an absolute distance measurement system. The Frequency Scanning Interferometry (FSI) technique, that was described earlier in Section 2.3.2, though it requires a complex operating laser (and therefore expensive) is able to provide measurements of arbitrary distances with a very high accuracy. Potential collaboration with research groups from NPL or University of Oxford could lead to implementing their FSI system into the scale bar. If the AMS network system would be able to provide measurements with a single laser, which will serve many interferometric bars, the accuracy of these measurements will be high whilst the cost will remain low.

7.3 Applications for the AMS scale bar

The main aim of this research was the development of a system that can provide accurate measurements for large scale structures. The AMS model can be used as a coordinate reference system for localised measurements. Networks of photogrammetry and laser tracker can be used for measurements of large scale structures. Since both methods are subject to environmental disturbances the provided uncertainty of such measurements in an uncontrolled environment will be negatively affected. If an AMS network can be built around the structure to be measured, photogrammetry and laser tracker can first reference the AMS network and then proceed to measuring nearby features of the structure. Therefore there will be a definite reduction in the uncertainty of each measurement [70].

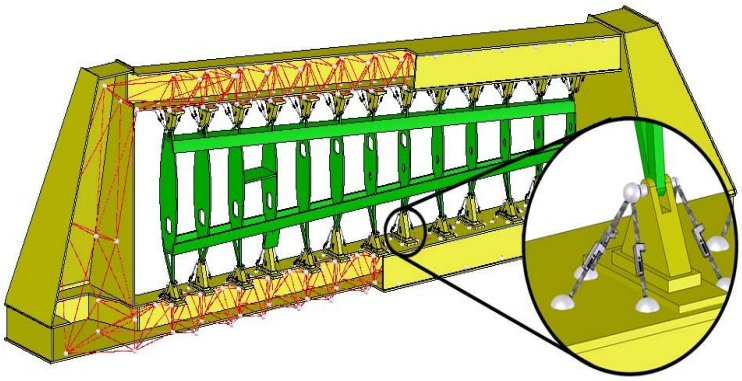

Figure 7.1 AMS embedded within a Wing Box Assembly Jig [70].

Another interesting application for the large scale coordinate reference

system that the AMS can provide, is by implementing this reference network in production tooling e.g. within large assembly jigs. By installing an AMS network within an assembly tooling, control of key interfaces of an aircraft wing box can be achieved (see Figure 7.1). This method can be used to obtain information regarding jig actuation such as compensation for thermal expansion of the assembly structure[70].

Appendix A

Appendix

A.1 Quadratue Analysis of the AMS interferometer

The field of the source can be written in vector form as:

$E = \left[\begin{smallmatrix} E_x \\ E_y \end{smallmatrix}\right]$

where E_x and E_y are the scalar components of $\vec{E}$. By normalising the intensity of the vertically polarised light, $E_x = 0$ and $E_y = 1$. Similarly the $\lambda/2$, $\lambda/4$, PBS_x and PBS_y are represented by:

$$\lambda/2 = \frac{1}{\sqrt{2}}\left[\begin{smallmatrix} -1 & 1 \\ 1 & 1 \end{smallmatrix}\right]$$

$$\lambda/4 = \frac{1}{\sqrt{2}}\left[\begin{smallmatrix} 1 & i \\ i & 1 \end{smallmatrix}\right]$$

$$PBS_x = \left[\begin{smallmatrix} 1 & 0 \\ 0 & 0 \end{smallmatrix}\right]$$

$PBS_y = \left[\begin{smallmatrix} 0 & 0 \\ 0 & 1 \end{smallmatrix}\right]$

where the $\lambda/2$ and $\lambda/4$ are at 22.5° and 45° respectively. At the output of the central PBS the electric field vector can be found by:

$$[PBS_y + PBS_x(\lambda/4)(\lambda/4)PBS_y(\lambda/4)(e^{i\phi})(\lambda/4)PBS_x] \text{ x } (\lambda/2)\left[\begin{smallmatrix} E_x \\ E_y \end{smallmatrix}\right] = \frac{1}{\sqrt{2}} \left[\begin{smallmatrix} e^{i\phi} \\ 1 \end{smallmatrix}\right]$$

The phase factor $e^{i\phi}$ accounts for the OPD of the interferometer. The recombined beam will will pass through a $\lambda/2$ and therefore:

$$(\lambda/2)\ \sqrt{2}\left[\begin{smallmatrix} e^{i\phi} \\ 1 \end{smallmatrix}\right] = \frac{1}{2}\left[\begin{smallmatrix} 1+e^{i\phi} \\ 1-e^{i\phi} \end{smallmatrix}\right]$$

The beam will then travel through a NPBS which contributes a $\frac{1}{\sqrt{2}}$. The transmitted beam will then reach a PBS so that:

$$PBS_y \frac{1}{\sqrt{2}} \frac{1}{2}\left[\begin{smallmatrix} 1+e^{i\phi} \\ 1-e^{i\phi} \end{smallmatrix}\right] = \frac{1}{2\sqrt{2}}\left[\begin{smallmatrix} 0 \\ 1-e^{i\phi} \end{smallmatrix}\right]$$

$$PBS_x \frac{1}{\sqrt{2}} \frac{1}{2}\left[\begin{smallmatrix} 1+e^{i\phi} \\ 1-e^{i\phi} \end{smallmatrix}\right] = \frac{1}{2\sqrt{2}}\left[\begin{smallmatrix} 1+e^{i\phi} \\ 0 \end{smallmatrix}\right]$$

So E_x can E_y be written as:

$$E_x = \frac{1}{2\sqrt{2}}(1 + e^{i\phi})$$

$$E_y = \frac{1}{2\sqrt{2}}(1 - e^{i\phi})$$

The intensity signal from E_x is represented as:

$$E_x E_x^* = [\frac{1}{2\sqrt{2}}(1 + e^{i\phi})][\frac{1}{2\sqrt{2}}(1 + e^{i\phi})]^*$$

which gives:

$$E_x E_x^* = \frac{1}{4}(1 + \cos(\phi))$$

And similarly for E_y:

$$E_y E_y^* = \frac{1}{4}(1 - \cos(\phi))$$

which is 180° out of phase with the previous signal (I,$\bar{I}$). Similarly the beam that reflects off teh NPBS will pass through a ($\lambda/4$) and then through a PBS:

$$PBS_y(\lambda/4)\frac{1}{\sqrt{2}}\frac{1}{2}\begin{bmatrix}1+e^{i\phi}\\1-e^{i\phi}\end{bmatrix} = \frac{1}{4}\begin{bmatrix}0\\i(1+e^{i\phi})-e^{i\phi}+1\end{bmatrix}$$

$$PBS_x(\lambda/4)\frac{1}{\sqrt{2}}\frac{1}{2}\begin{bmatrix}1+e^{i\phi}\\1-e^{i\phi}\end{bmatrix} = \frac{1}{4}\begin{bmatrix}i(1-e^{i\phi})+e^{i\phi}+1=\\0\end{bmatrix}$$

By factorising properly and using $i = e^{i\pi/2}$, E_x and E_y are found to be:

$$E_x = \tfrac{1}{4}(1+i)(1-e^{i(\phi+\frac{\pi}{2})})$$

$$E_y = \tfrac{1}{4}(1+i)(1+e^{i(\phi+\frac{\pi}{2})})$$

Therefore the intensity signal from E_x is represented as:

$$E_xE_x^*=\frac{1}{4}(1-\sin(\phi))$$

and E_y:

$$E_yE_y^*=\frac{1}{4}(1+\sin(\phi))$$

This pair is 180° out of phase with each other $(Q, \bar{Q})$ and at the same time, 90° out of phase with $(I, \bar{I})$. Therefore, we have proved that there are four quadrature signals generated from this interferometric design.

A.2 Gaussian Beam Model

```
restart : with(plots) : with(LinearAlgebra) :
local n, L1, l, L2, l, R, Rdet : n := 1 : λ := 1550·10^-6 :
# Rin and thetain to be determined
#L1 is the distance from source to BS
 #L is the distance between the 2 spheres CD.
 # l is the position of the BS relative to the second sphere
 # R is the radius of the sphere
 #Rdet is the radius of the detector
 # L2 is the distance from the BS (point E) to the detector
 #matrix m4 and m7 represent the intercept with the spheres i.e concave surface.
 # if convex you need −2 divided by R
m2 := Matrix(2, 2, [1, L1, 0, 1]) : m3 := Matrix(2, 2, [1, L-l, 0, 1]) :
m4 := Matrix(2, 2, [1, 0, 2/R, 1]) : m5 := Matrix(2, 2, [1, L, 0, 1]) :
m7 := Matrix(2, 2, [1, 0, 2/R, 1]) :
m8 := Matrix(2, 2, [1, l, 0, 1]) : m9 := Matrix(2, 2, [1, L2, 0, 1]) :
L1 := 10 : L := 1000 : l := 100 : L2 := 10 : R := 50 : Rdet := 0.05 :
prop := m9.m8.m7.m5.m4.m3.m2 : # multiply to get final propagation matrix
#assign values of ABCD matrix to Aa,Bb,Cc,Dd
Aa := prop(1) : Bb := prop(3) : Cc := prop(2) : Dd := prop(4) :
generate := proc(win, sign, powerfrom, powerto, step)
 local res, i, Rin, qin, q2, Req2, Imq2, Rout, wout, FracPower, z, zRin, AA, BB, CC, DD :
res := [ ] :
 for Rin from -10^powerfrom by step to -10^powerto do:
qin := evalf( 1 / (1/(sign·Rin) - I·λ/(π·win^2)) ) :
 q2 := (Aa·qin + Bb)/(Cc·qin + Dd) :
 Req2 := evalf(Re(1/q2)) :
 Imq2 := evalf(Im(1/q2)) :
Rout := 1/Req2 :
wout := sqrt(-λ/(n·π·Imq2)) :
 FracPower := 2·Rdet^2/wout^2 :
z := Re(qin) : zRin := Im(qin) :
  res := [res[ ], [z, FracPower, Rin, zRin, log(-sign·z)]] :
end do:
#plot(res[.., [3, 5]], style=point, labels=["Rin", "log(-z)"]);
plot(res[.., [1, 2]], style=point, labels=["z", "FracPower"]);
#plot(res[.., [3, 4]], style=point, labels=["Rin", "zRin"]);
#plot(res[.., [3, 2]], style=point, labels=["Rin", "FracPower"]);
 end proc:
```

#value to use for Rout
$RR := res[1, 6]$:
$$tt := \frac{\text{Rdet}}{\text{RR}} :$$
$\text{theta} := \arcsin(tt)$:
 # range in path errors drange
$drange := RR \cdot (1 - \cos(\text{theta}))$:

References

[1] O. C. Martin, J. E. Muelaner, Z. Wang, A. Kayani, D. Tomlinson, P. G. Maropoulos, and P. Helgasson, *Metrology enhanced tooling for aerospace (META): A live fixturing Wing Box assembly case study* (2011).

[2] *Light Controlled Factory – www.lightcontrolledfactory.com.*

[3] P. Maropoulos, P. Keogh, J. Knight, W. Wadsworth, J. Huntley, S. Robson, J. Muelaner, D. Ross-Pinnock, Z. Wang, A. Francis, H. Dantanarayana, L. MacDonald, J. Boehm, and S. Kyle, *The Light Controlled Factory*, Glasgow (2014).

[4] P. Maropoulos, P. Vichare, O. Martin, J. Muelaner, M. Summers, and A. Kayani, *Early design verification of complex assembly variability using a Hybrid – Model Based and Physical Testing – Methodology*, CIRP Annals - Manufacturing Technology, **60**, pp. 207–210 (2011).

[5] B. Muralikrishnan, D. S. Sawyer, C. J. Blackburn, S. D. Phillips, B. R. Borchardt, and W. T. Estler, *ASME B89.4.19 Performance Evaluation Tests and Geometric Misalignments in Laser Trackers — NIST*, Journal of Research of the National Institute of Standards and Technology (2009).

[6] CEN, *Geometrical Product Specifications (GPS) — Inspection by measurement of workpieces and measuring equipment Part 1: Decision rules for proving conformance or nonconformance with specifications ISO 14253-1* (1998).

[7] H. Schwenke and M. Wissman, *Measuring device WO/2012/010112* (2011).

[8] *ETALON AG - www.etalon-ag.com.*

[9] P. A. Coe, *An Investigation of Frequency Scanning Interferometry for the alignment of the ATLAS semiconductor tracker*, Ph.D. thesis, University of Oxford, Trinity Termt (2001).

[10] J. Muelaner and P. Maropoulos, *Large Volume Metrology Technologies for the Light Controlled Factory*, Procedia CIRP, **25**, pp. 169–176 (2014).

[11] D. Ross-Pinnock and P. G. Maropoulos, *Review of industrial temperature measurement technologies and research priorities for the thermal characterisation of the factories of the future*, Proceedings of the Institution of Mechanical Engineers, Part B: Journal of Engineering Manufacture, **230**, pp. 793–806 (2016).

[12] Z. Wang and P. Keogh, *Active Vibration Control for Robotic Machining*, in *Volume 2: Advanced Manufacturing*, p. V002T02A079, ASME (2017).

[13] Z. Wang and P. G. Maropoulos, *Real-time laser tracker compensation of a 3-axis positioning system—dynamic accuracy characterization*, The International Journal of Advanced Manufacturing Technology, **84**, pp. 1413–1420 (2015).

[14] B. Hughes and M. Warden, *A Novel Coordinate Measurement System Based on Frequency Scanning Interferometry*, The Journal of the CMSC, **8**, pp. 18–24 (2013).

[15] Sir William Thomson, *History of the Atlantic Cable & Submarine Telegraphy - atlantic-cable.com/CablePioneers/Kelvin.*

[16] V. A. Slaev, A. G. Chunovkina, and L. A. L. A. Mironovskii, *Metrology and theory of measurement*, De Gruyter, Berlin/Boston, 2nd edition (2013).

[17] A. E. Fridman, A. Sabak, and P. Makinen, *The quality of measurements : a metrological reference*, Springer Science & Business Media, LLC (2012).

[18] S. Yang and G. Zhang, *A review of interferometry for geometric measurement*, Measurement Science and Technology, **29**, p. 102001 (2018).

[19] S. S. Tolansky, *An introduction to interferometry*, Longman (1973).

[20] P. Hariharan, *Optical interferometry*, Academic Press (2003).

[21] P. A. Tipler and R. A. Llewellyn, *Modern physics*, W.H. Freeman (2008).

[22] W. M. Saslow and W. M. Saslow, *Chapter 16 – Optics*, pp. 678–IV (2002).

[23] *Interference Newton's Rings www.okotech.com/lp-interference.*

[24] S. Mani Naidu, *Engineering Physics*, pp. 14/10–14/15, Pearson, Delhi, 1st edition (2009).

[25] L. B. Oliveira, J. R. Fernandes, I. M. Filanovsky, C. J. Verhoeven, and M. M. Silva, *Analysis and Design of Quadrature Oscillators*, Springer Netherlands, Dordrecht (2008).

[26] D. C. Williams, *Optical methods in engineering metrology*, Glasgow, 2nd edition.

[27] J. Wang, J. Yu, W. Miao, B. Sun, S. Jia, W. Wang, and Q. Wu, *Long-range, high-precision absolute distance measurement based on two optoelectronic oscillators*, Optics Letters, **39**, p. 4412 (2014).

[28] H. J. Miller, *Location, Absolute and Relative*, in *International Encyclopedia of the Social & Behavioral Sciences*, pp. 284–286 (2015).

[29] *Portable Laser Tracker*, volume Vol.154, Engineering & Manufacturing (2015).

[30] The European Synchrotron, *Laser Tracker and Robotic Total Station Errors*, ESPR (2010).

[31] Bridges B, *How Laser Trackers Work - Accuracy, speed, and minimum advance preparation, make laser trackers among the most versatile of CMMs*, Technical report (2009).

[32] K. C. Lau and R. J. Hocken, *Three and five axis laser tracking systems* (1986).

[33] S. Kyle, *Operational features of the Leica laser tracker*, in *IEE Seminar Business Improvement Through Measurement*, volume 1999, pp. 4–4, IEE (1999).

[34] *Faro Laser Tracker Vantage - iQlaser - www.iqlaser.co.za/faro-laser-tracker-vantage*.

[35] J. Dale, B. Hughes, A. J. Lancaster, A. J. Lewis, A. J. H. Reichold, and M. S. Warden, *Multi-channel absolute distance measurement system with sub ppm-accuracy and 20 m range using frequency scanning interferometry and gas absorption cells*, Optics Express, **22**, p. 24869 (2014).

[36] J. J. Martinez, M. A. Campbell, M. S. Warden, E. B. Hughes, N. J. Copner, and A. J. Lewis, *Dual-sweep frequency scanning interferometry using four wave mixing*, IEEE Photonics Technology Letters, **27**, pp. 733–736 (2015).

[37] J. R. Green, *Development of a Prototype Frequency Scanning Interferometric Absolute Distance Measurement System for the Survey & Alignment of the International Linear Collider*, Ph.D. thesis, Keble College, Oxford (2007).

[38] X. Jia, Z. Liu, L. Tao, and Z. Deng, *Frequency-scanning interferometry using a time-varying Kalman filter for dynamic tracking measurements*, Optics Express, **25**, p. 25782 (2017).

[39] Z. Duan, Y. Wu, M. Li, W. Wang, Y. Liu, and S. Yang, *A novel FMCW waveform for multi-target detection and the corresponding algorithm*, in *IEEE International Symposium on Electromagnetic Compatibility*, volume 2017-Octob, pp. 1–4, Institute of Electrical and Electronics Engineers Inc. (2018).

[40] B. Hughes, M. A. Campbell, A. J. Lewis, G. M. Lazzarini, and N. Kay, *Development of a high-accuracy multi-sensor, multi-target coordinate metrology system using frequency scanning interferometry and multilateration*, in *Videometrics, Range Imaging, and Applications XIV*, volume 10332, p. 1033202, SPIE (2017).

[41] M. Campbell, B. Hughes, A. Lewis, J. Martinez, and N. Copner, *Mulilateration with frequency scanning interferometry and four wave mixing*, Technical report, National Physical Laboratory (2014).

[42] M. S. Warden and M. Stuard Warden, *Absolute distance metrology using frequency swept lasers*, Technical report (2011).

[43] J. Dale, B. Hughes, A. J. Lancaster, A. J. Lewis, A. J. H. Reichold, M. S. Warden, . E. Baumann, F. R. Giorgetta, I. Coddington, L. C. Sinclair, K. Knabe, W. C. Swann, and N. R. Newbury, *Multi-channel absolute distance measurement system with sub ppm-accuracy and 20 m range using frequency scanning interferometry and gas absorption cells*, International Organization for Standardization Geneva E. Hecht, Optics D. Wells and E. Krakiwsky, **22** (2014).

[44] S. L. Gilbert, W. C. Swann, and C.-M. Wang, *Standard Reference Materials : Hydrogen cyanide H13C14N absorption reference for 1530 nm to 1560 nm wavelength calibration - SRM 2519*, Technical report (2004).

[45] S. Gilbert and W. Swann, *Acetylene 12C2H2 Absorption Reference for 1510 nm to 1540 nm Wavelength Calibration -SMR2517a*, National Institute of Standards and Technology (2001).

[46] M. S. Warden, *Precision of frequency scanning interferometry distance measurements in the presence of noise*, Applied Optics, **53**, p. 5800 (2014).

[47] P. A. Coe, D. F. Howell, and R. B. Nickerson, *Frequency scanning interferometry in ATLAS: remote, multiple, simultaneous and precise distance measurements in a hostile environment*, Measurement Science and Technology, **15**, pp. 2175–2187 (2004).

[48] S. Miller and K. Severance, *Photogrammetry system and method for determining relative motion between two bodies* (2011).

[49] U. Wijenayake, S.-I. Choi, and S.-Y. Park, *Automatic detection and decoding of photogrammetric coded targets*, in *2014 International Conference on Electronics, Information and Communications (ICEIC)*, pp. 1–2, IEEE (2014).

[50] F. H. Moffitt and E. M. Mikhail, *Photogrammetry*, Harper & Row (1980).

[51] B. Triggs, P. F. McLauchlan, R. I. Hartley, and A. W. Fitzgibbon, *Bundle Adjustment — A Modern Synthesis*, pp. 298–372, Springer Berlin Heidelberg (2000).

[52] W. Bösemann and Werner, *Industrial Photogrammetry - accepted metrology tool or exotic niche*, ISPRS - International Archives of the Photogrammetry, Remote Sensing and Spatial Information Sciences, **XLI-B5**, pp. 15–24 (2016).

[53] J. Hecht, *City of light : the story of fiber optics*, Oxford University Press (1999).

[54] H. A. C. Wood, K. Harrington, T. A. Birks, J. C. Knight, and J. M. Stone, *High-resolution air-clad imaging fibers*, Optics Letters, **43**, p. 5311 (2018).

[55] P. C. Davies and D. S. Betts, *Quantum Mechanics*, Routledge (2018).

[56] W. J. Wadsworth, A. L. Love, F. Yu, M. R. A. Hassan, M. Xu, and J. C. Knight, *Gas filled hollow core mid-IR fibre lasers*, in *2017 Conference on Lasers and Electro-Optics Europe & European Quantum Electronics Conference (CLEO/Europe-EQEC)*, pp. 1–1, IEEE (2017).

[57] A. N. Kolyadin, A. S. Biryukov, Y. P. Yatsenko, A. D. Pryamikov, E. M. Dianov, I. A. Bufetov, A. V. Gladyshev, and A. F. Kosolapov, *Efficient 1.9-μm Raman generation in a hydrogen-filled hollow-core fibre*, Quantum Electronics, **45**, pp. 807–812 (2015).

[58] W. T. Silfvast, *Laser fundamentals*, Cambridge University Press (2004).

[59] E. A. J. Marcatili and R. A. Schmeltzer, *Hollow Metallic and Dielectric Waveguides for Long Distance Optical Transmission and Lasers*, Bell System Technical Journal, **43**, pp. 1783–1809 (1964).

[60] E. Hecht, *Optics*, GLOBAL EDITION, Adelphi University, 5th edition (2017).

[61] D. Bird, *Attenuation of model hollow-core, anti-resonant fibres*, Optics Express, **25**, p. 23215 (2017).

[62] F. Hadjaj, A. Belghachi, A. Halmaoui, M. Belhadj, and H. Mazouz, *Study of a Fabry-Perot Resonator*, International Journal of Mathematical, Computational, Physical, Electrical and Computer Engineering, **7**, pp. 1189–1193 (2013).

[63] W. Belardi and J. C. Knight, *Effect of core boundary curvature on the confinement losses of hollow antiresonant fibers*, Optics Express, **21**, p. 21912 (2013).

[64] F. Yu, W. J. Wadsworth, and J. C. Knight, *Low loss silica hollow core fibers for 3–4 μm spectral region*, Optics Express, **20**, p. 11153 (2012).

[65] W. Belardi and J. C. Knight, *Hollow antiresonant fibers with low bending loss*, Optics Express, **22**, p. 10091 (2014).

[66] M. H. Frosz, P. S. Russell, M. C. Günendi, G. Ahmed, P. Uebel, N. N. Edavalath, and J.-M. Ménard, *Broadband robustly single-mode hollow-core PCF by resonant filtering of higher-order modes*, Optics Letters, **41**, p. 1961 (2016).

[67] T. A. Birks, W. J. Wadsworth, and P. S. J. Russell, *Supercontinuum generation in tapered fibers*, Optics Letters, **25**, p. 1415 (2000).

[68] T. A. Birks, I. Gris-Sánchez, S. Yerolatsitis, S. G. Leon-Saval, and R. R. Thomson, *The photonic lantern*, Advances in Optics and Photonics, **7**, p. 107 (2015).

[69] T. Birks and Y. Li, *The shape of fiber tapers*, Journal of Lightwave Technology, **10**, pp. 432–438 (1992).

[70] J. Muelaner, W. Wadsworth, M. Azini, G. Mullineux, B. Hughes, and A. Reichold, *Absolute multilateration between spheres*, Measurement Science and Technology, **28**, p. 045005 (2017).

[71] S. Aguado, J. Santolaria, D. Samper, J. Velázquez, C. Javierre, Á. Fernández, S. Aguado, J. Santolaria, D. Samper, J. Velázquez, C. Javierre, and Á. Fernández, *Adequacy of Technical and Commercial Alternatives Applied to Machine Tool Verification Using Laser Tracker*, Applied Sciences, **6**, p. 100 (2016).

[72] S. Kyle, S. Robson, L. Macdonald, and M. Shortis, *Compensating for the effects of refraction in photogrammetric metrology*, Technical report.

[73] A. Glindemann, *Introduction to Spatial Interferometry*, Springer Science & Business Media B.V (2011).

[74] A. DiMarzio, A. Devaney, and S. Lindberg, *Optical quadrature interferometry utilizing polarization to obtain in-phase and quadrature information* (2000).

[75] D. Gavel, *Polarization Quadrature Interferometer*, Laboratory for Adaptive Optics (2004).

[76] V. Greco, G. Molesini, and F. Quercioli, *Accurate polarization interferometer*, Review of Scientific Instruments, **66**, pp. 3729–3734 (1995).

[77] *Gas Cell Wavelength References www.wavelengthreferences.com/products/standard-gas-cells*.

[78] W. Swann and S. Gilbert, *Accuracy limits for simple molecular absorption based wavelength references*, in *Technical Digest: Symposium on Optical Fiber Measurements, 2004.*, pp. 15–18, IEEE (2004).

[79] Wavelength References, *C-Band Wavelength Calibrator Acetylene Gas Cell C2H2*, Technical report, www.wavelengthreferences.com (2000).

[80] Z. Wang, W. Belardi, F. Yu, W. J. Wadsworth, and J. C. Knight, *Efficient diode-pumped mid-infrared emission from acetylene-filled hollow-core fiber*, Optics Express, **22**, p. 21872 (2014).

[81] W. C. Swann and S. L. Gilbert, *Pressure-induced shift and broadening of 1510–1540-nm acetylene wavelength calibration lines*, Journal of the Optical Society of America B, **17**, p. 1263 (2000).

[82] *Thorlabs fiber optomechanics www.thorlabs.com/thorproduct.cfm?partnumber=FT-114X149*, Technical report.

[83] M. Gdeisat and F. Lilley, *One-Dimensional Phase Unwrapping Problem*, Technical report, Liverpool John Moores University (2011).

[84] P. de Groot and S. Kishner, *Synthetic wavelength stabilization for two-color laser-diode interferometry*, Applied Optics, **30**, p. 4026 (1991).

[85] P. de Groot and J. McGarvey, *Chirped synthetic-wavelength interferometry*, Optics Letters, **17**, p. 1626 (1992).

[86] K. Thurner, P. F. Braun, and K. Karrai, *Absolute distance sensing by two laser optical interferometry*, Review of Scientific Instruments, **84**, p. 115002 (2013).

[87] R. Dändliker, R. Thalmann, and D. Prongué, *Two-wavelength laser interferometry using superheterodyne detection*, Optics Letters, **13**, p. 339 (1988).

[88] P. J. de Groot, *Extending the unambiguous range of two-color interferometers*, Applied Optics, **33**, p. 5948 (1994).

[89] G. C. Bjorklund, M. D. Levenson, W. Lenth, and C. Ortiz, *Applied physics Physics B and Laser Frequency Modulation (FM) Spectroscopy Theory of Lineshapes and Signal-to-Noise Analysis*, Technical report (1983).

[90] W. S. Martins, M. Oriá, M. Chevrollier, H. L. D. de S. Cavalcante, and T. Passerat de Silans, *Two-beam nonlinear Kerr effect to stabilize laser frequency with sub-Doppler resolution*, Applied Optics, **51**, p. 5080 (2012).

[91] J. Juarez, *The Use of a Lock-In Amplifier to Stabilize the Frequency of a Laser Diode*, Ph.D. thesis, College of the Holy Cross (2009).

[92] Stanford Research Systems, *MODEL SR850 DSP Lock-In Amplifier*, Technical report (1992).

[93] K. Michels, F. Klawonn, R. Kruse, and A. Nürnberger, *Fundamentals of Control Theory*, in *Fuzzy Control*, pp. 57–234, Springer Berlin Heidelberg, Berlin, Heidelberg (2006).

[94] Smuts Jacques, *Control Notes - Reflections of a Process Control*, Technical report, OptiControls Inc (2011).

[95] F. Haugen, *Ziegler-Nichols' Closed-Loop Method*, TechTeach, pp. 1–7 (2010).

[96] K. Janprom, W. Permpoonsinsup, and S. Wangnipparnto, *Intelligent Tuning of PID Using Metaheuristic Optimization for Temperature and Relative Humidity Control of Comfortable Rooms* (2020).

[97] C. Lorenzini, A. S. Bazanella, L. F. A. Pereira, and G. R. Gonçalves da Silva, *The generalized forced oscillation method for tuning PID controllers*, ISA Transactions, **87**, pp. 68–87 (2019).

[98] L. Wu, Y. Jiang, C. Ma, W. Qi, H. Yu, Z. Bi, and L. Ma, *0.26-Hz-linewidth ultrastable lasers at 1557 nm*, Scientific Reports, **6**, p. 24969 (2016).

[99] T. Uehara, K. Tsuji, K. Hagiwara, and N. Onodera, *Optical beat-note frequency stabilization between two lasers using a radio frequency interferometer in the gigahertz frequency band*, Optical Engineering, **53**, p. 124109 (2014).

[100] *POF Data Book*, MRC Techno Research Inc, Japan (1993).

[101] S. A. Bateman, *Hollow Core Fibre-Based Gas Discharge Laser Systems and Deuterium Loading of Photonic Crystal Fibres*, Ph.D. thesis, University of Bath (2014).

[102] D. Tabor, *Gases, liquids and solids*, Penguin Books Ltd, Victoria, 2nd edition.

[103] C. S. Edwards, G. P. Barwood, H. S. Margolis, P. Gill, and W. R. Rowley, *High-precision frequency measurements of the $\nu 1 + \nu 3$ combination band of 12C2H2 in the 1.5 μm region*, Journal of Molecular Spectroscopy, **234**, pp. 143–148 (2005).

[104] S. Xie, R. Pennetta, and P. S. J. Russell, *Self-alignment of glass fiber nanospike by optomechanical back-action in hollow-core photonic crystal fiber*, Optica, **3**, p. 277 (2016).

[105] R. A. Maruf and M. Bajcsy, *On-chip splicer for coupling light between photonic crystal and solid-core fibers*, Applied Optics, **56**, p. 4680 (2017).

[106] D. Fan, Z. Jin, G. Wang, F. Xu, Y. Lu, D. J. J. Hu, L. Wei, P. Shum, and X. Zhang, *Extremely High-Efficiency Coupling Method for Hollow-Core Photonic Crystal Fiber*, IEEE Photonics Journal, **9** (2017).

[107] M. Artiglia, G. Coppa, P. Di Vita, M. Potenza, and A. Sharma, *Mode field diameter measurements in single-mode optical fibers*, Journal of Lightwave Technology, **7**, pp. 1139–1152 (1989).